University of Strathclyde

Department of Naval Architecture, Ocean and Marine Engineering

Nonlinear hydrodynamic interaction analysis of multi-platform system

XIUDI REN

The thesis submitted in fulfillment of the requirements for the degree of

Doctor of Philosophy

August 2021

Acknowledgement

First and foremost, I would like to thank my supervisor Prof. Longbin Tao for his inspiring advice and kind help. Prof. Tao was always encouraging and helpful with his expertise in hydrodynamic related problems. During my PhD time, his kindly encouragement of my current and future research development inspired me in what I do, especially for building a decent foundation of my academic career. His efforts in supervising me with my PhD study will always be appreciated.

I would like to thank Dr Yibo Liang from Doosan Babcock and Dr Martin Nuernberg from "Technology for Advanced Offshore Services" for their kind help in developing the numerical model and providing test data for validation. Their valuable supports are much appreciated.

I would like to thank Ms Susan Pawson and other staff in the Department of NAOME for their kind help in administrative and technical issues.

I would like to thank all my outstanding colleagues and friends in the University of Strathclyde. They always support and encourage me to solve the problems in academic and life. The time I spend with them makes my life in Scotland more pleasant.

I am grateful to my parents for their selfless support on my study and life. They always support my study and career plan decisions and give me many suggestions based on their experiences. I am proud of being their son.

Finally, I would like to thank my wife, Duojiao Chen, for support me during my whole PhD time even she is doing her own PhD in the US. Without her trust and comprehension, we cannot overcome distance between the UK and the US for these years.

List of Publications

Ren, X., Tao, L., Liang, Y., & Han, D. (2021). Nonlinear wave surface elevation around a multi-column offshore structure. *Ocean Engineering*, *238*, 109757.

Ren, X. and Tao, L., 2021. Nonlinear hydrodynamic characteristics of multi-body platform system. *European Journal of Mechanics, B/Fluids*, *89*, pp.509-524.

Ren, X. and Tao, L., 2020, October. Nonlinear wave surface elevation around array of truncated cylinders. In *30th International Ocean and Polar Engineering Conference, ISOPE 2020* (pp. ISOPE-I).

Ren, X., Liang, Y. and Tao, L., 2019, June. Nonlinear wave surface elevation characteristics analysis around a multi-body offshore platforms system. In *International Conference on Offshore Mechanics and Arctic Engineering* (Vol. 58882, p. V009T13A003). American Society of Mechanical Engineers.

Ren, X. and Tao, L., 2017, July. Probability of Slamming Due to Set-Down of Tension Leg Platform. In *The 27th International Ocean and Polar Engineering Conference*. International Society of Offshore and Polar Engineers.

Abstract

Along with the technological development of ocean engineering, offshore platforms are gradually becoming larger and more complex. The recent development in the deepwater region often involves multiple floating platforms adjacent to each other to perform more complex functions. Several aspects should be concerned due to the larger and more complex offshore structures in the offshore area, like water surface elevation and wave run-up around structures, motion characteristics of platforms in the multi-platform system and wave loads on platforms in multi-platform system. 3D potential flow method is applied in the present study. The perturbation theory is employed to divide the velocity potential into first-order and second-order potential. The boundary value problem at each order is solved by boundary element method.

This research describes the investigation carried out on the surface elevation around single column and multiple columns structures since the peak surface elevation often impacts the offshore structures with nonlinear wave loads and potentially causes slamming to platforms. The near-trapping frequency mode for circular columns is extended and applied for the rounded corner square columns and validated. The characteristics of different mechanism (superposition and near-trapping) for peak surface elevation are identified in the present thesis. The peak value of the second-order surface component caused by superposition decreases with higher corner ratio of column. However, for the peak surface elevation caused by near-trapping, the second-order surface component decreases with lower corner ratio of column. Additionally, the peak surface elevation caused by near-trapping is located at the area enclosed by columns. These characteristics are applied to distinguish the mechanism of peak surface elevation.

This thesis also contains the study on dynamic responses of a two platforms system containing a Tension Leg Platform (TLP) and a tender assisted drilling (TAD) with a flexible connection between the two platforms. The mooring lines and tendons are taken into consideration in the coupled analysis of the multi-body platform's system. The numerical model is validated by the published experimental result. Both frequency domain analysis and time domain coupled analysis are conducted. The motion responses and wave load characteristics on the two

platforms in the multi-platform coupled model are investigated in the numerical simulation. It is found that the nonlinear wave force on TLP (Sum-frequency wave force) and TAD (Drift force) are changed significantly due to the existence of adjacent platform. The impact of hydrodynamic interaction on each platform is primarily determined by the incident wave direction and the arrangement direction of the platforms.

The multi-platform system is not only applied in the oil and gas area but also in the renewable energy area. Research of interaction between an offshore wind turbine and support vessel is contained in the present study. The relative distance and the force along the connecting lines between the wind turbine and support vessel are investigated under different wind-wave misalignment conditions during the operation period. The maximum relative distance and tension in the connecting lines are significantly influenced by the wind-wave misalignment under the low environmental condition (LC) and medium condition (MC). However, there is little impact of misalignment under high condition (HC). For floating wind turbine, the impact of wind-wave misalignment for the floating wind turbine is rather small when the environmental condition is medium and high condition. There is also an interesting discovery that increasing wind speed and wind-wave misalignment evidently leads to a jump of maximum relative distance and maximum tension in the connecting lines.

List of Figures

List of Tables

List of symbols

$\Phi(x, y, z, t)$	Total velocity potential
$\Phi^{(1)}(x, y, z, t)$	Total first-order velocity potential
$\Phi^{(2)}(x, y, z, t)$	Total second-order velocity potential
ω	Circular frequency of incident wave
$\phi^{(1)}(x, y, z)$	Complex first-order time-independent total velocity potential
$\phi_I^{(1)}$	Complex first-order time-independent incident wave potential
$\phi_D^{(1)}$	Complex first-order time-independent diffraction wave potential
$\phi_R^{(1)}$	Complex first-order time-independent radiation wave potential
N_i	i-th body in the multi-body system
$\xi_m^{(1)N_i}$	First-order complex amplitude of the oscillatory motion of body N_i in m-th mode
$\phi_m^{(1)N_i}$	First-order unit-amplitude radiation potential for body N_i in m-th mode
m, k	Modes referred to as surge, sway, heave, roll, pitch and yaw
$n_m^{N_i}$	Generalized normal vectors
ϕ_{ij}^{+}	Sum-frequency time-independent velocity potential
ϕ_{ij}^{-}	Difference-frequency time-independent velocity potential

$\phi_I^{\pm}$ Second-order time-independent incident wave potential

$\phi_D^{\pm}$ Second-order time-independent diffraction wave potential

$\phi_R^{\pm}$ Second-order time-independent radiation wave potential

$\xi_m^{(2)N_i}$ Second-order complex amplitude of the oscillatory motion of body N_i in m-th mode

$\phi_m^{(2)N_i}$ Second-order unit-amplitude radiation potential of body N_i in m-th mode

$Q_F^{\pm}$ Inhomogeneous terms in equation of second-order free surface condition

$Q_B^{\pm}$ Inhomogeneous terms in equation of second-order boundary condition

$G(\boldsymbol{\zeta};\mathbf{x})$ Green function which is referred to as wave source potential

σ Source strength

Num Total number of panels

$\mathbf{x}_p$ The coordinate of the centre of the p-th panel

μ Added mass

λ Damping coefficient

$F^{(1)}$ Total first-order force

$F_I^{(1)}$ First-order incident wave force (Froude–Krylov force)

$F_D^{(1)}$ First-order diffraction wave force

$F_R^{(1)}$	First-order radiation wave force
$F_{ex}^{(1)}$	First-order exciting force
$F_{HS}^{(1)}$	First-order hydrostatic force
$\varsigma^{(1)}(t)$	First-order time-dependent surface elevation
$\eta^{(1)}$	First-order time-independent surface elevation
$F^{(2)}$	Total second-order force
$F_I^{(2)}$	Second-order incident wave force
$F_D^{(2)}$	Second-order diffraction wave force
$F_R^{(2)}$	Second-order radiation wave force
$F_{ex}^{(2)}$	Second-order exciting force
$F_{HS}^{(2)}$	Second-order hydrostatic force
$F_q^{(2)}$	Second-order force caused by quadratic first-order quantities
$f_{ji}^{\pm}$	Quadratic transfer function (QTF) of second-order exciting force
$\varsigma^{(2)}(t)$	Second-order time-dependent surface elevation
$\eta_{ji}^{\pm}$	Quadratic transfer function (QTF) of second-order surface elevation
$\eta^{(2)}$	Second-order time-independent surface elevation (double frequency)

$\bar{\eta}$	Constant term time-independent surface elevation
η	Maximum total surface elevation amplitude
F_{wind}	Wind force on the structure
M_{wind}	Wind moment on the structure
$F_{current}$	Current force on the structure
$M_{current}$	Current moment on the structure
C_w	Wind coefficient
ρ_α	Air density
U	Relative wind speed on the platform
A_w	Shadow area
C_c	Current coefficient
ρ_w	Fluid density
A_c	Shadow area in current direction
V	Current speed
L	Distance from force to centre of gravity
I	Rotation moment of inertia
A_p	Water plane area
M_p	Waterplane moment of about y-axis

$\kappa(t)$	Retardation function
R^I	Inertia force vector of slender system
R^D	Damping force vector of slender system
R^s	Internal structural reaction force vector of slender system
R^E	External force vector of slender system
$r, \dot{r}, \ddot{r}$	Structural displacement, velocity and acceleration vectors
M^S	Structural mass matrix of slender system
$M^F(r)$	Mass matrix accounting for internal fluid flow
$M^H(r)$	Displacement-dependent hydrodynamic mass matrix
$C^s(r)$	Internal structural damping
$C^H(r)$	Hydrodynamic damping matrix
Δt	Time interval
M_t	Tangential mass matrix
C_t	Damping matrix
K_t	Stiffness matrix
$\widehat{K}_t$	Effective stiffness
$\Delta\widehat{R}_t$	Effective incremental load vector
γ, β, θ	Time integration parameters based on the Newmark β-family method

Contents

1 Introduction

1.1 Backgrounds and motivation

In the modern world, oil and gas is the main source of energy for most societies. According to the Statistical Review of World Energy by BP (2020), the oil and gas takes 57.3% of primary energy consumption in the world in 2019 (Figure 1.1).

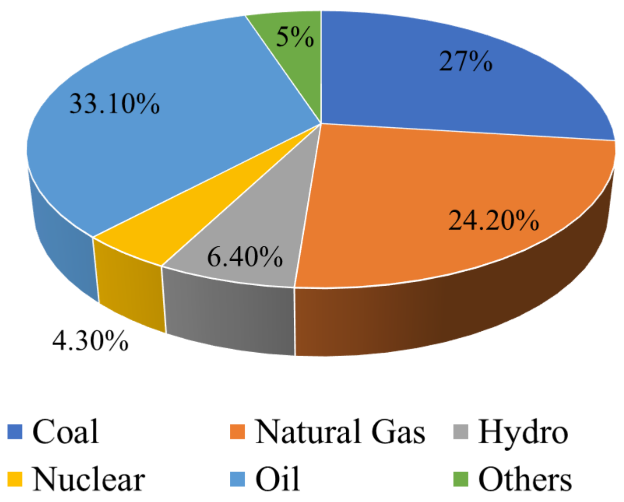

Figure 1.1 World total primary energy consumption by fuel in 2019 (BP, 2020)

Oil and gas had already been used in some capacity, such as fossil fuel or as a material for construction, for thousands of years before the modern era, with the earliest known oil wells being drilled in China in 347 AD. The modern history of the oil and gas industry started in 1847, with a discovery made by Scottish chemist James Young. He observed natural petroleum seepage in the Riddings coal mine, and from this seepage distilled both a light thin oil suitable for lamps and a thicker oil suitable for lubrication (Umar, 2019).The first offshore oil well was drilling in 1897 by Henry L. Williams at the Californian coast region. He used the pier to support a land rig next to an existing field (Maribus, 2014, National Academies of Sciences, 2016). By 1921, steel piers were being used in Rincon and Elwood (California) to support land-type drilling rigs. The first "on-water drilling" was born in the swamps of Louisiana in the early 1930s with the use of shallow-draft barges. The first free-standing structure had been installed in the Gulf of Mexico 1.5 miles offshore with the aim to drill for oil through the seabed (Pratt et al., 1997). Offshore accounts for 15% of global oil reserves and 45% of global gas reserves, as well as almost 30% world's remaining conventional resources in the case of oil, and a share of almost two-thirds in the case of gas (Birol, 2018).

For a long term, the offshore production is limited in the shallow water along coastal regions. However, with the development of offshore technology and the discovery of many oil and gas deposits, the offshore industry start moving to deepwater. Especially in recent decades, offshore oil and gas exploration and exploitation in deepwater increasing very fast. The definition of water depth is listed below:

Shallow water: The drilling and operation water depth is less than 400m.

Deepwater: The drilling and operation water depth of platform is around 1500m.

Ultra-deepwater: The drilling operation water depth is greater than 1500m.

As shown in Figure 1.2, deepwater commitments are expected to see a large growth as their cost has now become much more competitive against greenfield continental shelf reserves (Karagiannopoulos, 2021). The shallow water project still takes the largest part of the total offshore projects. However, the number of deepwater projects shows an impressive growth. With the oil price crashed in 2014 and 2015, the day rates of drilling platform and offshore support vessel is also fallen making the search for new field in deepwater more economically.

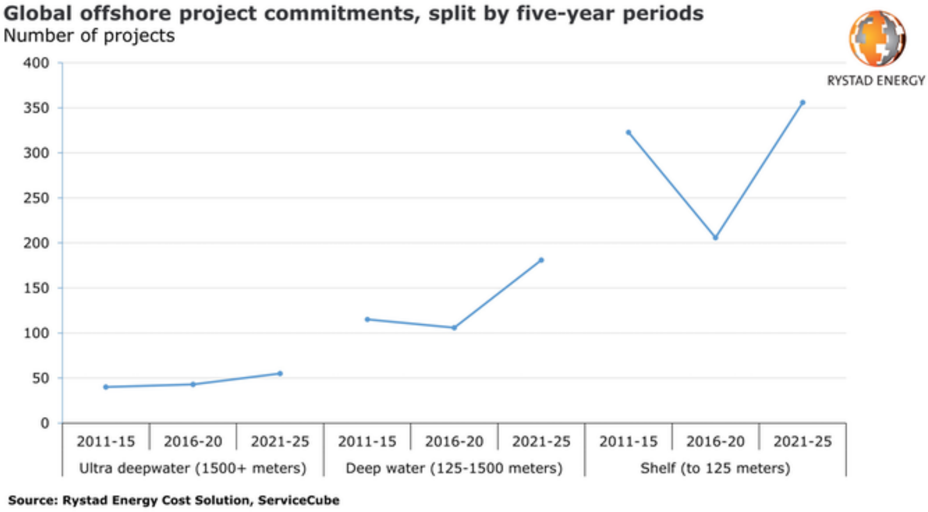

Figure 1.2 Global offshore projects commitments (Karagiannopoulos, 2021)

Due to the oil and gas wells moving into deepwater, the fixed platforms are no longer suitable for deepwater exploitation and exploration. To adapt different kinds of offshore drilling and production requirements with different working depth, different types of floating platforms are developed and appeared in recent decades such as Floating Production Storage and Offloading vessel (FPSO), Spar, Semi-submersible and Tension Leg Platform (TLP). Thus, a considerable number of large size floating structures have been fabricated and installed in different deepwater regions around the world (Figure 1.3 and Figure 1.4).

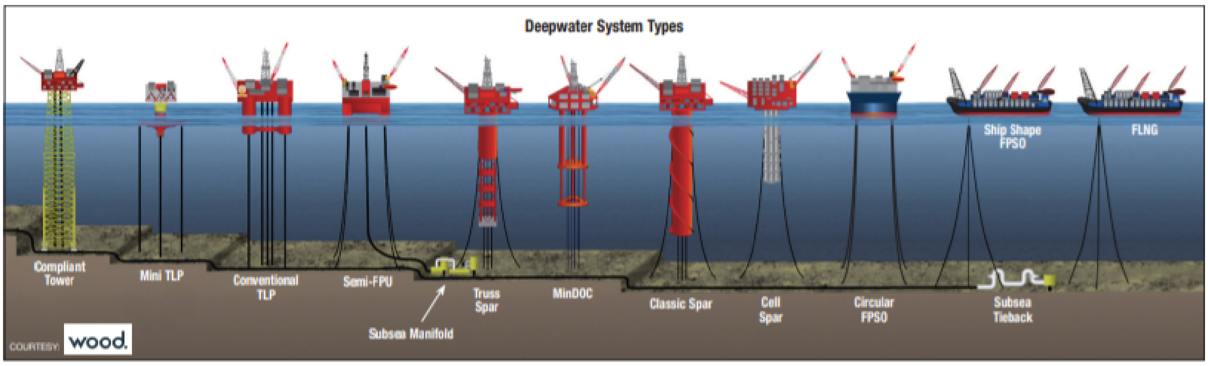

Figure 1.3 Deepwater system types (Offshore, 2019)

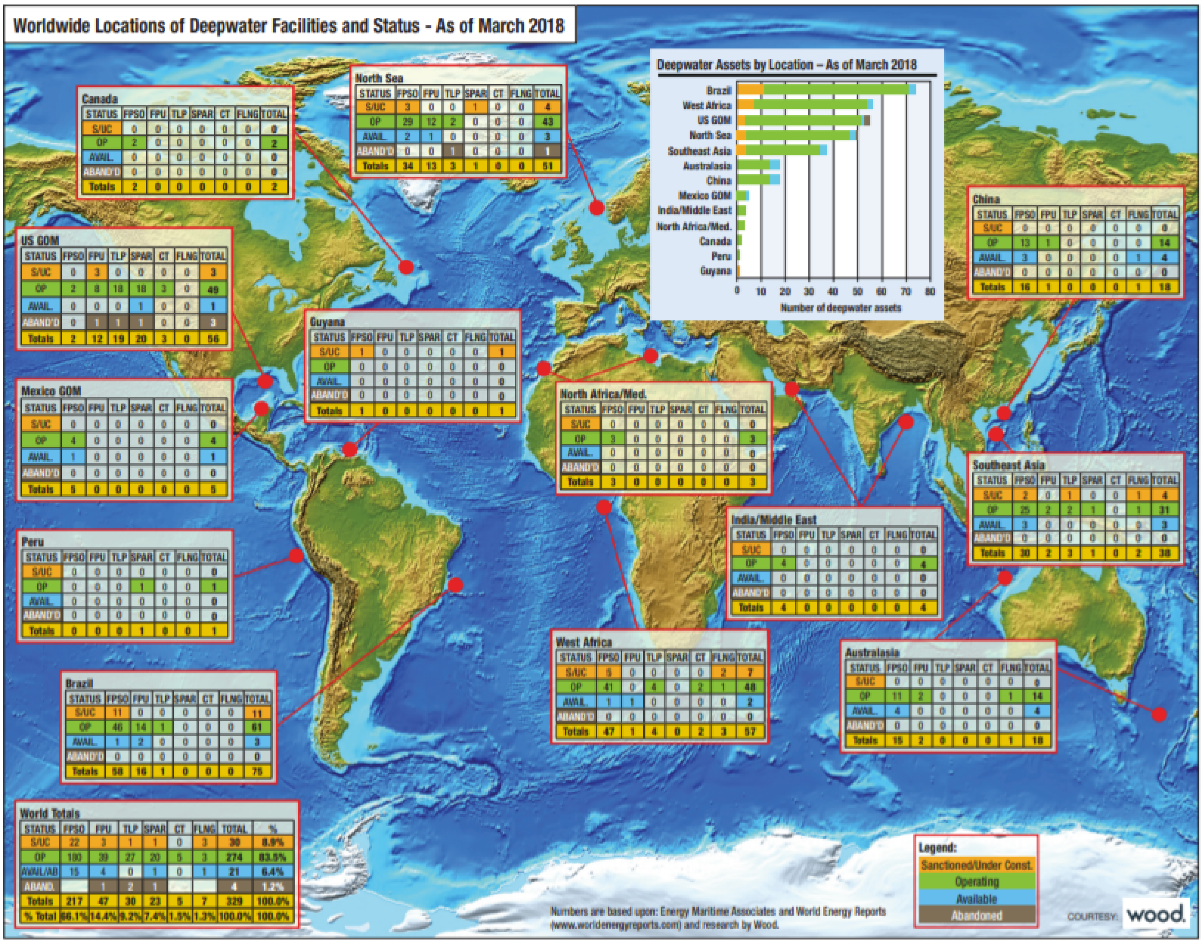

Figure 1.4 Deepwater platforms distribution all over the world (Offshore, 2018)

Since the offshore oil and gas fields progressively moving towards deepwater, more complex functional requirements are desired for the oil and gas drilling and production platform system. The traditional individual offshore platform is replaced by the complex drilling and production system gradually. The platforms for producing and drilling or accommodating are always combined as a multi-platform system to achieve more functions and support. The Odin field is the first field development applying the concept of the combination of the different platforms (Figure 1.5).and the project is consisting of a fixed jacked platform and a tender vessel (Smith and Dixon, 1987). With the first successful attempt, more tender support vessels are used with the nearshore fixed platforms.

Figure 1.5 Configuration of Odin field (Smith and Dixon, 1987)

To explore the resource in deepwater, the floating platforms are needed. Tension leg platform (TLP) is a widely employed option for the oil and gas production in deepwater for its good stability at sea. Besides, tender assist drilling (TAD) system has a great economic benefit since it can provide several kinds of supports to the main production platform. The combination of coupled TLP-TAD system is often adopted during the drilling stage since the advantages of TLP's motion characteristics and TAD's outstanding supportive abilities (Adrian and Wong, 2018).

The first commercialized floating multi-platform system which is serving in deepwater was completed in 2018 named Malikai containing TLP and TAD in the multi-platform system (Figure 1.6). Malikai is a marginal field ---with limited reserves in challenging reservoirs, remote from existing infrastructure and in 500m water depth (Adrian and Wong, 2018). The TLP and TAD in multi-platform system are connected by nylon hawser ropes together with chain-polyester-wire moorings on the TAD and TLP allow for station-keeping during operation conditions.

Figure 1.6 Configuration of Malikai Project (Aramanadka et al., 2018)

In multi-platform system adopted in Malikai project, the TLP is employed as the production and storage platform and TAD is applied as drilling vessel and accommodation platform. In this thesis, the simulated model is also based on the Malikai project.

1.2 Literature review

Due to the larger and more complex offshore structures required for application in the harsh offshore environment, there are several aspects such as nonlinear water surface elevation and wave run-up around structures, motion characteristics of platforms in multi-platform system as part of the consequence of hydrodynamic interaction between platforms in multi-platform system should be examined in detail.

1.2.1 Nonlinear surface elevation around multiple column structures

With the continuing development of the offshore oil and gas resources, the hydrodynamic interactions among a group of cylindrical structures attracted much attention in recent decades. There is a strong association between surface elevations and wave loads on offshore structures, especially when it comes to the nonlinear slamming loads on the deck caused by excessive vertical surface elevation. An interesting issue in designing offshore platforms is how to determine the distance between deck and water surface which is also called air gap design in order to avoid slamming which may cause serious damage to structures. The peak of surface elevation generated near column and climbing along structure is widely known as wave run-up (Kriebel, 1992). When the extreme peak surface occurs in the area enclosed by multiple columns due to large resonant motion at certain frequencies, the phenomenon is called near-trapping (Evans and Porter, 1997). In addition, free surface elevation is also associated with phenomena such as wave impacts, green water, wave deformation, rolling, spray (Shan et al., 2011). Therefore, accurate prediction of surface elevation is an essential part of the design stage of an offshore platform.

In a traditional design concept, it is used to neglect any deck slamming probability by increasing the initial air gap of platforms. The traditional air gap design method is simply to sum up the vertical response of the platform and wave elevation directly. This method has a great impact on the stability of the platform and increases project expenditure sharply. There is also a simplified method based on linear and nonlinear method to calculate the air gap in a quick way (DNVGL-OTG13). In OTG13, the linear surface elevation is multiplied by an asymmetry factor to estimate the air gap. The asymmetry factor is calculated accounting all relevant effects including platform motion, nonlinear effect and current effect. There are some relevant effects to design the safe air gap. An empirical method for estimating the non-linear enhanced upwelling near columns is proposed by Stansberg (2014). Pakozdi et.al. (2018) have generalized the method for time domain analysis. A comparison of numerical and experimental results for surface elevation above pontoons of a semi-submersible was presented by Pessoa et.al. (2018). Non-linear motion effects of platform on the air-gap were investigated by Kvaleid, et al. (2014). To avoid the over design of the air gap, research have been carried out to predict wave surface elevation which is strongly associated with air gap design (Taylor and Sincock, 1989, Sweetman et al., 2001, Dong and Zhan, 2009, Low, 2010, Grice et al., 2013, Abdussamie et al., 2017, Fang et al., 2018).

Considerable research efforts have been made on the wave run-up along columns in offshore structure. Either numerical simulation or model test are performed by Raman and Venkatanarasaiah (1976), Raman et al. (1977), Chakrabarti (1978) and Kim and Yue (1989) to predict the wave run-up amplitude. However, the comparisons between numerical results and laboratory data have not generally been encouraging. Kriebel (1992) described second-order wave run-up and predicted nonlinear wave run-up distributions for 22 experimental conditions. It is found that the nonlinear diffraction theory is valid for the same relative depth and wave steepness conditions applicable to Stokes second-order plane-wave theory. Morris-Thomas and Thiagarajan (2004) investigated the wave run-up on the single fixed bottom-seated cylinder in gravity waves. It was shown that the second-order harmonic component in the incident wave is important to the run-up amplitude for a single column. Xiong et al. (2015) measured the inline force for a single truncated circular cylinder in a wave tank under different submergence depths and revealed that the inline force on the single truncated cylinder is influenced by the submergence depth, wave steepness and scattering parameters. The current also have significant impact on the surface elevation when it has same direction with incident wave. The wave-current effect can significantly increase the drift force and run-up amplitude (Pan et al, 2016; Liu et al, 2016).

Besides the wave run-up, the near-trapping amplitude also has great influence on the air gap design which is directly impacted by wave run-up. The near-trapping phenomenon between columns related to geometry spaces and incident wave frequency is discussed by Linton and Evans (1990). Linear diffraction theory is applied by Evans and Porter (1997), the near-trapping amplitude is found to increase with decreasing of the space of columns. Linton and Evans (1990) and Malenica et al. (1999) revealed the relationship between incident wavelength and geometry space causing near-trapping among circular columns. Grice et al. (2013) applied the linear theory to the diffraction of regular waves by arrays of columns. Free surface amplification has been calculated using the linear model of the computer program DIFFRACT and compared between solitary columns and arrays of two and four columns. It is reported by the authors that the near-trapping phenomenon between the cylinders has been captured by the simulations based on the first-order solution. Cong et al. (2015) carried out the experiment on the diffraction of regular waves by four-cylinder structures and reported that near-trapping wave motion was observed inside the structure for a specific incident wave frequency.

There are many factors influencing the wave surface elevation around offshore structures like fixity and existence of pontons. By comparing the experimental results of platforms with and without pontoons linked to the columns, the surface elevation is found to be slightly smaller in the absence of the pontoons (Niedzwecki and Huston, 1992). Simos et al. (2008) performed small-scale model tests of air-gap response of a floating semi-submersible. It is revealed that the first-order numerical solution seriously underestimates the wave run-up. Shan et al. (2011) investigated the surface elevation around different columns of a semi-submersible. The model tests were conducted for both floating and fixed models and it was found that the wave run-up for the floating semi-submersible is significantly smaller than that for the structure being fixed. In addition, the results indicated that the wave shape close to the columns shows higher harmonic characteristics due to the interaction between waves and columns of the semi-submersible platform.

It is widely acknowledged that viscosity can play important role in wave breaking and wave run-up. Considerable effort has been made to theoretically predict the surface elevation or wave run-up using the computational fluid dynamics (CFD) method. Wang and You (2009) used viscous solver FLUENT based on the Navier-Stokes (N-S) equations to simulate the interaction of viscous wave fields with a fixed semi-submersible platform. It is revealed that the viscous effect reduces the wave run-up on the columns of the platform. Dong and Zhan (2009) obtained wave elevation and run-up along a fixed circular column in shallow water based on the N-S equations applying the volume of fluid (VOF) method for the free surface. Good agreement was observed between numerical simulations and experimental measurements. Chen et al. (2014) generated regular waves and focused waves by using OpenFOAM and carried on investigating wave runup and wave load on a single column wind turbine under the regular wave and focused wave. Their results captured the higher order harmonic components of wave runup and wave load showed agreement with experimental measurement. Lin et al. (2017) developed a CFD model for simulating different types of wind turbines at sea. The results showed that the wave run-up and wave load of these models under small wave steepness is even higher than that for larger wave steepness at some incident wave frequency, and the authors attributed that to near-trapping phenomenon.

It should be noted that the CFD method can be accurate in capturing the interaction between water and air in wave breaking or wave run-up. However, for large structures with the ratio of the two parameters produce the free-surface Keulegan-Carpenter number, $Kc=A/a<\boldsymbol{O}(\mathbf{1})$ (A and a being the wave amplitude and cylinder radius, respectively), the potential theory is applicable. For A/a less than of order unity, the flow around the cylinder will not separate and the fluid domain can be described by potential theory (Morris-Thomas and Thiagarajan, 2004).

Potential flow theory based numerical model provides a more effective way to solve the wave-structure interactions often involving the prediction of nonlinear surface elevation and wave loads on offshore structures. Wang and Wu (2010) investigated an array of cylinders in a numerical wave tank. Free surface elevation and hydrodynamic force were obtained for both bottom mounted and truncated cylinders. Sweetman et al. (2001) used the commercial program WAMIT in which the second-order nonlinearities were included to predict the air-gap response of a semi-submersible. Kristiansen et al. (2004) conducted the mesh sensitivity study of columns and free surface for the second-order nonlinear wave run-up.

1.2.2 Hydrodynamic interaction between multi-platform system

Comparing with the single floating structure, the hydrodynamic interaction between floating structure and wave also has great impact on the motion and load characteristics of platforms in the multi-platform system. The hydrodynamic interaction between platforms and waves becomes more complex in multi-platform system than single platform. As one of the critical aspects, the response of the mooring lines system and the bridge between two platforms are determined by the motion characteristics of each platform in the multi-platform system. The accurate prediction of the multi-platform hydrodynamic response is very important for the coupled analysis between the platforms and mooring lines system. The interaction between multi-platform system and the wave which contains diffraction and radiation makes the solution of the wave load and prediction of the motion response more challenging. Additionally, the nonlinear mooring system and the bridge between two platforms make the coupled analysis of multi-platform more complex to solve.

Among some of the pioneers, Kim (1972) applied the 2D strip method in the 1970s solving the interaction between slender structures in waves. Loken (1981) calculated the motion response and the wave drift force for a multi-body system based on the potential theory. Comparing with the model test values, the result of drift force is lower since the neglection of the viscosity. Williams and Rangappa (1994) applied a semi-analytical method to calculate the added mass and potential damping of ocean structures consisting of arrays of circular cylinders. Chakrabarti (1999) and Williams and Li (2000) used the multiple-scattering method, which is efficient for arrays of axisymmetric bodies, to analyse the interaction between different bodies. Williams and Li (2000) employed the finite-element method to investigate the dynamics of multiple floating structures. Choi and Hong (2002) applied a higher-order boundary-element method (HOBEM) to analyse hydrodynamic interactions of a multi-body system. The nonlinear wave run up and air-gap response in multiple columns Semi-submersible were conducted by Lu et al. (2020).

The multi-body system is also widely applied in the drilling and production of oil and gas and storage and loading platforms like FPSO and FLNG with side-by-side arrangement (Jean-Robert et al., 2006, Watai et al., 2015). Hydrodynamic characteristics of two ships coupled motion response, wave load and some issues like water surface resonance in the narrow gap between ships are investigated (Zhao et al., 2014, Perić and Swan, 2015, Jin et al., 2019). More recently, Ganesan and Sen (2016) conducted numerical simulation of an FPSO with a shuttle side-by-side in 3D numerical wave tank. Gap resonance is studied by implementing a damping lid method with a constant damping factor to solve the over estimation of free surface. Zhao et al. (2020) investigated the gap resonance between two barges investigating the group dynamics and wave propagation of the resonant responses in a narrow gap by model test. It showed that the gap resonance is sensitive to the approaching wave heading direction and the group velocity of the resonant mode is smaller than that for deep water free waves. Huang et al. (2018) carried out both experiment and numerical study to investigate the response of the gangway between two side-by-side FPSOs. Li (2020) investigated the multi-body hydrodynamic resonance and shielding effect of vessels parallel and nonparallel side-by-side arrangement.

It is noted that some researchers also applied the viscous fluid based on CFD to solve such kind of hydrodynamic issues. Ok et al. (2017) solve the motion of side-by-side floating vessels by using the finite-volume method to solve the N-S equation with OpenFOAM. Gupta et al. (2018) carried out the numerical study of VIM and vibration on riser in TLP-TAD system. Liang (2018) calculated the two semi-submersible platform system under the current condition. The "lock-in" phenomenon between two Semi-submersibles under 0° incident wave had been simulated to validate weather the collide would occur. Although CFD method can correctly solve multi-body hydrodynamic problems, it is very time-consuming compared to potential theory which is widely used at present.

To date, most research on the topic has focused on the hydrodynamic characteristics between ships or jacked platforms (Wu, 2014, Xu et al., 2015). There are also some studies on the hydrodynamic interaction between two floating platforms in a multi-platform system. Xia and Taghipour (2012) conducted an eigenvalue study of mooring system of Tension Leg Platform (TLP) with a tender assisted drilling (TAD) in longitudinal motion of the two bodies in the multi-body system. Choi et al. (2018) conducted an experimental study on TLP and Semi-sub's motion response characteristics. It is observed that the coupled low-frequency motion periods of the TLP-tender semi-submersible platform are generally shorter than those of individual structure due to additional hawser and moorings between the two floating bodies. Dong et al. (2019) investigated the motion of gangway between two platforms in the multi-body platform system using both model test and numerical simulation. The results of gangway extension and rotation show that the dominant degree-of-freedom (DOF) of global motion for gangway responses is identical under different headings. The extreme value predictions of gangway responses are also performed based on Weibull distribution in their research. Morandini et al. (2005) computed some basic gangway responses under a tandem configuration without a very strong hydrodynamic interaction. Both Li et al. (2015) and Huang et al. (2018) performed studies on gangway responses between floater and FPSO floating side-by-side in parallel and non-parallel configurations, respectively.

Multi-platform system is not only applied in the oil and gas field but also in offshore wind energy development. By increasing number of structures being installed in the sea, there is a significant demand for offshore support vessels to carry out the necessary and regular maintenance and inspection tasks required for the safe operation of offshore wind farms. Vessel based inspection systems are used by most operators for regular inspections and maintenance regarding scour, corrosion, weld, and structural inspections. The motion characteristics of gangway and fender for docking a floating wind turbine had been simulated using numerical method (Wu, 2014). Guanche et al. (2016) applied this method on different arrangements of gangways for floating wind turbines under different wave conditions.

1.2.3 Coupled analysis in multi-platform system

The complexity of the multi-platform issue lies in not only the hydrodynamic interaction between platforms but also the coupled analysis of connected platforms and their mooring systems.

In early stage of investigation of multi-platform system or so-called multi-body system, the interconnected lines are not contained, and the motion equation of each body is calculated individually. There are several studies mainly focus on the hydrodynamic interaction between two adjacent bodies without any connections. However, the offshore structures become larger and more complex with the development of the offshore technology and more functions are desired. The offshore structures are often connected by hinges or moorings in some projects. The dynamic motion of connected structures and coupling effect due to the connections are attracted more attention among the researchers. Newman (1994) introduced a method of computing the motions of simply connected (rigid or hinged) floating bodies as well as the motions of the connection, within the framework of linear frequency-domain model. Newman (2001) and Taghipour and Moan (2008) considered the dynamic coupling effect between the bodies in multi-body system simulation. Koo and Kim (2005) simulated two moored vessels in side-by-side offloading operation in irregular waves by using a combined matrix method. They considered both vessel and mooring dynamics, as well as the coupled hydrodynamic coefficients. The sway and roll motions were found significantly influenced by the mechanical coupling effects between two vessels.

1.2.4 Knowledge gaps in multi-platform system

As described in the above introduction and review of some earlier research, many issues of the hydrodynamic characteristics of multi-platform system have to be clarified for consideration in practical design. The hydrodynamic interaction between two platforms in multi-platform system should also be investigated since the diffraction and radiation caused by adjacent platform can change the fluid characteristics around the platform significantly. There are various physical phenomena such as shielding effect caused by the existence of adjacent platform should be investigated to determine its impact on the multi-platform system. A further understand of motion response and wave load on platforms in multi-structure system is needed, especially with the mooring lines and connection between platforms in the whole system. In addition, the surface elevation around multi-structures columns and different platforms should be properly investigated since the surface elevation around structure and wave run-up along columns are associated with the air gap design of the platforms. Some fluid physical reason for the higher surface elevation in multi-structures columns should be clarified. With the research stated in the previous sections, the knowledge gap can be itemized as following:

- The fluid mechanism (hydrodynamic interaction) in multi-platform system should be clarified under different wave direction since the system is not double symmetrical.
- The impact of the adjacent platform on characteristics of motion and wave force on platform should be clarified.
- The method to distinguish the physical reason of the peak surface elevation can be further clear.

The potential flow theory is applied in the present thesis. In potential flow theory, the fluid is assumed as inviscid. It is sufficient to apply the first-order and the second-order potential flow theory to predict the free surface elevation when the Keulegan-Carpenter number is small which means the viscosity is not dominated.

The potential flow theory also has its limitations. If there is strong nonlinearity of the incident wave which may lead an extreme strong nonlinear phenomenon such as jet-like run up, the viscous effect might become more important, and the compressibility of air trapped between water and the structure boundary should be taken into account. A CFD tool or method which contains the viscous effect should be employed to predict the run up. For the motion response of the structures in the multi-platform system, there will be larger prediction of motion at the natural period of the structure. However, the potential damping is more dominated at the normal range of incident wave period. The potential flow theory can be employed in most conditions.

1.3 Research aims and objectives

As indicated in the introduction and review of multi-platform system, many important scientific issues of hydrodynamic interaction for multi-platform system should be investigated. A better understand is needed on the hydrodynamic interaction and shielding effect among the multi-platform system, motion response feature of platforms in the system, nonlinear wave force on the platforms' arrangement in system, nonlinear surface elevation around multi-column structure and multi-platform system. This project is to carry out numerical study on hydrodynamic characteristics of multi-platform system in deepwater operation, and the detailed fluid physics behind the complex hydrodynamic phenomena. The following objectives are set to achieve the project aims:

- To develop a reliable numerical model to predict the hydrodynamic characteristics of typical multi-platform system for application in offshore oil and gas production. This part of study will be carried out on the realistic offshore multi-platform system including TLP and TAD for deepwater oil and gas production.

- To investigate the fluid mechanics that are related to the multi-platform system, e.g., shielding effect caused by the adjacent platform and the hydrodynamic interaction between platforms. The investigation on the hydrodynamic interaction under heading wave and beam sea are included in this part.

- To predict the motion response and nonlinear wave force on the platforms in the multi-platform system, such as relative distance between platforms in multi-platform system and drift force on platform in multi-platform.

- To examine the characteristics of nonlinear surface elevation and the physical mechanisms around the multi-column structure and multi-platform system. Different components of the surface elevation are investigated to distinguish different physical mechanisms causing peak surface elevation.

- To demonstrate the application of a single point mooring with the multi-platform/vessel system in offshore wind farm maintenance using the present coupled model, further investigate the characteristics of motion response of the offshore support vessel and dynamic tension in the connecting lines.

1.4 Thesis outline

The thesis is divided into six chapters. A brief introduction of the multi-platform and a comprehensive literature review of the related research are presented in Chapter 1. Methodology, including potential theory, frequency- and time-domain analysis method are described in Chapter 2. Chapter 3 contains development of the numerical model and implementation including model validation, matrix of the numerical simulation and detailed results and discussions about the surface elevation around multiple columns structures (Ren and Tao, 2020, Ren et al., 2021a). Both experimental test and numerical simulation of the TLP-TAD multi-platform system are presented in Chapter 4 (Ren and Tao, 2017, Ren et al., 2019, Ren and Tao, 2021). Interaction of the offshore wind turbine and offshore support vessel in multi-platform system are displayed in Chapter 5. The conclusions of the present study and discussion about the future studies are given in Chapter 6.

2 Numerical methodology

2.1 Coordinate system

In the multi-platform system, there are three coordinates are introduced to describe the motion response. One is the global coordinate system, O-XYZ, with the origin located at the mean water level (MWL), and two local systems which is fixed on the platform, O_1-$X_1Y_1Z_1$ and O_2-$X_2Y_2Z_2$, relative to the mean position with the origins located at the centre of gravity (COG) of each body. In addition, the third kind of inertial reference frames for two platforms which are located at the same original position with local coordinates should be introduced. They are fixed in space and coincides with local system at rest. It is applied to measure the oscillating motions of platforms. The position of the two coordinates fixed on platforms in O-XYZ are listed in Table 2.1. In the present thesis, the motions and force are calculated according to the body fixed coordinate system on each platform.

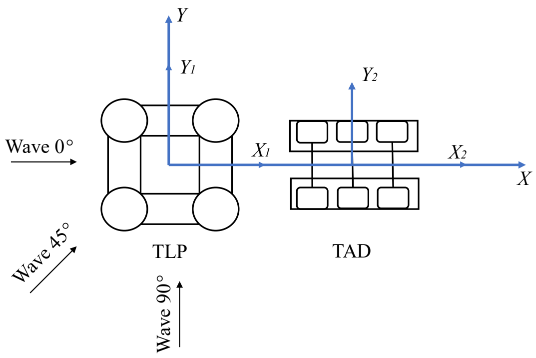

(a) Top view

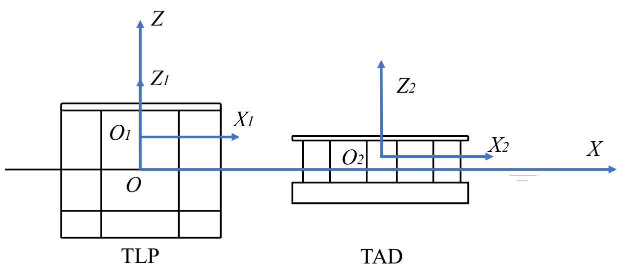

(b) Side view

Figure 2.1 Coordinates system for multi-platform system

Table 2.1 The initial positions of two local coordinate systems O_1-$X_1Y_1Z_1$ and O_2-$X_2Y_2Z_2$ in global coordinate system

	X/m	Y/m	Z/m
O_1-$X_1Y_1Z_1$	0	0	9.76
O_2-$X_2Y_2Z_2$	109.04	0	6.85

2.2 Some assumption and perturbation

In the present study, the fluid is assumed inviscid, irrotational and incompressible. The total velocity potential $\Phi(x, y, z, t)$ satisfies the Laplace equation and different boundary conditions. The BVPs will be solved in the following part in both first-order and second-order to investigate the hydrodynamic characteristics of multi-platform system.

With the assumption of a perturbation solution in terms of a small wave slope of the incident waves, the velocity potential is expanded in a form (Wamit Theory Manual,1993):

$$\Phi(x, y, z, t) = \Phi^{(1)}(x, y, z, t) + \Phi^{(2)}(x, y, z, t) + \cdots \tag{2.1}$$

According to the perturbation of the total velocity potential, the first-order and second-order boundary value problem are considered separately. The incident wave potential is perturbated to second-order, the nonlinearities of the second-order potential and quadratic first-order quantities are taken into account in the calculation. Additionally, the nonlinear incremental equation of motion is applied in the time domain coupled analysis making the stiffness on each platform update at each time step.

2.3 The first-order problem in multi-platform

The total first-order velocity potential $\Phi^{(1)}(x, y, z, t)$ for the wave-body interaction can be expressed by a sum of components having circular frequency ω:

$$\Phi^{(1)}(x,y,z,t) = Re\{\phi^{(1)}(x,y,z)e^{-i\omega t}\}$$
$$= Re\left\{\left[\phi_I^{(1)} + \phi_D^{(1)} - i\omega \sum_{m=1}^{6} \sum\nolimits_{1}^{N} (\xi_m^{(1)N} \phi_m^{(1)N})\right] e^{-i\omega t}\right\} \tag{2.2}$$

Here the $\phi^{(1)}(x,y,z)$ is the complex first-order velocity potential which is independent of time. The subscript m=1,2,…6 represents the six degree of freedom of motion (surge, sway, heave, roll, pitch and yaw respectively). The $N=1,2,\cdots N_i \cdots N_j \cdots N$ is the number of the platforms in multi-body system. The $\phi^{(1)}(x,y,z)$ can be decomposed to the sum of incident wave potential $\phi_I^{(1)}$, diffraction potential $\phi_D^{(1)}$, and radiation potential $\phi_R^{(1)}$.

The first-order incident wave spatial potential $\phi_I^{(1)}$ can be expressed as:

$$\phi_I^{(1)} = \frac{-igA}{\omega} \frac{\cosh\ k(z+h)}{\cosh\ kh} e^{ikx} \tag{2.3}$$

The radiation potential is a linear combination of the modes of motion components that:

$$\phi_R^{(1)} = -i\omega \sum\nolimits_{m=1}^{6} \sum\nolimits_{N_i=1}^{N_i=N} (\xi_m^{(1)N_i} \phi_m^{(1)N_i}) \tag{2.4}$$

where N_i is the i-th body in multi-body platform system with total number of bodies N. $\xi_m^{(1)N_i}$ is the first-order complex amplitude of the oscillatory motion in mode of the i-th body of multi-body platform system in m-th DOF. $\phi_m^{(1)N_i}$ is the first-order unit-amplitude radiation potential (specifically, unit amplitude means the unit-amplitude linear or angular velocity of the rigid body motion). These modes are referred to as surge, sway, heave, roll, pitch and yaw in the increasing order of "m". The N_i=1,2⋯N is the order of the platform of each body in multi-body system.

The first-order radiation potential of platform N_i (N=1,2,⋯N_i⋯N_j⋯N) can be obtained by solving the BVPs:

$$\nabla^2\phi_m^{(1)N_i} = 0 \qquad \text{in fluid domain} \tag{2.5}$$

$$-\omega^2\phi_m^{(1)N_i} + g\frac{\partial\phi_m^{(1)N_i}}{\partial z} = 0 \quad \text{at free surface} \tag{2.6}$$

$$\frac{\partial\phi_m^{(1)N_i}}{\partial z} = 0 \qquad \text{at sea bottom} \tag{2.7}$$

$$\frac{\partial\phi_m^{(1)N_i}}{\partial n} = n_m^{N_i} \qquad \text{on mean wet surface of } \boldsymbol{N_i} \text{ platform} \tag{2.8a}$$

$$\frac{\partial\phi_m^{(1)N_j}}{\partial n} = 0 \qquad \text{on mean wet surface of } \boldsymbol{N_j} \text{ platform} \tag{2.8b}$$

$$\lim_{R\to\infty}\sqrt{R}\left(\frac{\partial\phi_m^{(1)N_i}}{\partial R} - ik\phi_m^{(1)N_i}\right) = 0 \qquad \text{in far field} \tag{2.9}$$

where $R = \sqrt{x^2 + y^2 + z^2}$, $n_m^{N_i}$ is the generalized normal vectors of the N_i body surface, N_j is the j-th body in multi-platform system with $j=1...N$ and $j \neq i$.

$$n_m^{N_i} = \begin{cases} \vec{n} & m = 1,2,3 \\ (x,y,z)\times\vec{n} & m = 4,5,6 \end{cases} \tag{2.10}$$

$\vec{n}$ is the unit normal vector pointing towards the body surface, (x,y,z) is the position vector on body surface.

The first-order diffraction potential $\phi_D^{(1)}$ also satisfies the Laplace equation and boundary conditions on free surface and N_i body boundary:

$$\nabla^2\phi_D^{(1)} = 0 \qquad \text{in fluid domain} \tag{2.11}$$

$$-\omega^2\phi_D^{(1)} + g\frac{\partial\phi_D^{(1)}}{\partial z} = 0 \qquad \text{at free surface} \tag{2.12}$$

$$\frac{\partial\phi_D^{(1)}}{\partial z} = 0 \qquad \text{at sea bottom} \tag{2.13}$$

$$\frac{\partial\phi_D^{(1)}}{\partial n} = -\frac{\partial\phi_I}{\partial n} \qquad \text{on mean wet surface of } N_i,\ i=1\cdots N \tag{2.14}$$

$$\lim_{R\to\infty}\sqrt{R}\left(\frac{\partial\phi_D^{(1)}}{\partial R} - ik\phi_D^{(1)}\right) = 0 \qquad \text{in far field} \tag{2.15}$$

where $R = \sqrt{x^2 + y^2 + z^2}$.

It should be noted that the far-field condition is necessary since the diffract wave should translate outward the body rather than inward body surface. For example, if $\phi_D^{(1)} = -\phi_I^{(1)}$, it satisfies Laplace equation (2.11) and boundary conditions from (2.12) to (2.14). However, the direction of the diffract wave becomes the single direction which is not correct. The far-field condition (2.15) is added to make that the wave energy is passing outward of the body.

2.4 The second-order problem in multi-platform

In second-order problem, the incident wave is considered as bi-chromatic wave with two frequencies ω_i and ω_j. The second-order velocity potential $\Phi^{(2)}(x,y,z,t)$ is decomposed into sum- and difference-frequency terms:

$$\Phi^{(2)}(x,y,z,t) = Re\sum_i\sum_j \phi_{ij}^{+}(x,y,z)e^{-i(\omega_i+\omega_j)t} + \phi_{ij}^{-}(x,y,z)e^{-i(\omega_i-\omega_j)t} \tag{2.16}$$

Here, the ϕ_{ij}^{+} and ϕ_{ij}^{-} are referred to as the sum- and difference-frequency velocity potential with frequencies.

As in the first-order, the second-order velocity potential can be decomposed into three components, the second-order incident wave potential $\phi_I^{\pm}$, the second-order diffracting wave potential $\phi_D^{\pm}$ and the second-order radiation potential $\phi_R^{\pm}$.

The second-order sum- and difference-frequency components of the incident potentials $\phi_I^{\pm}$ can be expressed as:

$$\phi_I^+(x) = \frac{1}{2}(q_{ij}^+ + q_{ji}^+)\frac{\cosh\ k^+(z+h)}{\cosh\ k^+h}e^{ik^+x} \tag{2.17}$$

$$\phi_I^-(x) = \frac{1}{2}(q_{ij}^- + q_{ji}^{-*})\frac{\cosh\ k^-(z+h)}{\cosh\ k^-h}e^{ik^-x} \tag{2.18}$$

where $k^{\pm} = k_i \pm k_j$ is the wavenumber and

$$q_{ij}^+ = -\frac{igA_iA_j}{2\omega_i}\frac{k_i^2-\nu_i^2+2k_ik_j-2\nu_i\nu_j}{\nu^+-k^+\tanh\ k^+h} \tag{2.19}$$

$$q_{ij}^- = -\frac{igA_iA_j^*}{2\omega_i}\frac{k_i^2-\nu_i^2-2k_ik_j-2\nu_i\nu_j}{\nu^--k^-\tanh\ k^-h} \tag{2.20}$$

where $\nu^{\pm} = \frac{(\omega_i \pm \omega_j)^2}{g}$

It is noted that the radiation described the disturbance due to the second-order motion of body and linearly proportional to the motion amplitude.

$$\phi_R^{\pm} = -i(\omega_i \pm \omega_j)\sum_{m=1}^{6}\ \sum_{N_i=1}^{N_i=N}\ (\xi_m^{(2)N_i}\phi_m^{(2)N_i}) \tag{2.21}$$

$\xi_m^{(2)N_i}$ is the second-order complex amplitude of the oscillatory motion in mode of *i*-th body of multi-body platform system in *m*-th DOF. $\phi_m^{(2)N_i}$ is the second-order unit-amplitude radiation potential (specifically, unit amplitude means the unit-amplitude linear or angular velocity of the rigid body motion). The N_i is the *i*-th body in multi-body platform system with total number of bodies *N* which is the same with the definition of that in first-order problem in Section 2.3.

Similarly, the second-order radiation potential of i-th platform N_i can be obtained by solving the BVPs:

For oscillating platform N_i and other platform fixed:

$$\nabla^2\phi_m^{\pm N_i} = 0 \qquad \text{in fluid domain} \tag{2.22}$$

$$-\left(\omega_i \pm \omega_j\right)^2 \phi_m^{\pm N_i} + g\frac{\partial \phi_m^{\pm N_i}}{\partial z} = 0 \quad \text{at free surface} \tag{2.23}$$

$$\frac{\partial \phi_m^{\pm N_i}}{\partial z} = 0 \qquad \text{at sea bottom} \tag{2.24}$$

$$\frac{\partial \phi_m^{\pm N_i}}{\partial n} = n_m^{N_i} \qquad \text{on mean wet surface of } \boldsymbol{N_i} \text{ platform} \tag{2.25}$$

$$\frac{\partial \phi_m^{\pm N_j}}{\partial n} = 0 \qquad \text{on mean wet surface of } \boldsymbol{N_j} \text{ platform} \tag{2.26}$$

$$\lim_{R\to\infty} \sqrt{R}\left(\frac{\partial \phi_R^{\pm N_i}}{\partial R} - ik\phi_R^{\pm N_i}\right) = 0 \qquad \text{in far field} \tag{2.27}$$

where $R = \sqrt{x^2 + y^2 + z^2}$, $n_m^{N_i}$ is the generalized normal vectors of the N_i body surface, N_j is the *j*th body in multi-platform system with *j=1…N* and $j \neq i$. $n_m^{N_i}$ is defined same with that in Eq (2.11). It should be noted that the wave number *k* in Eq (2.27) should satisfy that:

$$k\tanh(kd) = \frac{(\omega_i \pm \omega_j)^2}{g} \tag{2.28}$$

The second-order diffraction wave potential satisfies the Laplace equation and the boundary conditions at the free surface with forcing term, bottom condition, the conditions on the body surface and the far field condition.

$$\nabla^2 \phi_D^{\pm} = 0 \qquad \text{in fluid domain} \tag{2.29}$$

$$-(\omega_i + \omega_j)^2 \phi_D^{\pm} + g\frac{\partial \phi_D^{\pm}}{\partial z} = Q_F^{\pm} \text{ at free surface} \tag{2.30}$$

$$\frac{\partial \phi_D^{\pm}}{\partial z} = 0 \qquad \text{at sea bottom} \tag{2.31}$$

$$\frac{\partial \phi_D^{\pm}}{\partial n} = Q_B^{\pm} \qquad \text{on mean wet surface of platform } \mathbf{I} \tag{2.32}$$

$$\frac{\partial \phi_D^{\pm}}{\partial n} = Q_B^{\pm} \qquad \text{on mean wet surface of platform } \mathbf{II} \quad (2.33)$$

$$\lim_{R \to \infty} \sqrt{R} \left(\frac{\partial \phi_D^{\pm}}{\partial R} - ik\phi_D^{\pm} \right) = 0 \qquad \text{in far field} \quad (2.34)$$

There are inhomogeneous terms in equation of free surface condition ($Q_F^{\pm}$) and body boundary condition ($Q_B^{\pm}$) defining the quadratic forcing functions (WAMIT theory manual, 1995).

In accordance with the definition of second-order potential (2.16), the forcing term Q_F and Q_B which is time dependent can be expressed in similar form:

$$Q_{F,B}(x, y, z, t) = Re \sum \sum [Q_{F,B\ ij}^{+}(x, y, z)e^{i(\omega_i + \omega_j)t} + Q_{F,B\ ij}^{-}(x, y, z)e^{i(\omega_i - \omega_j)t}] \quad (2.35)$$

With the symmetry condition:

$$Q_{F,B\ ij}^{+} = Q_{F,B\ ji}^{+}, Q_{F,B\ ij}^{-} = Q_{F,B\ ji}^{-*} \quad (2.36)$$

Second-order quantities can be expressed in a form of equation (2.35) with symmetry condition in (2.36). To simplify the expression, the subscript *i,j* will be omitted hereafter. The expression for the complex amplitudes of the free-surface forcing functions is:

$$Q_F^{+} = \frac{i}{4g}\omega_i \phi_i \left(-\omega_j^2 \frac{\partial \phi_j}{\partial z} + g \frac{\partial^2 \phi_j}{\partial z^2} \right) + \frac{i}{4g}\omega_j \phi_j \left(-\omega_i^2 \frac{\partial \phi_i}{\partial z} + g \frac{\partial^2 \phi_i}{\partial z^2} \right) - \frac{1}{2} i(\omega_i + \omega_j) \nabla \phi_i \cdot \nabla \phi_j$$

(2.37)

$$Q_F^{-} = \frac{i}{4g}\omega_i \phi_i \left(-\omega_j^2 \frac{\partial \phi_j^*}{\partial z} + g \frac{\partial^2 \phi_j^*}{\partial z^2} \right) + \frac{i}{4g}\omega_j \phi_j^* \left(-\omega_i^2 \frac{\partial \phi_i}{\partial z} + g \frac{\partial^2 \phi_i}{\partial z^2} \right) - \frac{1}{2} i(\omega_i - \omega_j) \nabla \phi_i \cdot \nabla \phi_j^*$$

(2.38)

It should be noted that the ϕ_i and ϕ_j are the first-order potential which contains the incident wave potential, diffraction potential and radiation potential.

Then, the sum- and difference-frequency forcing on body boundary are given by

$$Q_B^+ = -\frac{\partial \phi_I^+}{\partial n} + \frac{i(\omega_i+\omega_j)}{2}\vec{n}\cdot H^+\mathbf{x} + \frac{1}{4}\left[(\boldsymbol{\alpha}_i \times \vec{n})\cdot\left(i\omega_j\left(\boldsymbol{\delta}_j + \boldsymbol{\alpha}_j \times \mathbf{x}\right) - \nabla\phi_j\right) + \left(\boldsymbol{\alpha}_j \times \vec{n}\right)\cdot\right.$$

$$\left.(i\omega_i(\boldsymbol{\delta}_i + \boldsymbol{\alpha}_i \times \mathbf{x}) - \nabla\phi_i)\right] - \frac{1}{4}\vec{n}\cdot[\left((\boldsymbol{\delta}_i + \boldsymbol{\alpha}_i \times \mathbf{x})\cdot\nabla\right)\nabla\phi_j + ((\boldsymbol{\delta}_j + \boldsymbol{\alpha}_j \times \mathbf{x})\cdot\nabla)\nabla\phi_i] \quad (2.39)$$

$$Q_B^- = -\frac{\partial \phi_I^-}{\partial n} + \frac{i(\omega_i-\omega_j)}{2}\vec{n}\cdot H^-\mathbf{x} + \frac{1}{4}\left[(\boldsymbol{\alpha}_i \times \vec{n})\cdot\left(-i\omega_j\left(\boldsymbol{\delta}_j^* + \boldsymbol{\alpha}_j^* \times \mathbf{x}\right) - \nabla\phi_j^*\right) + \left(\boldsymbol{\alpha}_j^* \times \vec{n}\right)\cdot\right.$$

$$\left.(i\omega_i(\boldsymbol{\delta}_i + \boldsymbol{\alpha}_i \times \mathbf{x}) - \nabla\phi_i)\right] - \frac{1}{4}\vec{n}\cdot[\left((\boldsymbol{\delta}_i + \boldsymbol{\alpha}_i \times \mathbf{x})\cdot\nabla\right)\nabla\phi_j^* + ((\boldsymbol{\delta}_j^* + \boldsymbol{\alpha}_j^* \times \mathbf{x})\cdot\nabla)\nabla\phi_i] \quad (2.40)$$

where $H^{\pm}$ is the quadratic components of the coordinate transformation matrix due to the rotation of body (from body fixed coordinates to inertial reference frame), $\boldsymbol{\delta} = (\delta_1, \delta_2, \delta_3)$ and $\boldsymbol{\alpha} = (\alpha_1, \alpha_2, \alpha_3)$ are the translational and rotational displacements of body fixed coordinates with respect to inertial reference frame at original position. (*) denotes the complex conjugate. $\mathbf{x} = (x, y, z)$ is the position vector on the body surface.

2.5 Integral equation method and Green function

The integral equation method is applied to solve the boundary value problem. The first-order diffraction potential and radiation potential can be obtained from the integral equation,

$$2\pi\phi_D(\mathbf{x}) + \iint_{S_B} d\boldsymbol{\zeta}\phi_D(\boldsymbol{\zeta})\frac{\partial G(\zeta;\mathbf{x})}{\partial n_\zeta} = \iint_{S_B} d\boldsymbol{\zeta}(-\frac{\partial \phi_I}{\partial n})G(\boldsymbol{\zeta};\mathbf{x}) \quad (2.41)$$

$$2\pi\phi_m(\mathbf{x}) + \iint_{S_B} d\boldsymbol{\zeta}\phi_m(\boldsymbol{\zeta})\frac{\partial G(\zeta;\mathbf{x})}{\partial n_\zeta} = \iint_{S_B} d\boldsymbol{\zeta} n_m G(\boldsymbol{\zeta};\mathbf{x}) \quad (2.42)$$

where S_B denotes the body boundary. The $G(\boldsymbol{\zeta};\mathbf{x})$ is the Green function which is referred to as wave source potential. It presents the velocity potential at the point $\mathbf{x}$ due to a point source of strength -4π at the point $\boldsymbol{\zeta}$. The fluid velocity can be calculated through the source strength σ. The σ_m represents the source strength of radiation potential and σ_D corresponds to the diffraction potential. The integral equation for the source strength of diffraction and radiation can be expressed as:

$$2\pi\sigma_D(\mathbf{x}) + \iint_{S_B} d\boldsymbol{\zeta}\sigma_D(\boldsymbol{\zeta})\frac{\partial G(\zeta;\mathbf{x})}{\partial n_{\mathbf{x}}} = -\frac{\partial \phi_I}{\partial n} \quad (2.43)$$

$$2\pi\sigma_m(\mathbf{x}) + \iint_{S_B} d\boldsymbol{\zeta}\sigma_m(\boldsymbol{\zeta})\frac{\partial G(\zeta;\mathbf{x})}{\partial n_{\mathbf{x}}} = n_m \tag{2.44}$$

The fluid velocity due to the diffraction and radiation potential is obtained from

$$\nabla\phi(\mathbf{x}) = \nabla\iint_{S_B} d\boldsymbol{\zeta}\sigma(\boldsymbol{\zeta})G(\boldsymbol{\zeta};\mathbf{x}) \tag{2.45}$$

The integral equations of diffraction and radiation are solved by panel method. The unknown varieties are assumed constant over each panel and the integral is enforced in the centre of each panel. The discrete form of the Eq (2.41) to (2.44) are:

$$2\pi\phi_D(\mathbf{x}_p) + \sum_{n=1}^{Num}\phi_D(\mathbf{x}_n)\int_{S_n} d\boldsymbol{\zeta}\frac{\partial G(\zeta;\mathbf{x}_p)}{\partial n_\zeta} = \sum_{n=1}^{Num} -\frac{\partial\phi_I(\mathbf{x}_n)}{\partial n}\int_{S_n} d\boldsymbol{\zeta}\, G(\boldsymbol{\zeta};\mathbf{x}_p) \tag{2.46}$$

$$2\pi\phi_m(\mathbf{x}_p) + \sum_{n=1}^{Num}\phi_m(\mathbf{x}_n)\int_{S_n} d\boldsymbol{\zeta}\frac{\partial G(\zeta;\mathbf{x}_p)}{\partial n_\zeta} = \sum_{n=1}^{Num} n_m(\mathbf{x}_n)\int_{S_n} d\boldsymbol{\zeta}\, G(\boldsymbol{\zeta};\mathbf{x}_p) \tag{2.47}$$

$$2\pi\sigma_D(\mathbf{x}_p) + \sum_{n=1}^{Num}\sigma_D(\mathbf{x}_n)\int_{S_n} d\boldsymbol{\zeta}\frac{\partial G(\zeta;\mathbf{x}_p)}{\partial n_{\mathbf{x}}} = -\frac{\partial\phi_I(\mathbf{x}_n)}{\partial n} \tag{2.48}$$

$$2\pi\sigma_m(\mathbf{x}_p) + \sum_{n=1}^{Num}\sigma_m(\mathbf{x}_n)\int_{S_n} d\boldsymbol{\zeta}\frac{\partial G(\zeta;\mathbf{x}_p)}{\partial n_{\mathbf{x}}} = n_m(\mathbf{x}_n) \tag{2.49}$$

where the *Num* is the total number of panels and $\mathbf{x}_p$ is the coordinate of the centre of the *p*-th panel. According to Wehausen and Laitone (1960), the Green function in finite depth is defined by:

$$G(\boldsymbol{\zeta};\mathbf{x}) = \frac{1}{r} + \frac{1}{\ddot{r}} + 2\int_0^\infty dk\,\frac{(k+\nu)\cosh k(z+h)\cosh k(c+h)}{k\sinh kh - \nu\cosh kh}e^{-kh}J_0(kR) \tag{2.50}$$

where $r^2 = (x-a)^2 + (y-b)^2 + (z-c)^2$, $\ddot{r}^2 = (x-a)^2 + (y-b)^2 + (z+c+2h)^2$, the coordinates of $\boldsymbol{\zeta}$ is (*a*,*b*,*c*), $J_0(x)$ is the Bessel function of zero order. $R = \sqrt{(x-a)^2 + (y-b)^2}$ and $\nu \equiv \frac{\omega^2}{g}$. In this expression, the Fourier *k*-integration is indented above the pole on the real axis in order to enforce the radiation condition. In the equation (2.46-48), the influence due to the continuous distribution of the Rankine part of the wave source potential on a quadrilateral panel is evaluated based on the algorithms described in Newman

(1985). The remaining wave part of the Green function is evaluated based on the algorithms described in Newman (1992). The integration part over a panel is carried out using either one or four points Gauss quadrature. Further detail information can be obtained in the reference WAMIT Theory Manual (1995).

For the second-order solution, the solution of radiation potential is identical to that of a first-order radiation problem at the sum and difference frequencies. However, the solution of diffraction potential is different with that of first-order problem since the free surface condition and body boundary condition are inhomogeneous by the forcing term.

The solution of second-order diffraction potential $\phi_D^{\pm}$ is obtained from Green's integral equation.

$$2\pi\phi_D^{\pm} + \iint_{S_B} \phi_D^{\pm}(\boldsymbol{\zeta}) \frac{\partial G(\mathbf{x};\zeta)}{\partial n_\zeta} ds = \iint_{S_B} Q_B^{\pm}(\boldsymbol{\zeta}) G(\mathbf{x};\boldsymbol{\zeta}) ds + \frac{1}{g}\iint_{S_F} Q_F^{\pm}(\boldsymbol{\zeta}) G(\mathbf{x};\boldsymbol{\zeta}) ds \qquad (2.51)$$

where G is the wave source potential which is defined in (2.50).

The panel method is applied to solve the integral equation. The left side of Eq (2.50) is similar with the equation for the first-order potential, thus the discrete form is same with Eq (2.46). However, the right-side integral is different. The integral over mean wetted surface S_B is described first. For the fixed body, the evaluation $Q_B^{\pm}(\mathbf{x})$ only contains the normal velocity caused by the incident wave potential $\phi_I^{\pm}$. For the floating body, we first modify the terms involving the double spacial derivative of the first-order velocity potential by applying Stokes's theorem.

$$\begin{aligned}
&\iint_{S_B} ds G\{\vec{n}\cdot[(\boldsymbol{\delta}+\boldsymbol{\alpha}\times\mathbf{x})\cdot\nabla]\nabla\phi\} \\
&\qquad = \iint_{S_B} ds[\vec{n}\cdot(\boldsymbol{\delta}+\boldsymbol{\alpha}\times\mathbf{x})](\nabla\phi\cdot\nabla G) + \iint_{S_B} ds\, G\{\vec{n}\cdot[(\nabla\phi\cdot\nabla)(\boldsymbol{\delta}+\boldsymbol{\alpha}\times\mathbf{x})]\} \\
&\qquad - \iint_{S_B} ds\frac{\partial\phi}{\partial n}[(\boldsymbol{\delta}+\boldsymbol{\alpha}\times\mathbf{x})\cdot\nabla G] + \int_{WL} dl\cdot G[\nabla\phi\times(\boldsymbol{\delta}+\boldsymbol{\alpha}\times\mathbf{x})]
\end{aligned}$$

(2.52)

With substitution of Eq (2.52) to $Q_B^{\pm}$, the integral over S_B is replaced by a sum of integral over each panel with assumption that the $Q_B^{\pm}$ is constant on each panel. $Q_B^{\pm}$ is evaluated on the centroids of the panels. The waterline is approximated by line segments (consisting of the sides of the panels adjacent to the free surface) and $Q_B^{\pm}$ is evaluated on the midpoints of the segments (WAMIT Theory Manual, 1995).

The last term in Eq. (2.51) is the free surface integral term. $Q_F^{\pm}$ is substituted into the integral of the free surface. The integral is calculated in two domains divided by a partition circle with radius $\rho = b$. b is large enough to neglect the effect of the evanescent waves outside the circle (Wamit Theory Manual, 1995). According to Kim and Yue (1989), the integration in the inner domain is carried out numerically. In the outer domain both the Green function and the asymptotic of the first-order potentials are expanded in Fourier-Bessel series. After integrating the trigonometric functions with respect to the angular coordinate, the free-surface integrals are reduced to the sum of the line integrals with respect to the radial coordinate ρ. The detail can be founded in WAMIT theory manual (1995) and Kim and Yue (1989).

In the inner domain, the second-order derivatives of the first-order potential in the surface integral can be transformed into first-order derivatives and line integrals around the waterline (WL) and the partition circle (PC) by Gauss theorem (WAMIT Theory Manual, 1995).

$$\iint_{S_F} \phi_i \frac{\partial^2 \phi_j}{\partial z^2} G ds - \iint_{WL+PC} \phi_i (\nabla \phi_j \cdot \vec{n}) G dl + \iint_{S_F} [(\nabla \phi_i \cdot \nabla \phi_j) G + \phi_i (\nabla \phi_j \cdot \nabla G)] ds$$

(2.53)

where S_F denotes the inner domain of the free surface. The divergence ∇ and the normal vector $\vec{n}$ must be interpreted in the two-dimensional sense on the $z = 0$ plane. The detail of the discrete method for boundary value problem can be found in the reference Wamit Theory Manual (1995) and Kim &Yue (1989).

In the outer domain, the far-field behaviour of the general-order ring source, for $R/h \gg 1$, the G can be expressed as (John, 1950):

$$G = -2\pi i C_0 \cosh k(z+h) \cosh k(c+h) H_0(kR) +$$
$$4\sum_{m=1}^{\infty} C_m \cos\kappa_m(z+h)\cos\kappa_m(c+h)K_0(\kappa_m R) \tag{2.54}$$

where H_0, K_0 are the zeroth-order first-kind Hankel function and second-kind modified Bessel function. k is the incident wave number.

$$C_0 = \frac{\nu^2-k^2}{k^2h-\nu^2h+\nu}, \qquad C_m = \frac{\kappa_m^2+\nu^2}{\kappa_m^2h+\nu^2h-\nu} \tag{2.55}$$

κ_m with m=1,2,…. are the real roots of the equation.

$$\omega^2 = -\kappa_m g \tan\kappa_m h, \quad (m-\tfrac{1}{2})\pi \le \kappa_m h \le m\pi \tag{2.56}$$

For the finite water depth, the second term of Eq. (2.48) is reducing with radial distance, κ_m, R, far-field asymptotic of G is given by the first term which represents outgoing waves:

$$G = -2\pi i C_0 \cosh k(z+h)\cosh k(c+h) H_0(kR) + O(e^{-\kappa_1 R}) \tag{2.57}$$

The far-field asymptotic of the ring sources, upon using the addition theorem, is (Kim and Yue1989):

$$G_n = -4\pi^2 i C_0 \cosh k(z+h)\cosh k(c+h) J_n(k\rho') H_n(k\rho) + O(e^{-\kappa_1 R}) \tag{2.58}$$

2.6 First-order forces and moments

Once the diffraction potential and radiation potential are solved, the first-order hydrodynamic pressure can be calculated from the velocity potential:

$$p(x,y,z,t) = -\rho\frac{\partial\Phi^{(1)}(x,y,z,t)}{\partial t} = Re\{i\rho\omega\left[\phi_I^{(1)} + \phi_D^{(1)} - i\omega\sum_{m=1}^{6}\sum_{1}^{N}\ (\xi_m^{(1)N_i}\phi_m^{(1)N_i})\right]e^{-i\omega t}\}$$

(2.59)

where ρ is the fluid density. The hydrodynamic force on body N_i caused by radiation potential can be derived

$$F_R^{N_i} = Re\left\{\left[\sum_{N_i,N_j=1}^{N_i,N_j=N} \sum_{m,l=1}^{m,l=6}\left(\omega^2\mu_{km}^{N_iN_j} + i\omega\lambda_{km}^{N_iN_j}\right)\xi_m^{(1)N_i}\right]e^{-i\omega t}\right\} \tag{2.60}$$

The added mass μ and damping λ can be expressed as:

$$\mu_{lm}^{N_iN_j} = \rho Re\left\{\iint_{S_{N_i}} \phi_m^{(1)N_j}\frac{\partial\phi_k^{N_i}}{\partial n}ds\right\} \tag{2.61}$$

$$\lambda_{lm}^{N_iN_j} = \omega\rho Im\left\{\iint_{S_{N_i}} \phi_m^{(1)N_j}\frac{\partial\phi_k^{N_i}}{\partial n}ds\right\} \tag{2.62}$$

The S_{N_i} is the mean wet body surface of the *i*-th body in multi-body platform system with total number is *N*. *i* and *j* =1,2⋯*N*. $\mu_{lm}^{N_iN_j}$ is the added mass of body N_i in *l*-th mode which is induced by the motion of body N_j in *m*-th mode. It should be noted that the added mass and the damping coefficient are same to that for the individual body N_i if *i*=*j*. The subscripts *m*=1,2,…6 is defined in Section 2.3, the *l*=1,2,…6 represents the six degrees of freedom of motion (surge, sway, heave, roll, pitch and yaw respectively).

The incident wave and diffract wave force can also be obtained:

$$F_{I+D}^{N_i} = \iint_{S_{N_i}}(p_I + p_D)n_m^{N_i}ds \tag{2.63}$$

The pressure p_I and p_D are hydrodynamic pressure calculated by the incident wave and diffract wave according to Bernoulli equation,

$$p_I = -\rho\frac{\partial\Phi_I}{\partial t} = \rho Re\left\{i\omega\phi_I^{(1)}e^{-i\omega t}\right\} \tag{2.64}$$

$$p_D = -\rho\frac{\partial\Phi_D}{\partial t} = \rho Re\left\{i\omega\phi_D^{(1)}e^{-i\omega t}\right\} \tag{2.65}$$

The total first-order force $F^{(1)}$ can be expressed as:

$$F^{(1)} = F_I^{(1)} + F_D^{(1)} + F_R^{(1)} + F_{HS}^{(1)} \tag{2.66}$$

where $F_{HS}^{(1)}$ represent the first-order hydrostatic restoring force. The $F_I^{(1)} + F_D^{(1)}$ can be expressed as $F_{ex}^{(1)}$ which is the first-order wave exciting force.

The first-order surface elevation $\varsigma^{(1)}(t)$ can be expressed in the form same with Eq (2.2),

$$\varsigma^{(1)}(t) = -\frac{1}{g}\frac{\partial \Phi^{(1)}}{\partial t}|_{z=0} = Re\{\eta^{(1)}e^{-i\omega t}\} \tag{2.67}$$

where $\eta^{(1)}$ is calculated by

$$\eta^{(1)} = \frac{i\omega}{g}\phi^{(1)} \tag{2.68}$$

According to Eq (2.2), the time-independent first-order surface elevation is:

$$\eta^{(1)} = \frac{i\omega}{g}(\phi_I^{(1)} + \phi_D^{(1)} - i\omega \sum_{m=1}^{6} \sum_{1}^{N} \ (\xi_m^{(1)N_i}\phi_m^{(1)N_i})) \tag{2.69}$$

2.7 Second-order force and moment

As pointed out earlier, the second-order radiation problem for $\Phi_R^{(2)}$ is identical to that of the first-order radiation potential except for the change in frequencies, and the added mass and hydrodynamic damping coefficients for the second-order motions can be obtained similarly.

All second-order nonlinear aspects are contained in the second-order exciting force. The second-order exciting force can be written in the same form as Eq (2.16) and Eq (2.35):

$$F_{ex}^{(2)}(x, y, z, t) = Re \sum_{j=1}^{2} \sum_{i=1}^{2} [A_j A_i f_{ji}^{+} e^{-i\omega^{+}t} + A_j A_i^{*} f_{ji}^{-} e^{-i\omega^{-}t}] \tag{2.70}$$

Since the radiation is considered separately, there is only incident wave and diffraction wave force are considered in $F_{ex}^{(2)}(x, y, z, t)$. Thus, the quadratic transfer function (QTF) $f_{ji}^{\pm}$ of second-order exciting force can be expressed as:

$$f_{ji}^{\pm} = f_{qji}^{\pm} + f_{pji}^{\pm} \tag{2.71}$$

where the $f_{qji}^{\pm}$ is caused by quadratic first-order potential, $f_{pji}^{\pm}$ is caused by the second-order potential. These force QTFs can be expressed as:

$$f_{pji}^{+} = \left[\rho i(\omega_j + \omega_i) \iint_{S_B} (\phi_I^{+} + \phi_D^{+})\, \vec{n} ds\right] / A_j A_i \tag{2.72}$$

$$\begin{aligned} f_{qji}^{+} = \{ & -\tfrac{\rho}{4} \iint_{S_b} \left(\nabla\varphi_j^{(1)} \cdot \nabla\varphi_i^{(1)} - i\omega_i \boldsymbol{\xi}_{m,j}^{(1)} \cdot \nabla\varphi_i^{(1)} - i\omega_j \nabla\varphi_j^{(1)} \cdot \boldsymbol{\xi}_{m,i}^{(1)}\right)\vec{n} ds \\ & + \tfrac{\rho}{4} \iint_{S_b} \left(i\omega_i \varphi_i^{(1)} \theta_j^{(1)} \times \vec{n} + i\omega_j \varphi_j^{(1)} \theta_i^{(1)} \times \vec{n}\right) ds \\ & + \tfrac{\rho g}{4} \oint_{WL} \left(\eta_j^{(1)} \eta_i^{(1)} - \xi_{3,j}^{(1)} \eta_i^{(1)} + \xi_{3,i}^{(1)} \eta_j^{(1)}\right) \vec{n}_c dl \\ & - \tfrac{\rho g A_w}{4} [(\theta_{1,j}^{(1)} \theta_{3,i}^{(1)} + \theta_{1,i}^{(1)} \theta_{3,j}^{(1)})(x_f - x_c') + (\theta_{2,j}^{(1)} \theta_{3,i}^{(1)} + \theta_{2,i}^{(1)} \theta_{3,j}^{(1)})(y_f - y_c') \\ & + (\theta_{1,j}^{(1)} \theta_{1,i}^{(1)} + \theta_{2,j}^{(1)} \theta_{2,i}^{(1)}) z_c'] \vec{k} \} / A_j A_i \end{aligned} \tag{2.73}$$

where $\theta_{1,2,3} = \xi_{4,5,6}$ which represent the rotation amplitude in roll, pitch and yaw of the body respect to the reference coordinate system. $\vec{n}_c = \vec{n}/|cos\gamma|$, γ is the angle between normal vector $\vec{n}$ and horizontal plane and for wall-sided bodies at the waterline, $\vec{n}_c = \vec{n}$. $A_i$and A_j are the amplitude of the incident wave with frequencies ω_i and ω_j. (x_f, y_f) is the centre of the water plane. The expressions for the difference-frequency problem are similar and are not given here for brevity.

Similar to first-order force, the total second-order force can be separated into several parts:

$$F^{(2)} = F_I^{(2)} + F_D^{(2)} + F_R^{(2)} + F_{HS}^{(2)} + F_q^{(2)} \tag{2.74}$$

where $F_q^{(2)}$ represent the second-order force caused by quadratic first-order quantities. The total second-order force can be also expressed as:

$$F^{(2)} = F_{ex}^{(2)} + F_R^{(2)} + F_{HS}^{(2)} \;\; (F_{ex}^{(2)} = F_I^{(2)} + F_D^{(2)} + F_q^{(2)}) \tag{2.75}$$

where $F_{ex}^{(2)}$ represent the second-order exciting force which has already discussed above.

The second-order surface elevation $\varsigma^{(2)}(t)$ can be expressed as:

$$\varsigma^{(2)}(t) = Re \sum_{j=1}^{2} \sum_{i=1}^{2} [\eta_{ji}^{+} e^{-i\omega^{+}t} + \eta_{ji}^{-} e^{-i\omega^{-}t}] \tag{2.76}$$

where the $\eta_{ji}^{\pm}$ can be decomposed into:

$$\eta_{ji}^{\pm} = \eta_{pji}^{\pm} + \eta_{qji}^{\pm} \tag{2.77}$$

The components of sum and difference frequency can be calculated:

$$\eta_{qji}^{+} = -\frac{1}{4g} \nabla\phi_j^{(1)} \nabla\phi_i^{(1)} - \frac{\omega_j \omega_i (\nu_j + \nu_i)}{4g^2} \phi_j^{(1)} \phi_i^{(1)} \tag{2.78}$$

$$\eta_{qji}^{-} = \frac{1}{4g} \nabla\phi_j^{(1)} \nabla\phi_i^{(1)} + \frac{\omega_j \omega_i (\nu_j + \nu_i)}{4g^2} \phi_j^{(1)} \phi_i^{(1)} \tag{2.79}$$

$$\eta_{pji}^{\pm} = \frac{i\omega^{\pm}}{g} \phi^{\pm} \tag{2.80}$$

For monochromatic wave that $\omega_i = \omega_j$, the difference-frequency component η_{ji}^{-} becomes constant component $\bar{\eta}$. The sum-frequency component η_{ji}^{+} becomes the double frequency component. In the present study, the double-frequency is expressed as $\eta^{(2)}$ to distinguish with the sum-frequency component η_{ji}^{+}.

2.8 Wind and current force

The wind and current force are calculated by the wind and current coefficients which are confirmed according to the DNV GL guideline (DNV-RP-C205). The wind and current force are calculated as follow and regarded as a constant force in the simulation:

$$F_{wind} = \frac{1}{2} C_w \rho_\alpha A_w U^2 \tag{2.81}$$

$$M_{wind} = \frac{1}{2} C_w \rho_\alpha A_w U^2 L \tag{2.82}$$

$$F_{current} = \frac{1}{2} C_c \rho_w A_c V^2 \tag{2.83}$$

$$M_{current} = \frac{1}{2} C_c \rho_w A_c V^2 L \tag{2.84}$$

C_w is the wind coefficient; ρ_α is the air density; A_w is the shadow area; U is the relative wind speed on the platform; C_c is the current coefficient; ρ_w is the fluid density; A_c is the shadow area in current direction; V is the current speed; L is the distance from force to centre of gravity.

2.9 Motion equation

The motion of the platform N_i is solved based on the hydrodynamic coefficients and wave loads mentioned previously, the motion equations for multi-body system in frequency domain can be expressed as:

$$\left[-\omega^2(M^{N_i} + \mu^{N_i N_i}) + i\omega\lambda^{N_i N_i} + C^{N_i} + K_H^{N_i} + K_M^{N_i}\right]\xi^{N_i}(\omega) + \left(-\omega^2\mu^{N_i N_j} + i\omega\lambda^{N_i N_j} - K_H^{N_j}\right)\xi^{N_j}(\omega) = F_{ex}^{N_j}(\omega) \tag{2.85}$$

It should be noted that the mass M, added mass μ damping coefficient λ and stiffness are k*m (6*6) matrix. The C is the hydrostatic restoring matrix, the K_H represents the stiffness caused by connecting hawsers and K_M is the stiffness provided by mooring lines. The frequency-domain motion amplitude $\xi^{N_i}(\omega)$ is 6*1 vectors for ith body. The sum-and difference frequency responses are also contained in equations which are same with first-order response except for the change in frequencies. Because the mooring and hawsers' force are contained in the left side, the mooring force is not required in the right side. In the frequency domain analysis, the stiffness caused by mooring lines and hawsers are regarded as constant. The stiffness of each line and hawsers are listed in the lines' properties in case study. The mass matrix and hydrostatic restoring matrix can be expressed as:

$$M = \begin{bmatrix} m & 0 & 0 & 0 & mz_G & 0 \\ 0 & m & 0 & -mz_G & 0 & mx_G \\ 0 & 0 & m & 0 & -mx_G & 0 \\ 0 & -mz_G & 0 & I_{44} & 0 & I_{46} \\ mz_G & 0 & -mx_G & 0 & I_{55} & 0 \\ 0 & mx_G & 0 & I_{64} & 0 & I_{66} \end{bmatrix} \tag{2.86}$$

$$C = \begin{bmatrix} 0 & 0 & 0 & 0 & 0 & 0 \\ 0 & 0 & 0 & 0 & 0 & 0 \\ 0 & 0 & \rho g A_p & 0 & -\rho g M_p & 0 \\ 0 & 0 & 0 & \rho g(A_p d_2^2 + V z_B) & 0 & 0 \\ 0 & 0 & -\rho g M_p & 0 & \rho g(A_p d_1^2 + V z_B) & 0 \\ 0 & 0 & 0 & 0 & 0 & 0 \end{bmatrix} \tag{2.87}$$

where m is the body mass; (x_G, y_G, z_G) is the center of gravity; I_{44}, I_{55}, I_{66} are the roll, pitch and yaw moments of inertia; the roll-yaw moment of inertia holds the symmetry relation $I_{46} = I_{64}$; A_p is the water plane area; M_p is the waterplane moment of about y-axis. d_1, d_2 are the radius of inertia of waterplane about x-axis and y-axis. V is the underwater volume; z_B is the vertical center of buoyancy.

The impulse response theory is adopted to describe the motion equations in time domain. The motion equation of platform N_i can be expressed as:

$$[M^{N_iN_i} + \mu^{N_iN_i}(\infty)]\ddot{x}^{N_i}(t) + \int_{-\infty}^{t} \kappa^{N_iN_i}(t-\tau)\dot{x}^{N_i}(\tau)d\tau + C^{N_i}x^{N_i}(t) + \mu^{N_iN_j}(\infty)\ddot{x}^{N_j}(t) + \int_{-\infty}^{t} \kappa^{N_iN_j}(t-\tau)\dot{x}^{N_j}(\tau)d\tau = F_{ex}^{N_i} + F_H^{N_i} + F_M^{N_i} + F_W^{N_i} + F_C^{N_i} \tag{2.88}$$

It should be noted that the term with $\kappa(t-\tau)$ is the convolution term of velocity, which embodies the memory effect of the reaction force of fluid dynamics. $\kappa(t)$ is the retardation function. The added mass and damping coefficient calculated above are frequency-dependent have the relationship:

$$\mu_{lm}(\omega) = \mu_{lm}(\infty) + \int_0^{\infty} \kappa_{km}(\tau) cos\omega\tau d\tau \tag{2.89}$$

$$\lambda_{lm}(\omega) = \omega \int_0^{\infty} \kappa_{lm}(\tau) sin\omega\tau d\tau \tag{2.90}$$

To simplify the function, the subscripts are omitted. The relationship between retardation function and frequency-dependent damping are obtained by FFT of the equation (2.90):

$$\kappa(t) = \frac{2}{\pi}\int_0^{\infty} \lambda(\omega)\frac{sin\omega\tau}{\omega} d\omega \tag{2.91}$$

The wave excitation force in frequency domain $F_{ex}(\omega)$ can be transferred to time domain excitation force $F_{ex}(t)$ according to the impulse theory. Let:

$$F_{ex}(t) = \int_{-\infty}^{t} h(t-\tau)\varsigma(\tau)d\tau \tag{2.92}$$

where $\varsigma(\tau)$ is the wave coordinate of wave at time τ. $F_{ex}(t) = h(t)$ is the impulse response. $h(t)$ have the Fourier relationship with the frequency response.

$$F_{ex}(\omega) = \int_{-\infty}^{+\infty} h(t)e^{-i\omega t}dt \tag{2.93}$$

$$h(t) = \frac{1}{2\pi}\int_{-\infty}^{+\infty} F_{ex}(\omega)e^{-i\omega t}d\omega \tag{2.94}$$

In the equations, the wave excitation force in frequency domain can be obtained according to the diffraction theory in frequency domain. The impulse function $h(t)$ can be calculated according to the equation above. With multiplying the wave amplitude time history $\varsigma(\tau)$, the wave excitation force in time domain can be obtained in Eq (2.93).

Based on the relationship between frequency domain and time domain, the added mass, damping coefficient and wave force can be calculated in the frequency domain. Then, the retardation function and wave force in time domain can be achieved. The force coming from mooring lines and hawsers are calculated in time domain with updating stiffness at each time step (It is introduced in the following section 2.11). With the solution of the wave force in time domain and the retardation function, the motion response can be obtained by motion equation in time domain.

2.10 Morison equation

The total hydrodynamic force operated on the slender structures like tethers, mooring lines and risers are calculated according to Morison equation. The diffract effect of the slender structures are omitted since the diameter is very small ($\frac{D}{\lambda} < 0.2$). The formular can be expressed as:

$$F = \rho V\dot{u} + \rho C_a V(\dot{u} - \dot{v}) + \frac{1}{2}\rho C_d A(u - v)|u - v| \tag{2.95}$$

where u and $\dot{u}$ is the water velocity and acceleration which is the incident wave velocity and acceleration in the present study. The C_a is the added mass coefficient. C_d is the drag coefficient and A is the crossing area of the slender elements. The first term in right side the Froude–Krylov force, second term is the hydrodynamic mass force and the third term is the drag force in the slender elements.

2.11 Time domain coupled analysis of mooring system and floating bodies

A time domain coupled analysis was applied to calculate the motion equations of the multi-platform system in the full 6 DOF taking into account the fully coupled effects of the attached tendons, mooring lines and risers. The TLP and TAD are included as rigid body nodal components in the three-dimensional finite element model, of 6-DOF, and with full arrangement of the tendons, mooring lines and risers each being represented as a line of finite elements representing slender structures.

There are two main steps are contained in the time domain coupled analysis. The first step namely static analysis is that calculating the static equilibrium position according to the kinetics parameters (added mass, damping matrix and hydrostatic matrix) getting from the frequency domain analysis. The second step namely dynamic analysis is operating the coupled dynamic analysis in time domain. The equilibrium position calculated in the static analysis will be applied as the original position in dynamic analysis.

The effect of the mooring system (mooring lines, tethers and risers) is taken into account. Each platform is included as rigid body point component in the 3D finite element method (FEM) with full arrangement of the mooring lines and risers each being represented as a line of finite elements representing slender structures (Riflex-4.12.2, 2018).

The dynamic equilibrium of a spatially discretized finite element system model can in general be expressed as (Riflex Theory manual, 2018):

$$R^I(r,\ddot{r},t) + R^D(r,\dot{r},t) + R^s(r,t) = R^E(r,\dot{r},t) \tag{2.96}$$

where R^I is the inertia force vector, R^D is the damping force vector, R^s is the internal structural reaction force vector (contact forces are also treated as internal forces), R^E is the external force vector (External force vector assembled from all elements. Accounts for specified external forces, rigid body forces for representation of buoys, clump weights etc. and contribution from distributed loading, i.e., weight, buoyancy and wave forces on rigid body point). $r, \dot{r}, \ddot{r}$ is the structural displacement, velocity, and acceleration vector. All force vectors are established by assembly of element contributions and specified discrete nodal forces.

The inertia force vector can be expressed as:

$$R^I(r,\ddot{r},t) = [M^S + M^F(r) + M^H(r)]\ddot{r} \tag{2.97}$$

M^S is the structural mass matrix; $M^F(r)$ is the mass matrix accounting for internal fluid flow. Since there is no internal fluid is considered in the present study, this term is set zero. $M^H(r)$ is displacement-dependent hydrodynamic mass matrix accounting for the structural acceleration terms in the Morison equation as added mass contributions in local directions.

The damping force vector is expressed as:

$$R^D(r,\dot{r}) = [C^s(r) + C^H(r)]\dot{r} \tag{2.98}$$

$C^s(r)$ is the internal structural damping. $C^H(r)$ is the hydrodynamic damping matrix accounting for diffraction effects for floating, partly submerged elements.

The internal reaction force vector $R^s(r,t)$ is calculated based on the instantaneous state of stress in each of the various elements of the whole system. The external load vector $R^E(r, \dot{r}, t)$ considers the weight and buoyancy for each element, forced displacements, environmental forces and other specific forces.

The distinguish feature among analysis module is that how the nonlinearity is treated in the analysis. Step-by-step numerical integration of the incremental dynamic equilibrium equations, with a Newton-Raphson type of equilibrium iteration at each time step. This approach allows for a proper treatment of all the described nonlinearities. Nonlinear dynamic analysis is, however, rather time consuming due to repeated assembly of system matrices (mass, damping and stiffness) and triangularisation during the iteration process at each time step.

The incremental form of the dynamic equilibrium equation, Eq. (2.96), is obtained by considering dynamic equilibrium at two configurations a short time interval Δt apart:

$$(R^I_{t+\Delta t} - R^I_t) + (R^D_{t+\Delta t} - R^D_t) + (R^S_{t+\Delta t} - R^S_t) = (R^E_{t+\Delta t} - R^E_t) \qquad (2.99)$$

The equation above states that the increment in external loading is balanced by increments inertia-, damping- and structural reaction forces over the time interval Δt.

For numerical solution, the nonlinear incremental equation of motion is linearized by introducing the tangential mass-, damping- and stiffness matrices at the start of the increment. The linearized incremental equation of motion can be expressed as:

$$M_t \Delta \ddot{r}_t + C_t \Delta \dot{r}_t + K_t \Delta r_t = \Delta R^E_t \qquad (2.100)$$

where M_t, C_t, and K_t denote denote the tangential mass-, damping- and stiffness matrices computed at time *t*. Δr_t, $\Delta \dot{r}_t$, $\Delta \ddot{r}_t$ and ΔR^E_t are the incremental displacement, velocity, acceleration and external force vectors.

After introducing the tangential mass, damping and stiffness matrices at start of the next time increment, and with the implementation of the residual force vector from the previous time step, the linearized incremental equation of motion is given by:

$$M_t \Delta \ddot{r}_t + C_t \Delta \dot{r}_t + K_t \Delta r_t = R^E_{t+\Delta t} - (R^I_t + R^D_t + R^S_t) \tag{2.101}$$

The numerical solution is then established on an incremental technique using a dynamic time integration scheme according to the Newmark β-family methods. The dynamic equilibrium at the end of the time step is obtained using a Newton-Raphson type of equilibrium iteration. Further details of these two methods can be founded in Riflex Theory Manual (2018).

By rewriting Eq. (2.100) for dynamic equilibrium at time $t + \Delta t$ and applying the Newmark β-family method, the incremental equation expressed by the incremental displacement vector over the time interval $\Delta t + \theta \Delta \tau$, is written:

$$\widehat{K}_t \Delta r_t = \Delta \widehat{R}_t \tag{2.102}$$

$\widehat{K}_t$ is the effective stiffness and $\Delta \widehat{R}_t$ is the effective incremental load vector. According to the Newmark β-family method, they are defined by:

$$\widehat{K}_t = \frac{1}{\beta (\Delta t)^2} M_t + \frac{\gamma}{\beta \Delta t} C_t + K_t \tag{2.103}$$

$$\Delta \hat{R}_t = R^E_{t+\Delta t} - (R^I_t + R^D_t + R^S_t) + (\frac{1}{\beta \Delta t} \dot{r}_t + \frac{1}{2\beta} \ddot{r}_t) + C_t(\frac{\gamma}{\beta} \dot{r}_t + (\frac{\gamma}{2\beta} - 1)\Delta t \ddot{r}_t) \tag{2.104}$$

In Eq (2.102-104), the parameters γ, β, and θ are the time integration parameters based on the Newmark β-family methods. Further details regarding the numerical time integration methods are given in standard textbooks on structural dynamics, see for instance Langen and Sigbjørnsson (1979) and Clough and Penzien (1975).

3 Nonlinear surface elevation around multiple columns structures

Surface elevation around multiple columns offshore structure is an important phenomenon crucial to air gap design of offshore platforms. This chapter investigates the competing hydrodynamic phenomena, i.e., wave run-up of surface elevation rising along the column and near-trapping – the increase of surface elevation due to near-resonance among the columns. Both wave run-up and near-trapping have the characteristics of generating surface elevation peak, and often impacts the offshore structures with nonlinear wave loads and potentially causes slamming to platforms. A comprehensive numerical study is conducted to examine the wave run-up along columns and near-trapping around multiple columns structures. With the wave parameters range of $KC=A/a<\boldsymbol{O}(\mathbf{1})$($A$ is the incident wave amplitude, a is the radius of column and KC is short for Keulegan-Carpenter number) and wave steepness $H/L<0.14$ considered (H is the incident wave hight and L is the incident wavelength), the free surface amplitude primarily depends on the diffraction pattern caused by the multiple columns and potential theory is applicable. The wave run-up and near-trapping due to wave interaction with a platform consisting of four-square columns with different corner radii are obtained by numerical simulations. It is found that the corner radius can leads to significant difference in surface elevation characteristics under difference directions of incident waves. Two mechanisms namely superposition and near-resonance resulting the peak surface elevation are examined in detail for wave interaction with multiple columns. Surface elevation around multiple columns structures are discussed in the following section (Ren and Tao, 2020, Ren et al., 2021a).

3.1 Model configurations and mesh convergence

3.1.1 Model configurations

Regular wave is considered with the incidence of 0° and 45° respectively. For nonlinear analysis, the incident wave is perturbed to the second-order, both the quadratic first-order potential term and the second-order potential term are taken into consideration in the calculation of surface elevation. Sum- and difference-frequencies contribution to the surface elevation and inline force are also calculated. All simulations are carried out by hydrodynamic program WAMIT through commercial software SESAM.

The principal dimensions of cylinders analysed in the study are given in Table 3.1 and the wave conditions are shown in Table 3.2. The arrangements of the columns with different cross-sections are shown in Figure 3.1.

Table 3.1. The dimension of cylinders

Cylinder type	**Diameter**	**Leg spacing**	**Corner-ratio**
Circular column	*D*	Single, Four-columns 2*D*	---
Sharp corner column	*D*	Single, Four-columns 2*D*	---
Rounded corner-square column	*D*	Single, Four-columns *2D*	1/3,1/4 and 1/6

Table 3.2 Wave conditions in the numerical simulation (*ka* is scatter parameter)

Wave Conditions	**Scattering parameters *ka***	**Wave steepness *H/L***
WC1	0.1-1.0	0.04
WC2	0.1-1.0	0.05
WC3	0.1-1.0	0.064

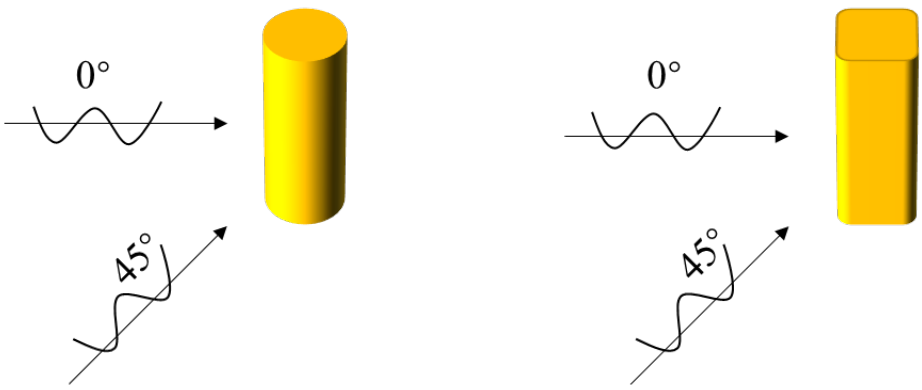

(a)

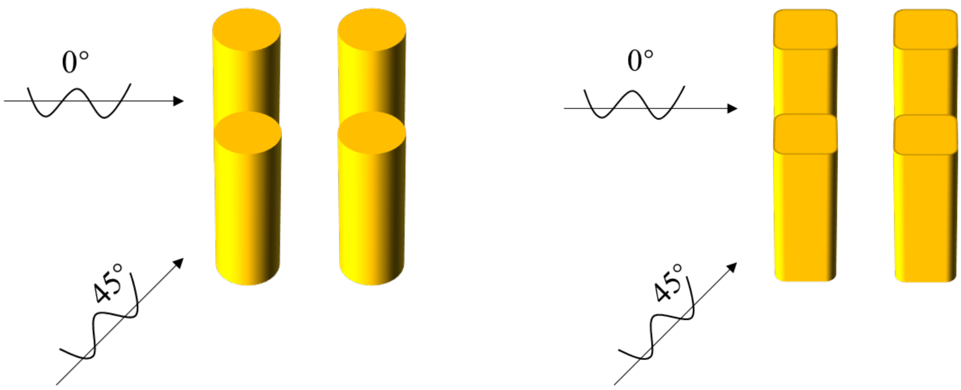

(b)

Figure 3.1 (a): Configuration of single column; (b): 4 columns with 0° and 45° incident wave

3.1.2 Mesh convergence of panel model and free surface model

A mesh sensitivity study has been carried out with different levels of mesh resolution for the simulation. The non-dimensional parameters of structure and incident wave in the sensitivity study have been kept the same. The scattering parameter is set to ka = 1.0, wave steepness is set to H/L=0.064 and leg space is $2D$ for 4 columns configuration, which is the strongest nonlinear condition in all the following simulations. Both surface elevation and the inline force have been calculated in the mesh sensitivity study. The leg space represents the distance between the centres of the columns for multiple cylinders group. Discretisation is carried out on both the column surface and the free surface as required by the second-order analysis. The mesh options have been listed in Table 3.3 and Table 3.4 for the single cylinder and the 4 cylinders cases respectively.

Table 3.3 Mesh options for the single cylinder and the second-order free surface

No.	Column surface mesh	No.	Free surface mesh
C1	400	F1	3000
C2	1500	F2	4000
C3	2400	F3	4800
C4	4800	F4	7650
C5	9600	F5	9000

In Table 3.3, there are 5 options for both column surface mesh and the free surface mesh. To avoid the influence between the two kinds of mesh, when investigating the mesh for the column, the mesh for the free surface has been set constant.

Table 3.4 Mesh options for the 4 columns configuration and the second-order free surface mesh

No.	Column surface mesh (1/4)	No.	Free surface mesh (1/4)
C1	400	F1	2700
C2	1500	F2	3920
C3	2400	F3	5070
C4	4800	F4	7800
C5	9600	F5	9250

Similar kinds of mesh for 4 cylinders configuration are listed in Table 3.4. Since the symmetrical configuration, only one-quarter of the mesh number is presented in Table 3.4. The method of convergence study is the same as the single cylinder case. The surface elevation and non-dimensional inline force calculated using different meshes are plotted in Figure 3.2 and Figure 3.3 respectively, and a clear trend of convergence for both physical quantities are evident. With the consideration of the two kinds of mesh and the computational time, the mesh of C4F4 (4800x7650) and C4F5 (4800x9250) are selected for the simulation of the single cylinder case and the 4 cylinders case respectively.

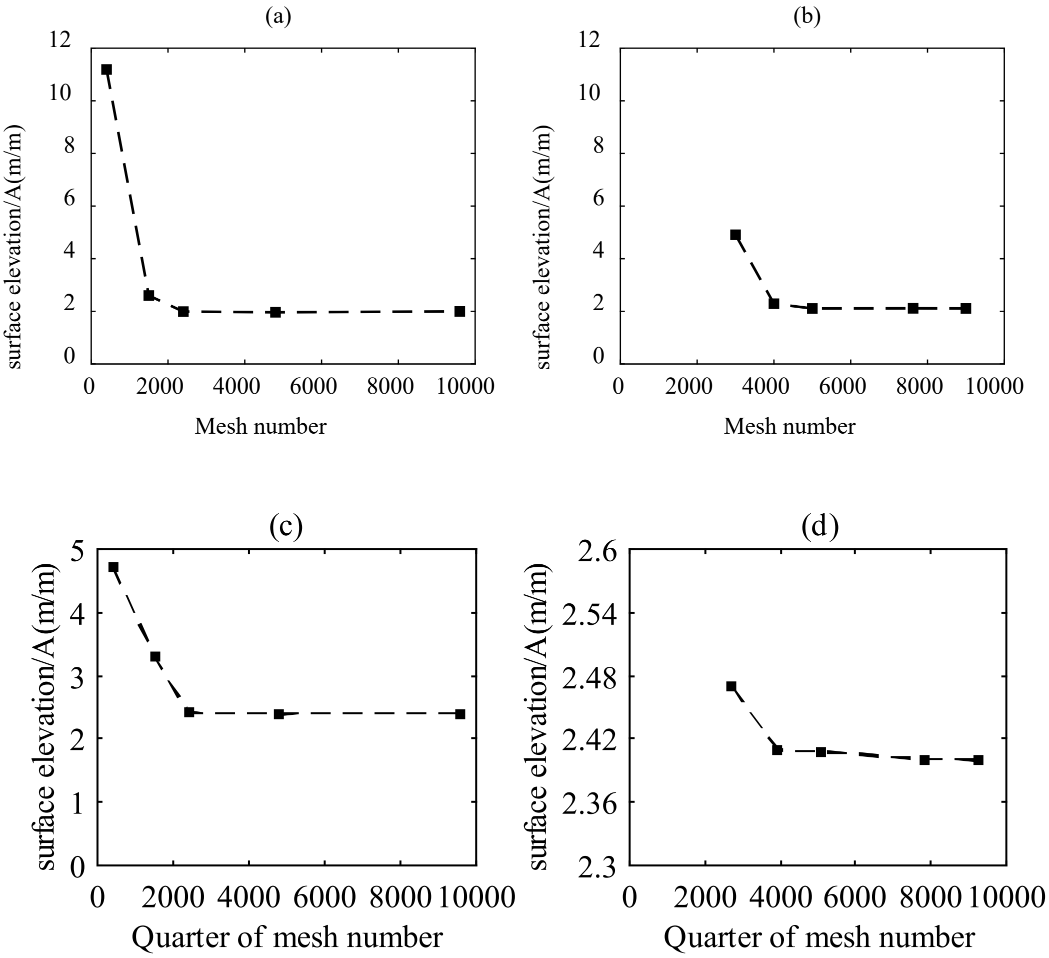

Figure 3.2 Surface elevation. (a): Column surface mesh convergence for the single fixed column with free surface mesh F5, (b): Free surface mesh convergence for the single fixed column with column surface mesh C5. (c): Column surface mesh convergence for the 4 fixed columns with free surface mesh F5 (d): Free surface mesh convergence for the 4 fixed columns with column surface mesh C5.

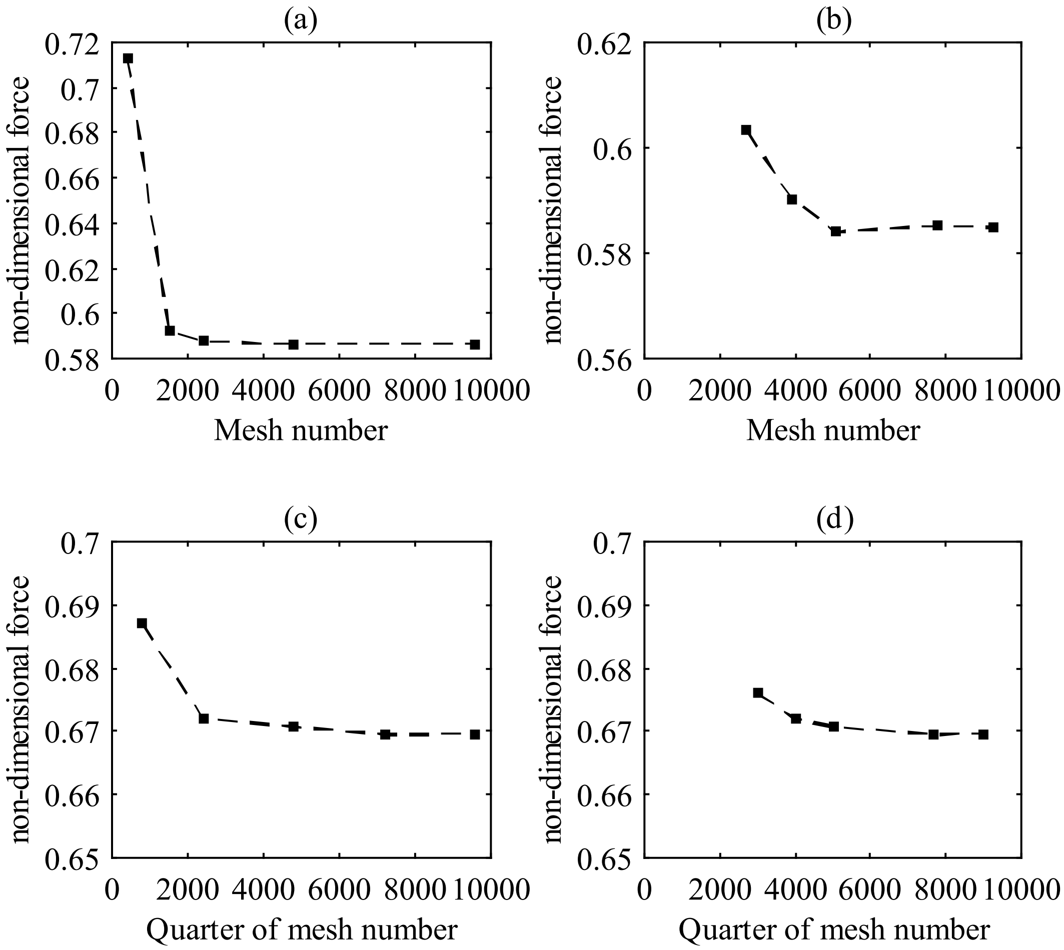

Figure 3.3 Inline wave force. (a): Column surface mesh convergence for the single fixed column with free surface mesh F5, (b): Free surface mesh convergence for the single fixed column with column surface mesh C5. (c): Column surface mesh convergence for the 4 fixed columns with free surface mesh F5 (d): Free surface mesh convergence for the 4 fixed columns with cylinder surface mesh C5.

The inline force shown in Figure 3.3 is non-dimensionalised by $\rho gHDd[\tanh(kd)/kd]$, where '*H*' is the incident wave height, '*D*' is the diameter of the cylinders, '*d*' is the water depth, and '*k*' is the wave number. As can be seen in Figure 3.2 and Figure 3.3, while simulations using the different mesh on the column approach to the converged results quickly for finer mesh, the requirement for the free surface mesh is considerably higher for the second-order free surface modelling.

(a) (b)

Figure 3.4 Visualization of the panel mesh of column (a) circular column; (b) Rounded corner square column

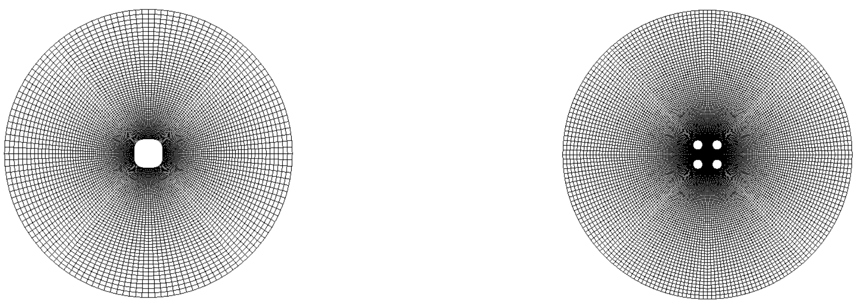

(a) (b)

Figure 3.5 Visualization of free surface mesh around the column (a) Free surface mesh for one column structure; (b) Free surface mesh for four columns

The panel mesh model and the free surface mesh adopted in the numerical simulation for surface elevation calculation are shown in Figure 3.4 and Figure 3.5 respectively.

3.2 Wave run-up along the column with different cross-section

3.2.1 Effect of cross-sectional shape of single column on wave run-up

There are different kinds of cross-section of column shape often be applied in the offshore structure design. Considerable research effort has been made about the impact of the shape of cross-section on wave run-up amplitude along column (Grice et al., 2013, Lu et al., 2020). However, there are very few studies focusing on the impact of the rounded corner ratio of squared column on the run-up amplitude along the vertical column. Three types of cross-sectional shapes for the columns are considered in the present work, i.e., circular, rounded corner square (with 3 different ratios, 1/6, 1/4 and 1/3) and the sharp corner square, to investigate the relationship between the surface elevation and the corner radius of column. Each column shape has the same cross-sectional diameter to keep the same diffraction parameters of the column.

The validation of wave run-up amplitude around the single column is presented firstly in Figure 3.6, and the run-up amplitude of the present numerical results agree well with the experimental measurements of Morris-Thomas and Thiagarajan (2004) for both scattering parameters calculated, ka=0.417 and ka=0.698 respectively. The maximum total amplitude η, which can be expressed as:

$$\eta = MAX\ Re\{\eta^{(1)}e^{-i\omega t} + \eta^{(2)}e^{-i2\omega t} + \bar{\eta}\} \tag{3.1}$$

where $\eta^{(1)}$, $\eta^{(2)}$ and $\bar{\eta}$ are time-independent surface elevation which is discussed in Section 2.6 and 2.7.

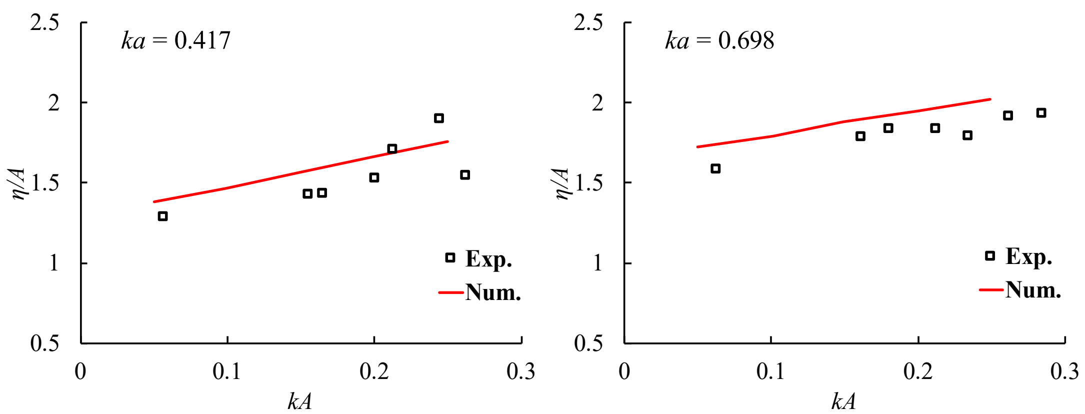

Figure 3.6 Wave run-up on a single column: Numerical results vs. Experimental measurements.

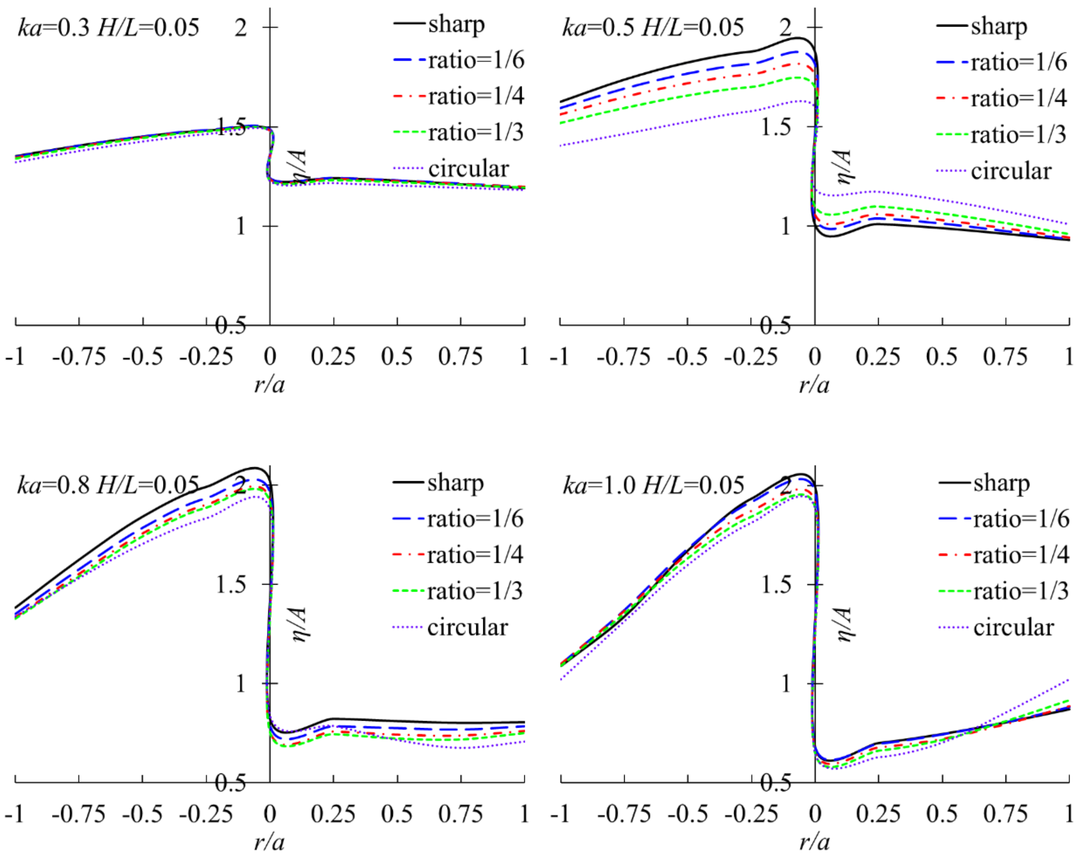

Figure 3.7 The wave profile near the column under 0° incident wave with different corner ratio columns

As one of the primary parameters crucial to the nonlinear wave interaction with offshore structures, scatter parameter can have significant impact on the nonlinear wave run-up and subsequent wave loads on offshore structures. The wave profile near single column in the incident wave direction at different scatter parameters *ka*=0.3, 0.5, 0.8 and 1.0 are calculated and shown in Figure 3.7 with the incident wave from 0° with the wave steepness *H/L*=0.05 (*H* is the wave hight and *L* is the wavelength). The wave profile before reaching the column is shown in the negative of the *X*-axis and profile behind the column is shown in the positive. The sharp corner square column and the circular column can be treated as special cases with corner ratio = 0 and 1/2 respectively. There is very slight difference of the wave run-up caused by columns of different corner ratios when *ka* = 0.3 because the wavelength is much longer than the diameter of the column. With higher scatter parameter like *ka* = 0.5, 0.8 and 1.0, there is more obvious impact of corner ratio on the wave run-up amplitude because of the shorter wavelength comparing to the column diameter. The higher corner ratio of the column evidently leads to lower wave run-up amplitude both upstream and downstream of the column when *ka* = 0.5, 0.8 and 1.0. However, there is an exception of the downstream for *ka* = 0.5 where a reverse trend can be observed for the wave run-up caused by different corner ratio of column indicating that the impact of the corner ratio on wave run-up is not uniform with the crossing scatter parameter.

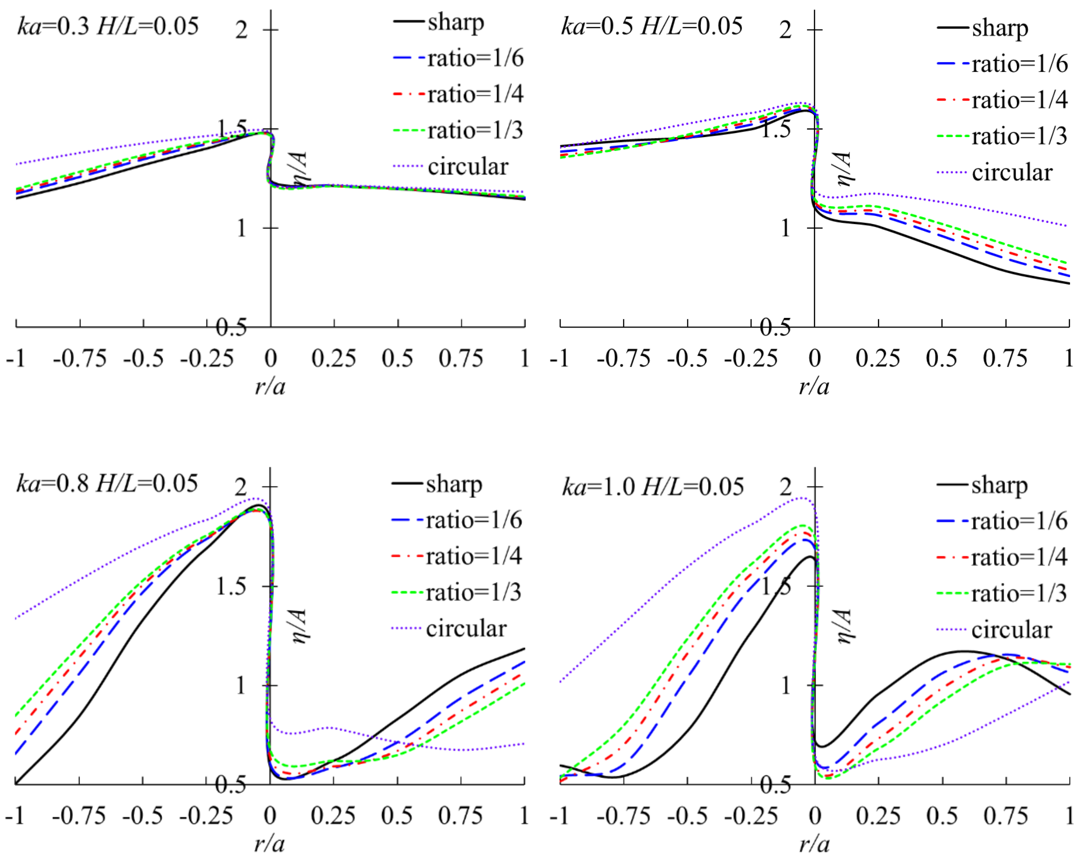

Figure 3.8 The wave profile near the column under 45° incident wave with different corner ratio columns

The wave profile near columns is shown in Figure 3.8 for the 45° incident wave. A general trend can be observed that in all cases, high corner ratio tends to lead to higher wave run-up upstream while result in lower wave run-up downstream noting that very little impact on wave run-up for *ka* = 0.3 where the diameter of the column is very small comparing to the incident wavelength. For all cases presented with different scatter parameters, the wave run-up is more sensitive to corner ratio with higher scatter parameter. At low *ka* (0.3 and 0.5), the surface profile appears to increase approaching the column and decrease downstream modestly, while for high *ka* (0.8 and 1.0), the free surface shows sharp increase approaching the column followed by clear increasing trend leaving the column downstream. Figure 3.8 demonstrates that the corner ratio has significant impact on nonlinear wave run-up especially for high scatter parameter conditions and thus should be considered in air-gap design for offshore structures.

3.3 Near-trapping and wave superposition around multiple columns

3.3.1 Near-trapping phenomenon in four columns structure

Four-columns structures are widely used in the offshore engineering. The interaction between columns and wave can lead to complex diffraction pattern around multiple columns. Near-trapping phenomenon are near-resonant free surface responses which is excited by waves of the appropriate frequency interacting with structures (Linton and Evans, 1990). There are considerable research effort on the near-trapping mode among multiple columns (Kim, 1972, Evans and Porter, 1997, Dong and Zhan, 2009, Grice et al., 2013, Kagemoto et al., 2014), and most studies are based on the circular columns due to their geometric simplicity (Evans and Porter, 1997, Dong and Zhan, 2009, Kagemoto et al., 2014). There are few works on the near-trapping among the square columns or rounded-corner square columns. As a key part of the present study, comprehensive numerical simulation has been conducted to further examine the phenomenon especially the detailed first- and second-order contributions of both surface elevation and wave forces on multiple column structures with variety of cross-sectional shapes, as well as under different incident wave directions. The numerical model with free surface mesh is firstly validated using the free surface elevation before the downstream column against experimental measurements of Contento et al. (2004) as shown in Figure 3.9.

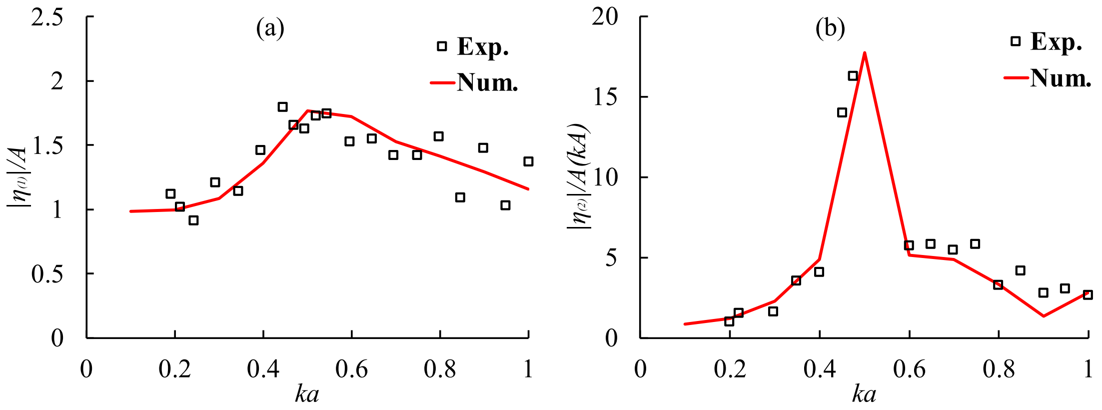

Figure 3.9 First-order (a) and second-order (b) non-dimensional amplitudes of the free surface elevation. Numerical result vs. Experimental result (Contento et al., 2004)

The first-order and the second-order surface elevation components are shown in Figure 3.9 (a) and (b) respectively. The surface elevation monitor point is selected just before the downstream column since this is the peak surface elevation point due to near-trapping phenomenon according to Linton and Evans (1990). In both numerical model and the experiment model, the geometric parameter is set a/d=0.275 (a is the radius of the column and d is the distance between the centres of two columns). The incident wave is from 45° to excite the four-column structure with potential near-trapping phenomenon and wave steepness is H/L =0.04. Figure 3.9 shows a good agreement between the numerical prediction and experimental measurement. According to Malenica et al. (1999), second-order near-trapping occurs at ka=0.5 which represents the half frequency of the linear trapping frequency resulting in the peak of the second-order component as shown in Figure 3.9 (b). It indicates that the potential theory model employed in the present study can predict the second-order near-trapping in multiple columns.

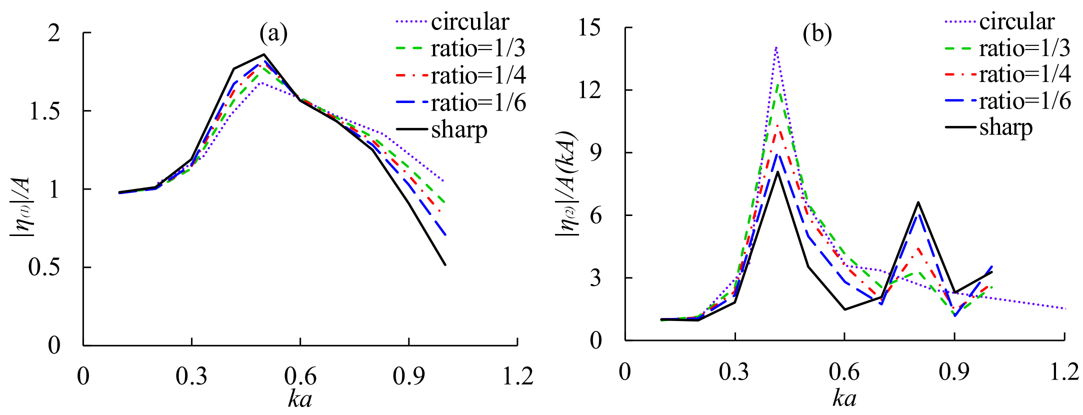

Figure 3.10 First-order (a) and second-order (b) non-dimensional amplitudes of the free surface elevation at point#1 (5.65, 0)

Similarly, for rounded-corner square columns, the surface elevation components at the Point#1 (-5.65, 0) before the downstream rounded-corner squared columns are presented in Figure 3.10 to investigate whether the near-trapping mode observed for circular columns are still valid for round square columns. The surface elevation around square and rounded-corner square columns are calculated along the increasing scatter parameter as shown in Figure 3.10. The ratio of the column's radius "*a*" to the distance between column axis "*d*" is set to $a/d = 0.25$ which is same to that in Malenica et al. (1999) for circular columns. The first-order surface elevation component (Figure 3.10 (a)) around different kinds of columns shows similar trend with increasing scatter parameter. The maximum first-order surface elevation amplitude increases as the corner ratio changes from circular to sharp. As described by Linton and Evans (1990) and Malenica et al. (1999), the second-order trapping frequency is $ka = 0.417$ for four circular cylinders with two times of diameter distance from centre to centre. It is shown that the second-order near-trapping occurs at $ka = 0.417$, thus forming the peak of the second-order surface component in front of the downstream cylinder shown in Figure 3.10 (b). There is an obvious difference between the second-order component surface elevation excited by the columns with rounded-corner and the circular column, that is, the second-order surface elevation component caused by the square and rounded corner square column has two distinct peaks ($ka = 0.417$ and $ka = 0.8$), while the circular cylinder only causes one peak ($ka = 0.417$).

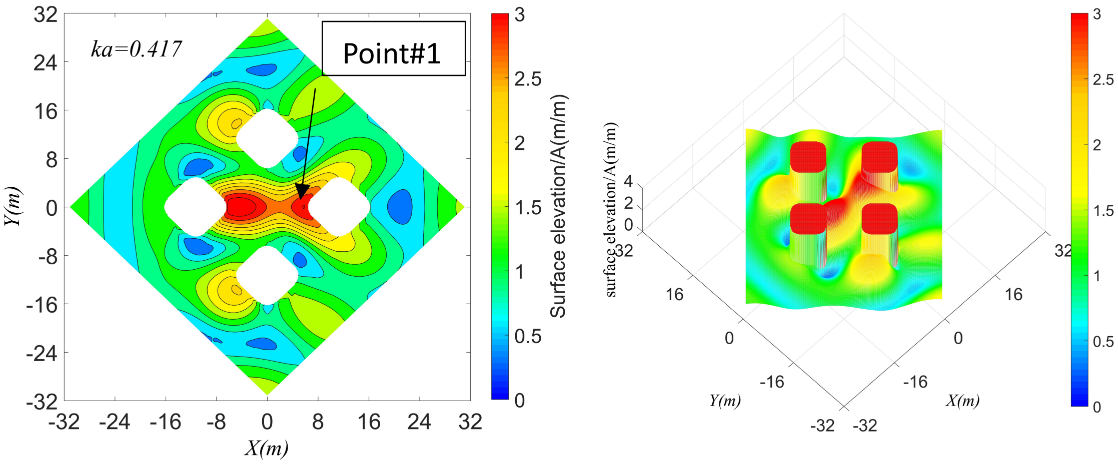
ka=0.417
Point#1
X(m)
Y(m)
Surface elevation/A(m/m)
surface elevation/A(m/m)

(a)

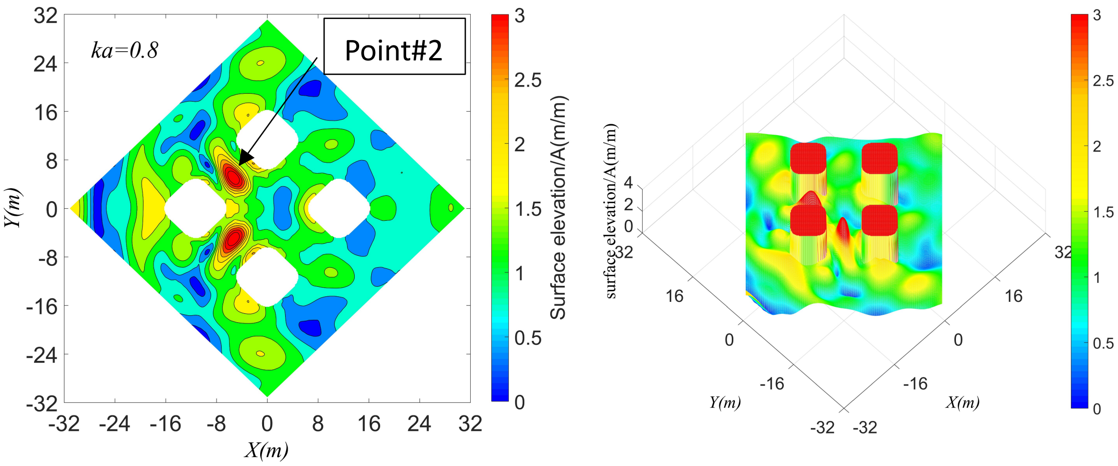
ka=0.8
Point#2
X(m)
Y(m)
Surface elevation/A(m/m)
surface elevation/A(m/m)

(b)

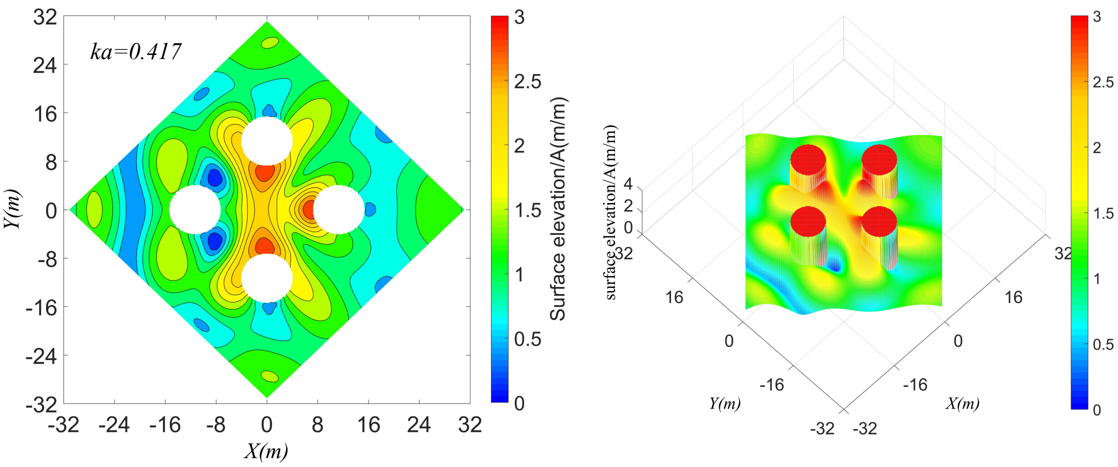
ka=0.417
X(m)
Y(m)
Surface elevation/A(m/m)
surface elevation/A(m/m)

(c)

Figure 3.11 Surface elevation contour around columns with 45° incident wave (a) rounded-corner square columns (ratio = 1/6) at *ka* = 0.417; (b) rounded-corner square columns (ratio = 1/6) at *ka* = 0.8; (c) circular columns at *ka* = 0.417 and points for surface elevation components analysis Point#1 (5.65, 0) and Point#2 (-5.65, 5.65)

To determine whether the two peaks of the second-order surface elevation component in Figure 3.10 are resulted from near-trapping among rounded-corner square columns, the contours of maximum surface elevation around the column group are plotted in Figure 3.11 (a) and (b) for *ka* = 0.417 and *ka* = 0.8 respectively. At the same time, the contour of wave surface elevation around the four circular columns with near-trapping phenomenon at *ka* = 0.417 is plotted in Figure 3.11 (c) for comparison. As shown in Figure 3.11, for *ka* = 0.417 (Figure 3.11 (a)), the peak surface elevation is located in the area surrounded by four rounded-corner square columns, which is similar to the surface elevation around the circular columns in Figure 3.11 (c). However, for *ka* = 0.8 (Figure 3.11 (b)), there is no clear peak of surface elevation in the same region surrounded by the rounded corner square columns as observed for *ka* = 0.417. On the contrary, a pair of peak surface elevations appear in the space between upstream and middle stream columns. The peak value of the second-order component at *ka*=0.8 is increasing with the lower corner ratio (second-order components of sharp corner column is highest at *ka*=0.8). This is inconsistent with the characteristics of peak surface elevation caused by near-trapping that the peak value of the second-order components caused by near-trapping will reduce with the decreasing corner ratio. It indicates that the peak of the second-order surface elevation component in front of the downstream column at *ka* = 0.8 is independent of the near-trapping and is attributed the superposition of the second-order components of the diffraction by different columns.

The surface elevation amplitude at the Point#1 along the time series at *ka*=0.417 and wave steepness *H/L*=0.064 is shown in Figure 3.12 to make near-trapping before different corner ratios' downstream columns more comprehensive. There are two peaks of surface elevation in each wave cycle in time series. The larger ratio columns make the peaks become higher and the troughs become lower. It indicates that the reduction of the second-order surface elevation component by decreasing corner ratios shown in Figure 3.10 (b) made the total surface elevation reduce when near-trapping occurs. A series of 3D surface elevation contour from 0s to 5.5s (with 0.5s each step) is also plotted in Figure 3.13 to show the surface elevation around four columns with corner ratio=1/6.

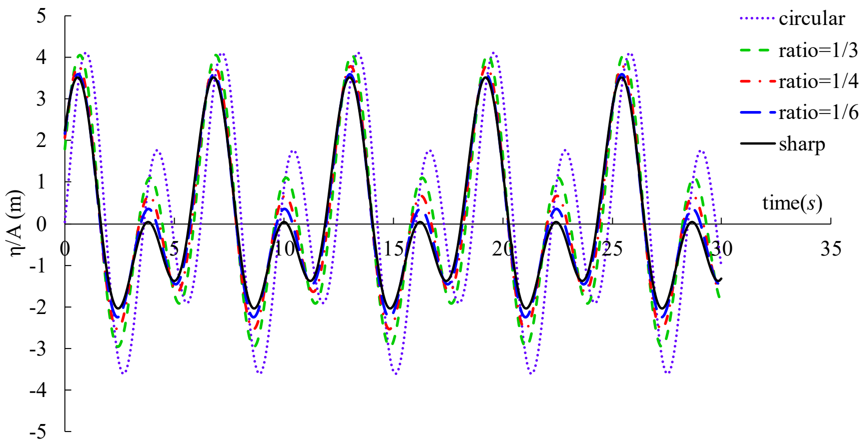

Figure 3.12 The surface elevation at Point#1 in time series (*ka*=0.417; *H/L*=0.064)

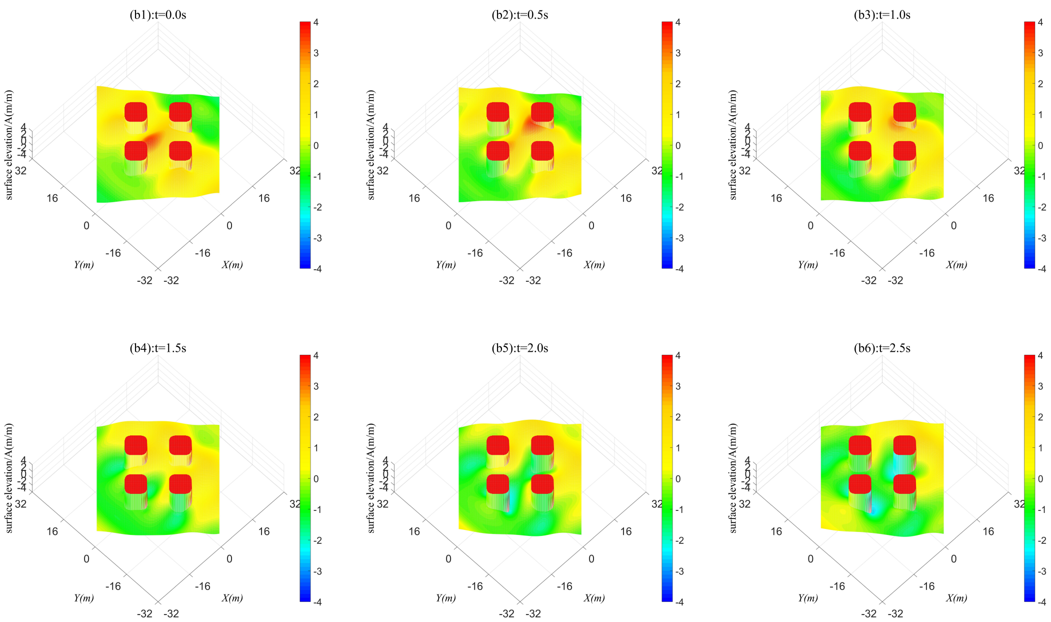

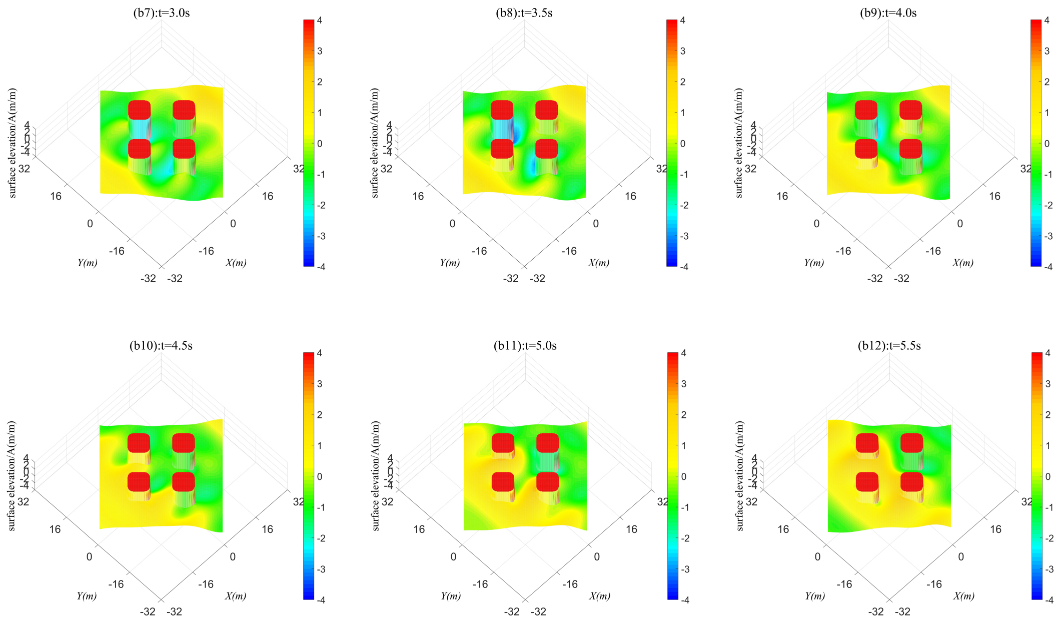

Figure 3.13 A time series surface elevation (nondimensionalized by the incident wave amplitude A) at the Point#1 and surface elevation contour around columns (ratio=1/6) with ka=0.417 and H/L=0.064

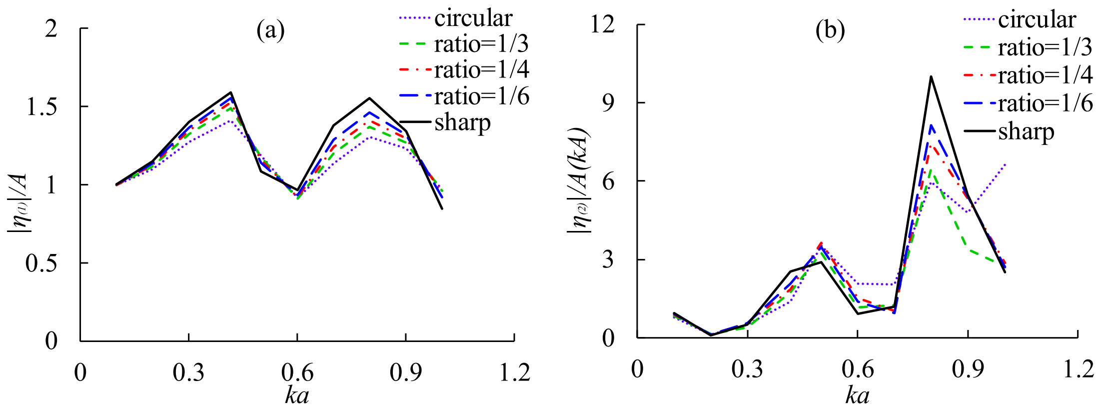

Figure 3.14 First-order (a) and second-order (b) non-dimensional amplitudes of the free surface elevation at point #2 (-5.65, 5.65)

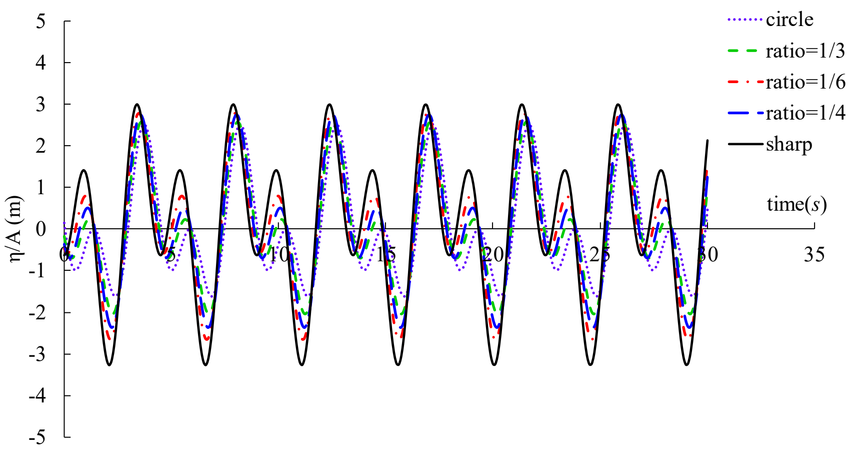

Figure 3.15 The surface elevation at Point#2 in time series (*ka*=0.8; *H/L*=0.064)

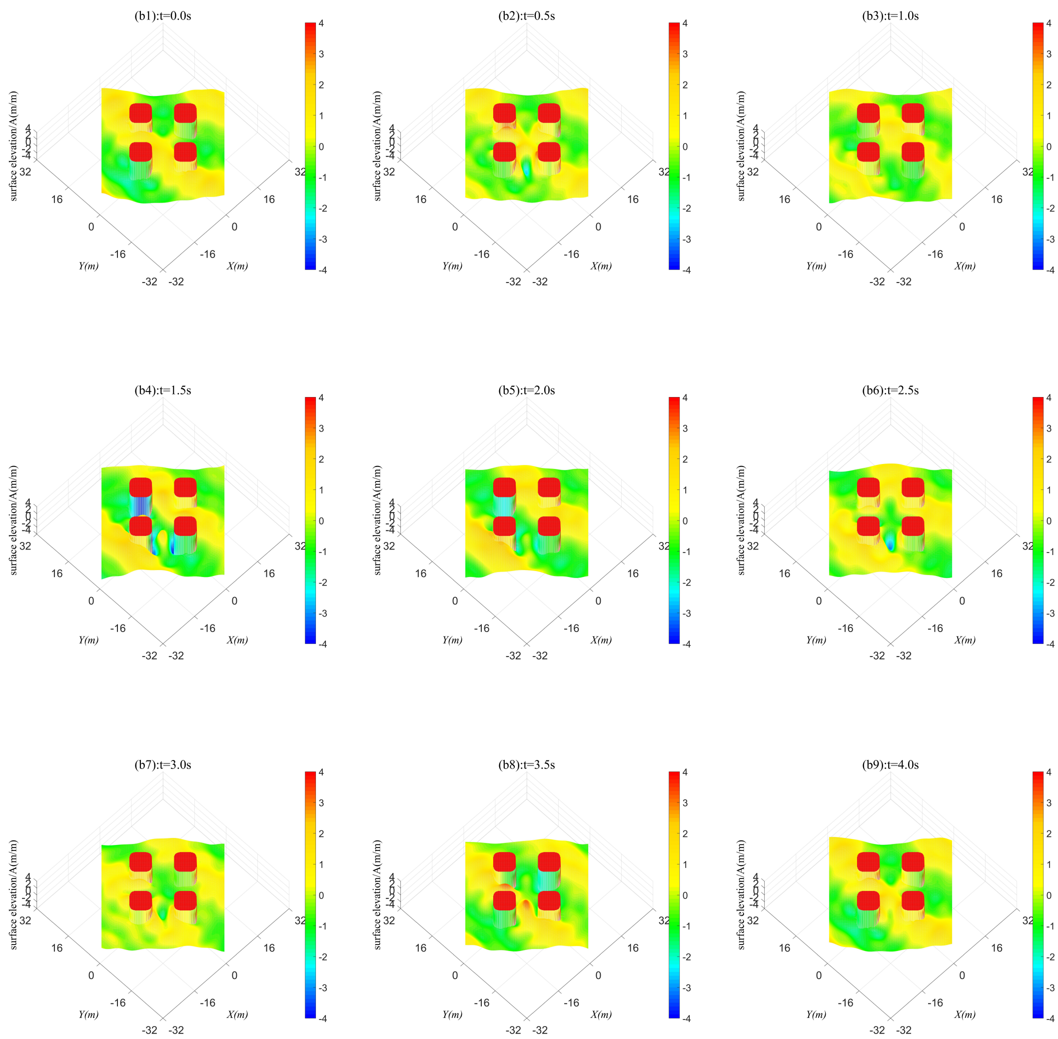

Figure 3.16 A time series surface elevation (nondimensionalized by the incident wave amplitude *A*) at the Point#2 and surface elevation contour around columns (ratio=1/6) with

ka=0.8 and H/L=0.064

In Figure 3.11 (b), it can be easily seen that there is an obvious peak between the upstream column and middle stream column. The analysis of the surface elevation components at the Point#2 (-5.65, 5.65) which is between these columns is carried out and the results are compared with the surface elevation components excited by circular columns in Figure 3.14. There are two similar peaks at ka=0.417 and ka=0.8 in first-order surface elevation component as shown in Figure 3.14 (a). However, there is no obvious peak at Point#2 (-5.65, 5.65) shown in contour of surface elevation at ka = 0.417 in Figure 3.11 (a). It indicates that the first-order elevation component of the peaks appearing insufficient to lead to the total peak surface elevation. In other words, the contribution of peak surface elevation seen at ka = 0.8 is the second-order surface elevation component. It is shown that the rounded-corner square column leads to the peak of the second-order surface elevation component (Figure 3.14). The sharp corner columns lead to the highest second-order surface elevation component. The peak value of the second-order surface elevation component decreases with the increasing corner ratio. It is noted that the flat part of the square columns makes the wave reflection between columns much stronger than circular columns. This should be taken into consideration in the design of the offshore structures with square columns.

In the time series of surface elevation at Point#2 shown in Figure 3.15 and Figure 3.16, there are two peaks in each wave cycle which is same with that at Point#1. According to the surface elevation in time series in Figure 3.15, there are two peaks appearing at Point#2 at t=1.5s and 3.5s respectively which is also shown in the 3D surface elevation (Figure 3.16) at Point#2. However, the highest peak and lowest trough of the surface elevation at Point#2 are caused by the column with sharp corners. It indicates that the oscillating amplitude of the surface elevation at Point#2 is reducing with increasing columns' corner ratio (from sharp corner to circle).

3.3.2 Surface elevation in the multiple columns under different wave directions

The flat panel parts of square columns can lead to exacerbated wave reflection between two adjacent columns. Therefore, the contour of the surface elevation around the square columns and the detailed surface elevation components are further analysed. In addition to that the surface elevation between adjacent columns in 45° incident wave discussed in previous section, the surface elevation around the multiple columns under 0° incident wave is examined in this section.

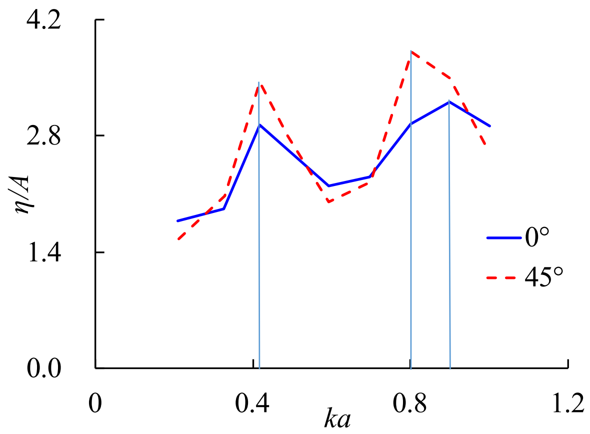

Figure 3.17 Maximum surface elevation around four fixed rounded-corner square columns (ratio=1/6) with 2 times diameter leg space

The maximum surface elevation around four rounded-corner square is shown in Figure 3.17. It can be seen that there are two peaks for the 0° incident wave at *ka*=0.417 and *ka*=0.9 while two peaks at *ka*=0.417 and *ka*=0.8 are observed under 45° incident wave. The contours of surface elevation around the rounded-corner square columns (ratio=1/6) at *ka*=0.417 and *ka*=0.9 under 0° incident wave are plotted in Figure 3.18 (a) and (b). It is noted that a single peak surface elevation occurs at the centre of the area enclosed by the four rounded-corner square columns nearing the upstream columns at *ka*=0.417. In contrast, two distinct peaks of surface elevation can be clearly seen near the inner boundaries of the two upstream columns at *ka*=0.9. The centre of the geometry is selected as the Point#3 (0, 0) shown in Figure 3.18 (a) to investigate the source of the peak surface elevation for *ka*=0.417. Since the whole configuration is symmetrical, the point near the inner boundaries of one of the upstream columns is selected as the Point#4 (-8, 4) shown in Figure 3.18 (b) to investigate the source of the peak surface elevation peak for *ka*=0.9.

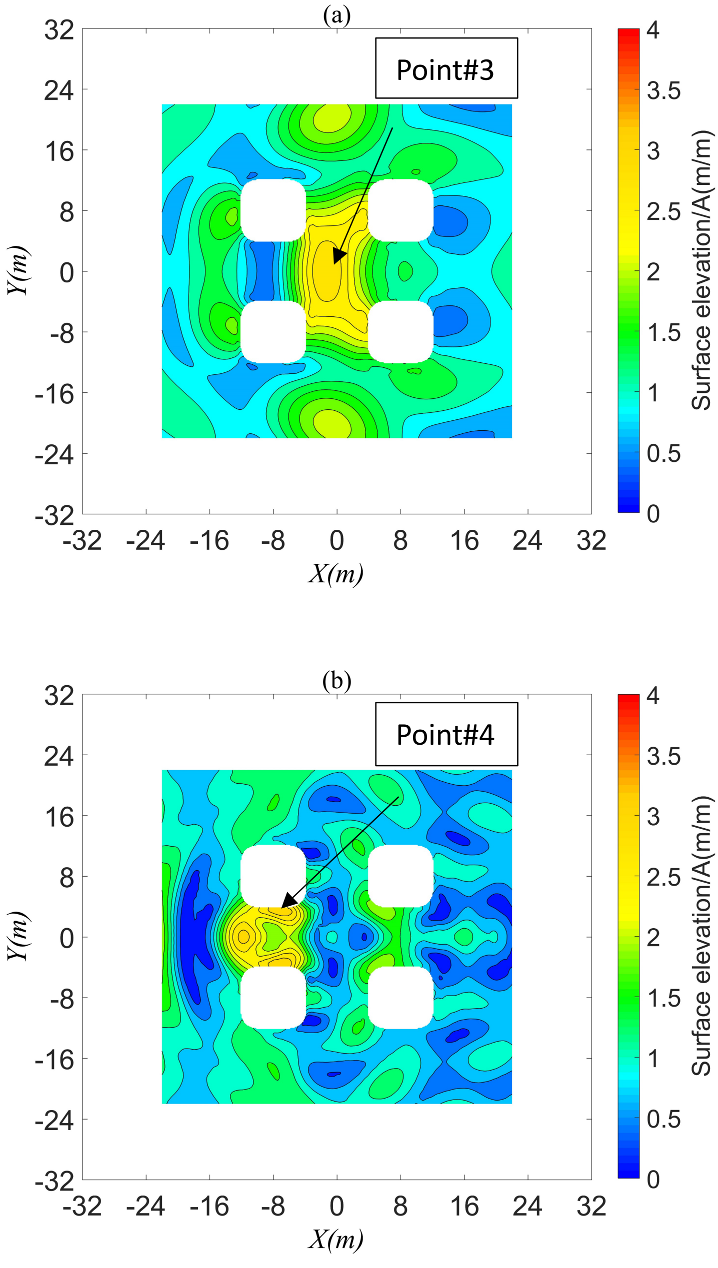

Figure 3.18 Contour of surface elevation near rounded-corner square columns (ratio = 1/6) with 0° incident wave (a) *ka* = 0.417; (b) *ka* = 0.9 and points for surface elevation components analysis point#3 (0, 0) and point#4 (-8, 4)

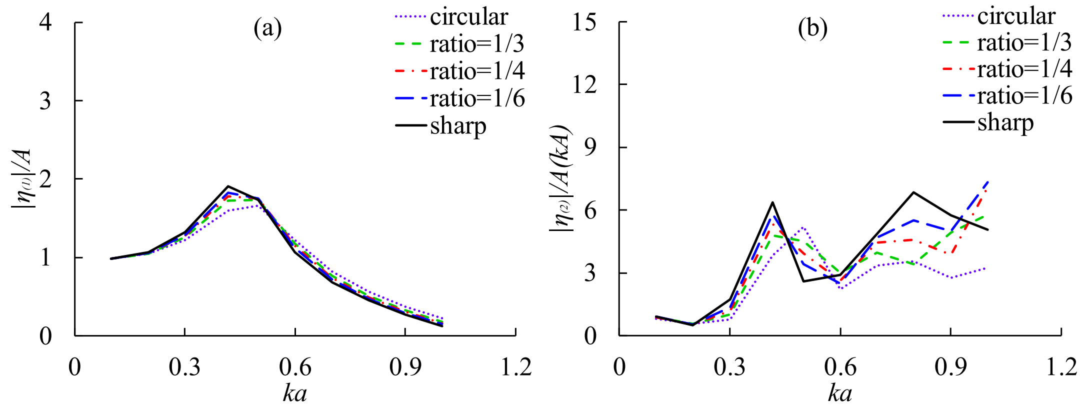

Figure 3.19 First-order (a) and second-order (b) non-dimensional amplitudes of the free surface elevation at geometric centre point #3 (0, 0) in Figure 3.18

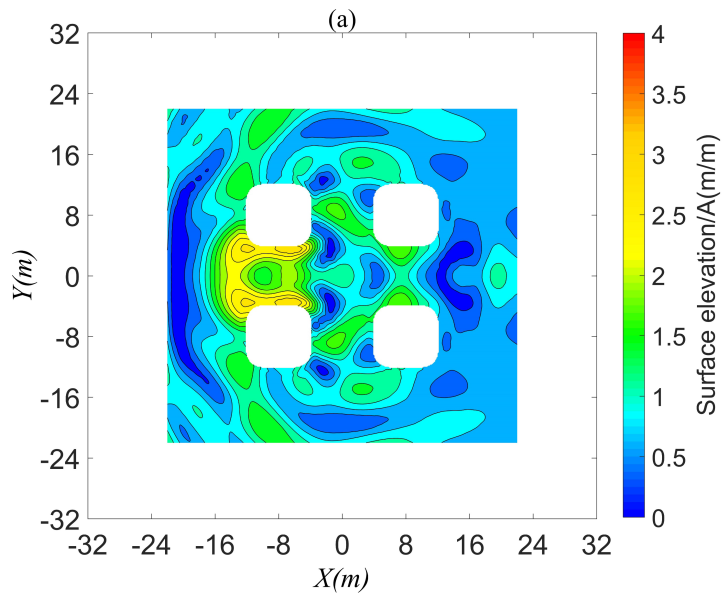

Figure 3.20 Contour of surface elevation near rounded-corner square columns (ratio = 1/6) with 0° incident wave at ka = 0.8

The first-order and second-order surface elevation components at geometric centre Point (0, 0) are shown in the Figure 3.19 (a) and (b) respectively. There is one peak of first-order surface elevation at ka = 0.417 shown in Figure 3.19 (a) while two peaks of the second-order surface elevation are clearly observed at ka = 0.417 and ka = 0.8 respectively as shown in Figure 3.19 (b). There is no peak surface elevation at geometric centre point at ka = 0.8 as shown in Figure 3.20 indicating that the peak of the second-order component shown in Figure 3.19 (b) has little contribution to the total surface elevation amplitude. It indicates that the peak of surface elevation at ka = 0.417 is dominated by the first-order surface elevation component. It can be further demonstrated by the ratio between the second-order and the first-order surface elevation at the geometric centre point which equals 3/5 when ka = 0.417. The first-order surface elevation component increases gradually with ka until reaching its peak at ka = 0.417 rather than a sudden jump, which means that the peak of the first-order surface elevation is not caused by resonance phenomenon between columns. It indicates that the peak at the geometric centre point is primarily due to the superposition of the incident waves and diffracted waves inside the four columns.

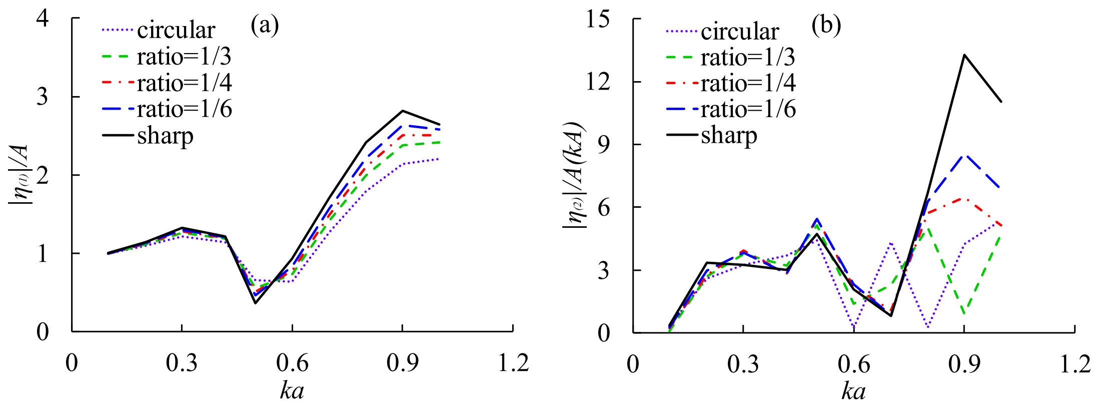

Figure 3.21 First-order (a) and second-order (b) non-dimensional amplitudes of the free surface elevation at point #4 (-8, 4) in Figure 3.18

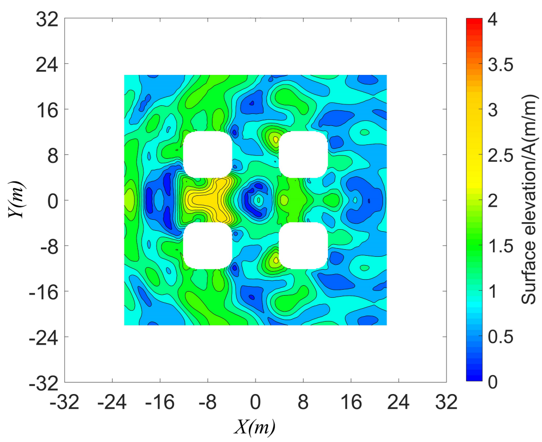

Figure 3.22 Contour of surface elevation near rounded-corner square columns (ratio = 1/6) with 0° incident wave at ka = 1.0;

In Figure 3.21, the surface elevation components at the point near the upstream columns (Point #4) are analysed in the first-order (Figure 3.21 (a)) and the second-order (Figure 3.21 (b)). For rounded-corner ratio 1/6, the highest first-order surface elevation component occurs at ka=0.9 in Figure 3.21 (a). There is also a significant peak of the second-order surface elevation component at ka = 0.9 as shown in Figure 3.21 (b). It is noted that the first-order surface component at the Point#4 changes little from ka = 0.9 to ka = 1.0. However, there is a marked reduction of second-order surface elevation component with increasing ka from 0.9 to 1.0 shown in Figure 3.21 (b). The different trend of the first- and the second-order surface elevation components at Point#4 is examined to further investigate the source of the peak surface elevation at ka = 0.9. The contour of the surface elevation around rounded-corner square columns at ka = 1.0 is also plotted in Figure 3.22 as comparison since different contribution of the first-order and the second-order surface elevation components from ka = 0.9 to 1.0. In Figure 3.22, the peak of total surface elevation occurs in the centre of the upstream columns rather than the position near columns. Comparing the surface elevation contour at ka = 0.9 (Figure 3.18 (b)) and ka = 1.0 (Figure 3.22), it is clear seen that the surface elevation amplitude at the point#4 decrease significantly with increasing ka = 0.9 to ka = 1.0.

It indicates that the first-order component does not have a decisive influence on the peak of surface elevation at the point#4, but the second-order component causes the peak at ka = 0.9. Since the second-order component peak appears gradually climbing (not generated in a narrow frequency band) instead of sudden jump, the peak of second-order surface component is the consequence of superposition of waves. In addition, the peak second-order surface component tends to decrease with higher ratio of corner of column. The impact of the ratio on the second-order component is more pronounced than that on the first-order component. Due to the lower ratio of corner radius, there is larger parallel part of columns leading stronger reflection of waves, and further resulting in the higher surface elevation and stronger nonlinearity.

3.4 Summary

In the present work, the potential theory-based program is used to solve the diffraction potential and surface elevation around the multiple columns where the incident wave is perturbed to the second-order. A number of physical parameters important to the surface elevation are examined in detail including the cross-section of the columns, ratio of the rounded corner of square columns and incident wave direction crossing multiple columns. It is noted that the highest surface may not only occur around the columns due to the interaction of multiple columns, thus the surface elevation analysed here is not only along the columns but also the entire area under the deck of the platform. A fully second-order solution of the surface elevation is obtained for wave diffraction problem.

The wave run-up along the columns and surface elevation around the multiple columns are investigated in present study. For the incident wave $Kc=A/a<\mathcal{O}(1)$ and wave steepness $H/L<0.14$, the potential theory is applied on the calculation of wave run-up along columns and surface elevation around the multiple columns. The wave run-up and peak surface elevation around rounded-corner square columns with different corner ratio are investigated and compared with those excited by circular columns. There are some conclusions achieved:

- The increasing ratio of corner radius appears to result in a lower wave run-up along the rounded-corner square column under 0° incident wave, and a higher wave run-up under 45° incident wave.

- There are two mechanism resources of the peak surface elevation namely superposition and near-trapping. Superposition is caused by the combination of incident wave and diffracted wave. Near-trapping is due to the resonance of the waves between columns which is dependent on the distance between columns and incident wavelength.

- It is demonstrated that near-trapping frequency model for multiple circular columns is still valid for the four rounded-corner square columns. However, the peak surface elevation due to near-trapping reduces with increasing corner ratio.

- The impact of the column’s corner ratio on the second-order component is significantly larger than that on first-order component. The peak of the second-order surface component decreases with higher ratio of column’s corner.

- During wave interaction with four rounded-corner square columns, a single peak surface elevation under 0° incident wave is attributed to superposition, while different peaks of surface elevation depending on scatting parameter under 45° incident wave are demonstrated due to near-trapping and superposition, respectively.

4 Dynamics of TLP-TAD multi-platform system

4.1 Model description of the multi-body system

As the offshore energy industry progressive moving towards harsh deepwater environment, larger and more complex platform system with more functions is required for longer operation time in offshore oil and gas industry. Multi-platform system is an excellent method to meet the requirements. A typical multi-platform system contains a production platform and a support platform (accommodation or drilling platform). The first commercial multi-platform system is consisting of a Tension Leg Platform (TLP) as production platform and a Tender Assist Drilling (TAD) as support platform. The dynamic characteristics of multi-platform system are investigated in the following section (Ren and Tao, 2017, Ren et al., 2019, Ren and Tao, 2021)

The specifications of TLP and TAD investigated in the present study are given in Table 4.1. A new coordinate system is introduced in this Chapter to define the fairleads and anchors positions of TLP and TAD. The global coordinate system *O-XYZ* is located at the mean water surface with OZ-axis pointing to upwards as described in Chapter 2. The new coordinate systems are located at the keel of TLP (O_T-$X_TY_TZ_T$) and TAD (O_D-$X_DY_DZ_D$) as shown in Figure 4.1. The XY plane is horizontal located at the base line of TLP and TAD. The Z-axis of these two new coordinates point to upwards. TLP is composed of four circular columns and rectangular pontoons. 8 tendons are attached to the columns (2 for each column) of the TLP. There are 24 top tension risers (TTRs) connecting with TLP in the real project. These 24 TTRs are simplified as 4 equivalent TTRs in model test and numerical simulation. 4 steel catenary risers (SCRs) are connected to the pontoon for production as shown in Figure 4.1. Two back lines applied to the TLP are to restrict its movement towards TAD. TAD is designed based on a semi-submersible with 8 mooring lines (Figure 4.1). Two platforms are connected by 4 hawsers. Detailed properties of the hawsers and mooring system for TLP (tendons, top tension risers and back lines) and TAD (8 mooring lines) are presented in this Section. The truncation method used in the experiment can be found in Wei et al. (2017) and Biao et al. (2018).

Table 4.1 Main particulars of TLP and TAD (full scale)

Parameter	Unit	TLP	TAD
Displacement	MT	5.09E4	1.73E4
Draft	m	22.25	9.75
XG	m	0.0	-0.1
KG	m	32	16.6
Roll gyradius	m	31.5	19.5
Pitch gyradius	m	30.2	31.2
Yaw gyradius	m	28.9	30.2
O_T/O_D in $O\text{-}XYZ$	m	(0,0, -22.25)	(109.04, 0, -9.75)

KG: from keel to centre of gravity

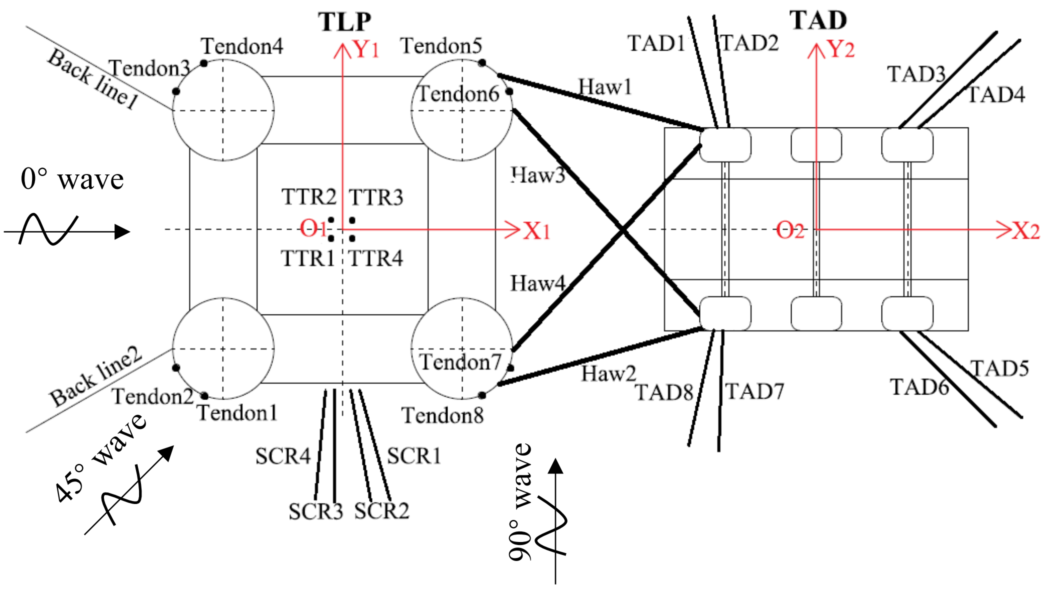

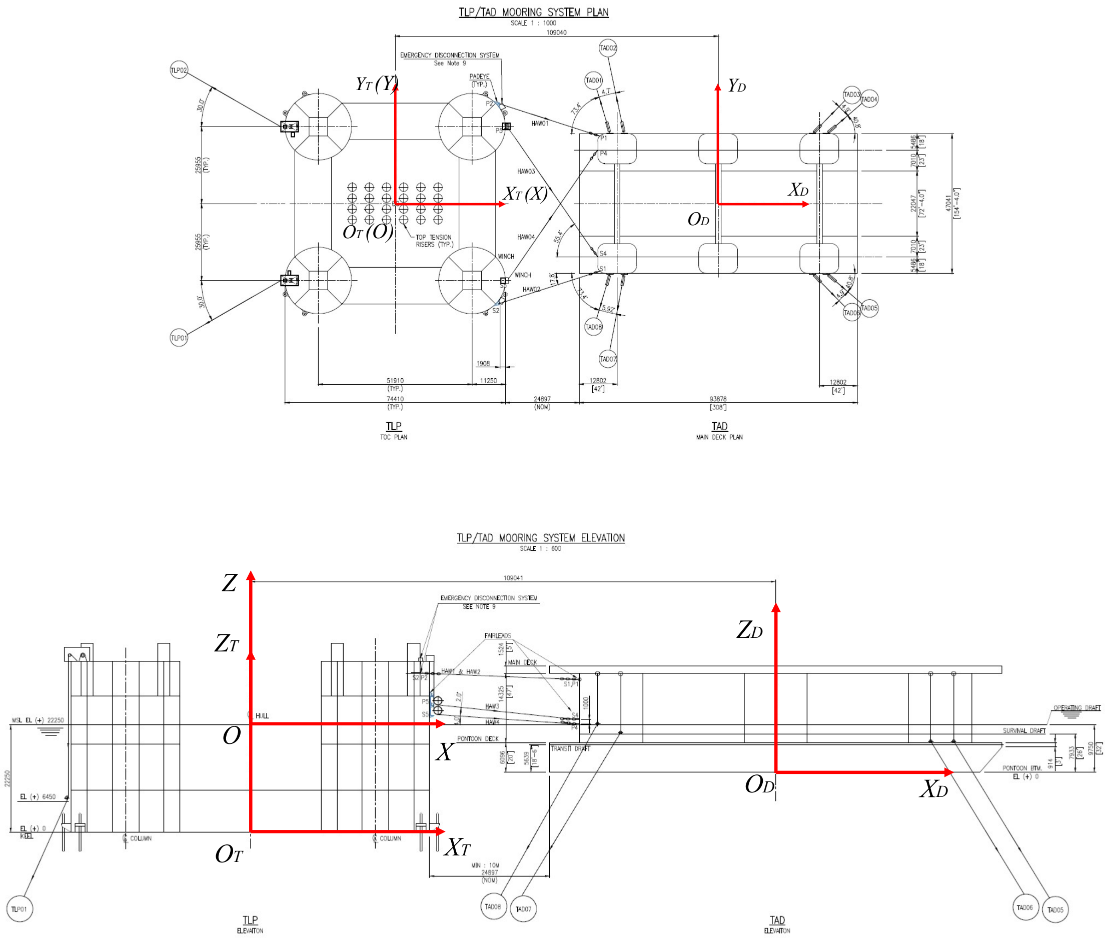

Figure 4.1 The arrangement of TLP and TAD in multi-body coupled model (Dong et al., 2019)

The fairleads and anchor points of 8 tendons are listed in Table 4.2 and properties of each tendon are provided in the Table 4.3.

Table 4.2 Tendons Geometry (in new TLP's coordinate system $O\text{-}X_TY_TZ_T$)

Tendon	Top position			Bottom position		
	X_T (m)	Y_T (m)	Z_T (m)	X_T (m)	Y_T (m)	Z_T (m)
T1	-30.833	-37.735	3.246	-30.833	-37.735	-463.75
T2	-37.735	-30.833	3.246	-37.735	-30.833	-463.75
T3	-37.735	30.833	3.246	-37.735	30.833	-463.75
T4	-30.833	37.735	3.246	-30.833	37.735	-463.75
T5	30.833	37.735	3.246	30.833	37.735	-463.75

T6	37.735	30.833	3.246	37.735	30.833	-463.75
T7	37.735	-30.833	3.246	37.735	-30.833	-463.75
T8	30.833	-37.735	3.246	30.833	-37.735	-463.75

Table 4.3 Tendon Properties, per tendon

Parameter	Unit	Prototype
Water depth	m	486.0
Tendon length	m	467.3
TLP draft	m	22.25
Tendon top from keel	m	3.246
Outside diameter	m	0.9144
Wall thickness	m	0.0343
EA/L	MT/m	4147.44
Weight in air	kg/m	832.7
Buoyancy	kg/m	673.1
Weight in water	kg/m	119.95
Top tension	MT	1450.0
Bottom tension	MT	1375.42

There are 4 equivalent top tensioned risers (TTRs) are applied for TLP to represent the 24 risers in prototype. The axial stiffness of the 4 risers is modeled to reproduce the total stiffness. The geometry of the 4 equivalent risers is given in Table 4.4 and main particulars are listed in Table 4.5.

Table 4.4 Top tension risers Geometry (in new TLP's coordinate $O\text{-}X_TY_TZ_T$)

Tendon	Top position			Bottom position		
	X_T (m)	Y_T (m)	Z_T (m)	X_T (m)	Y_T (m)	Z_T (m)
R1	8.69	3.66	40.50	8.69	3.66	-463.75

R2	8.69	-3.66	40.50	8.69	-3.66	-463.75
R3	-8.69	-3.66	40.50	-8.69	-3.66	-463.75
R4	-8.69	3.66	40.50	-8.69	3.66	-463.75

Table 4.5 Equivalent Risers Properties

Parameter	Unit	Prototype	Equivalent
Water depth	m	486.0	486.0
TLP draft	m	22.25	22.25
Top COR (centre of rotation) from keel	m	40.50	40.50
Riser length	m	504.00	504.00
Diameter	mm	365.00	894.00
EA/L	MT/m	19031.80	4757.90*4
Tensioner stiffness	MT/m	1366.14	341.53*4
Overall stiffness	MT/m	1274.64	318.66*4
Weight in air (total)	kg/m	5537.2	1384.3*4
Buoyancy (total)	kg/m	2483.3	620.8*4
Wet weight (total)	kg/m	3053.8	763.4*4
Top tension (total)	MT	2626.02	656.51*4

There are also 4 steel catenary risers are employed in the TLP model. The impact of the SCRs has been taken into consideration. The properties of the SCRs are provided in Table 4.6 and Table 4.7. The anchor positions are listed in Table 4.8.

Table 4.6 SCRs properties

No.	OD	OD +coating	Dry weight	Wet weight	EA
	mm	m	kg/m	kg/m	kN
8" Gas export flowline	219.1	0.2259	121.00	82.00	2.4842E+06

(SCR01)					
10" Liquid export flowline (SCR02)	282.5	0.3851	231.00	112.00	3.7579E+06
Future water injection (SCR03)	282.5	0.2893	204.00	140.00	4.2467E+06
Future water injection (SCR04)	282.5	0.2893	204.00	140.00	4.2467E+06

OD: outer diameter; E: Young's module; A: Crossing area.

Table 4.7 SCRs Layout (in new TLP's coordinate $O\text{-}X_TY_TZ_T$)

No.	Top tension	Departure angle	Azimuth angle	SCR Porch Coordinate X_T	Y_T	Z_T
	kN	deg	deg	m	m	m
8" Gas export flowline	572	18	110.31	8.050	-36.463	6.190
10" Liquid export flowline	782	18	104.64	3.450	-36.463	6.190
Future water injection	968	18	90.00	-3.400	-36.463	6.190
Future water injection	968	18	85.00	-8.000	-36.463	6.190

Table 4.8 SCR lengths and anchor locations (in global coordinate system $O\text{-}XYZ$)

No.	Length	Anchor Location X	Y	Z
	m	m	m	m
SCR01	1046.07	285.755	-786.716	-486
SCR02	1050.06	205.578	-810.507	-486
SCR03	1046.296	-3.400	-836.463	-486
SCR04	1046.29	-77.725	-833.419	-486

For TAD's mooring system, the configuration and the principal dimensions of the coupled mooring system are given in Figure 4.1 (b), (c) and Table 4.9.

Table 4.9 Mooring configuration of the TAD and back lines of the TLP

No.	SEG1 Wire	SEG2 Chain	Attach. Buoyancy	SEG3 Rope	SEG4 Chain	SEG5 Chain	Azimuth angle	Pre-tension	Hang-off Angle
	m	m	(MT)	m	m	m	deg	MT	deg
TAD01	168.00	30.00	-	894.00	162.00	21.00	73.40	74.11	29.03
TAD02	130.00	30.00	-	902.00	144.00	21.00	78.05	78.08	28.47
TAD03	422.00	30.00	-	853.00	223.00	21.00	134.31	80.70	27.83
TAD04	461.50	30.00	-	839.00	223.00	21.00	139.25	79.31	28.27
TAD05	350.00	30.00	-	956.00	238.00	21.00	220.75	79.82	29.46
TAD06	321.00	30.00	-	963.00	238.00	21.00	225.69	80.27	29.55
TAD07	135.00	46.00	18.00	841.00	137.00	21.00	280.71	76.15	24.46
TAD08	130.00	46.00	18.00	832.00	155.00	21.00	286.63	72.46	24.50
TLP01	165.00	30.48	-	1059.18	283.80	21.00	330.17	90.00	26.87
TLP02	161.00	30.48	-	1050.04	283.08	21.00	30.13	89.70	25.44

Note: Hang-off angle is measured with respect to the MWL (mean water level). Azimuth angle is measured clockwise from the TLP platform North (negative direction of OX or O_TX_T).

As shown in Table 4.9, there are three kinds of material employed in the mooring lines connecting to the TAD and the backlines connecting to TLP. The make-up of the mooring lines and their properties are listed in Table 4.10.

Table 4.10 TLP/TAD mooring and hawser makeup and properties

Material	Diameter	EA	Dry weight	Wet weight	MBL
	mm	kN	N/m	N/m	MT
Wire	79	3.531E+05	349.8	258.2	522
R4 chain	76	5.837E+05	1135.6	987.2	615
Rope	137	TBD	126.4	30.2	587

MBL: maximum breaking limitation

The position of fairleads and anchors for mooring lines on TAD and backlines on TLP are listed in the Table 4.11.

Table 4.11 Fairlead and anchor coordinates of the TLP/TAD (For TAD in $O\text{-}X_DY_DZ_D$, for TLP in $O\text{-}X_TY_TZ_T$)

No.	Fairlead coordinates			Anchor positions		
	x	y	z	x	y	z
	m	m	m	m	m	m
TAD01	-36.53	23.52	11.29	-266.37	1161.31	-476.25
TAD02	-31.75	23.52	9.41	-158.41	1138.19	-476.25
TAD03	31.73	23.52	7.62	1175.21	1083.45	-476.25
TAD04	36.51	23.52	7.62	1286.66	1006.78	-476.25
TAD05	36.51	-23.52	7.62	1286.66	-1006.79	-476.25
TAD06	31.73	-23.52	7.62	1175.21	-1083.47	-476.25
TAD07	-31.75	-23.52	9.41	-117.85	-1056.54	-476.25
TAD08	-36.53	-23.52	11.29	-228.52	-1031.78	-476.25
TLP01	-37.97	-25.955	6.45	-1315.92	-758.91	-463.75
TLP02	-37.97	25.955	6.45	-1312.15	765.45	-463.75

In the multi-platform system model, the TLP and TAD are connected by 4 hawsers between two platforms. The attached position on each platform is shown in Figure 4.1 (b) and (c). The coordinates of the attachment points are listed in Table 4.12.

Table 4.12 TLP/TAD hawser attachment point (For TAD in $O\text{-}X_DY_DZ_D$, for TLP in $O\text{-}X_TY_TZ_T$)

No.	Hull	x (m)	y (m)	z (m)
P1	DTV	-40.23	22.60	19.21
P2	TLP	34.88	37.79	33.05
P4	DTV	-40.23	18.03	9.95
P5	TLP	37.71	25.96	27.25
S1	DTV	-40.23	-22.60	19.21
S2	TLP	34.88	-37.79	33.05

S4	DTV	-40.23	-18.03	10.95
S5	TLP	37.71	-25.96	25.25

Besides the 10 mooring lines (8 TAD mooring lines and 2 TLP back lines), 4 hawsers are arranged between the platforms. Two surge lines are named as HAW1 and HAW2 while the two crossing lines are denoted as HAW3 and HAW4. The properties are provided in the Table 4.13 and detail configuration of hawsers are shown in Table 4.14.

Table 4.13 Hawser Line Properties

Normal		Surge line 18" Circ.		Crossing line 21" Circ.	
Tension	Elongation	Tension	Elongation	Tension	Elongation
% of MBL	% of L	MT	m	MT	m
0.00	0.0	0.00	0.00	0.00	0.00
5.00	5.8	22.50	1.66	30.15	2.62
10.00	9.2	45.00	2.64	60.30	4.15
15.00	11.4	67.50	3.27	90.45	5.14
20.00	13.2	90.00	3.78	120.60	5.96
30.00	15.7	135.00	4.50	180.90	7.08
40.00	17.5	180.00	5.01	241.20	7.90
60.00	20.2	270.00	5.79	361.80	9.11
80.00	22.2	360.00	6.36	482.40	10.02
100.00	24.0	450.00	6.88	603.00	10.83

Table 4.14 Hawser Configuration

No.	Section Description	Composition	Pretension	Distance	Length	Diameter	Dry weight	EA	MBL
			MT	m	m	mm	N/m	kN	MT
HAW1	TAD attachment P1	R4 chain	58.63	2.00	2.00	76.0	1136.0	583754	615.0
	Mid line P1-P2	Nylon (18''circ)		31.74	28.656	145.0	127.0	-	450.0
	TLP fairlead P2	R4 chain		2.00	2.00	76.0	1136.0	583754	615.0
HAW2	TAD attachment S1	R4 chain	58.63	2.00	2.00	76.0	1136.0	583754	615.0
	Mid line S1-S2	Nylon (18''circ)		31.74	28.656	145.0	127.0	-	450.0
	TLP fairlead S2	R4 chain		2.00	2.00	76.0	1136.0	583754	615.0
HAW3	TAD attachment S4	R4 chain	23.96	2.00	2.00	76.0	1136.0	583754	615.0
	Crossing line S4-S5	Nylon (21''circ)		47.01	45.122	168.0	171.0	-	603.0
	TLP fairlead P5	Wire		5.00	5.00	79.0	350.0	353100	522.0
HAW4	TAD attachment S4	R4 chain	23.96	2.00	2.00	76.0	1136.0	583754	615.0
	Crossing line S4-S5	Nylon (21''circ)		46.95	45.063	168.0	171.0	-	603.0
	TLP fairlead P5	Wire		5.00	5.00	79.0	350.0	353100	522.0

Since the symmetry of the platform of TLP and TAD, 0° and 45° wave headings are investigated for three configurations, namely, isolated TLP, isolated TAD and coupled TLP-TAD model. The model tests conducted by Dong et al. (2019) in the Deepwater Offshore Basin at Shanghai Jiao Tong University is used as primary benchmark for the extensive validation of the present numerical model.

Table 4.14 listed the random wave conditions for the present numerical study. JONSWAP wave spectrum with significant wave height H_s, peak wave period T_s and spectral steepness γ are selected. According to Dong et al. (2019), the wind and current force are considered and replaced by the equivalent constant force on platforms which is also applied in the present numerical simulation to replace the wind and current force. The viscous effect on the structures is estimated by Morison equation and added to the damping matrix in the motion equations.

Table 4.14 Environmental condition

Condition	Direction	H_s	T_P	γ
EC1	0	2.4	7	1.2
EC2	90	1.1	7	1.2

4.2 Mesh convergence of panel mesh and free surface mesh

Mesh sensitive study is conducted prior to the comprehensive numerical simulations of the multi-body platforms. The wave force acting on both TLP and TAD is used as measure to demonstrate the convergence of the numerical calculation. The meshes discretised for the structure boundary and free surface are investigated in the mesh convergence study for both the first-order and the second-order wave force calculated in the present study. The wave condition used in the mesh convergence study is from 0° with frequency 1.2rad/s.

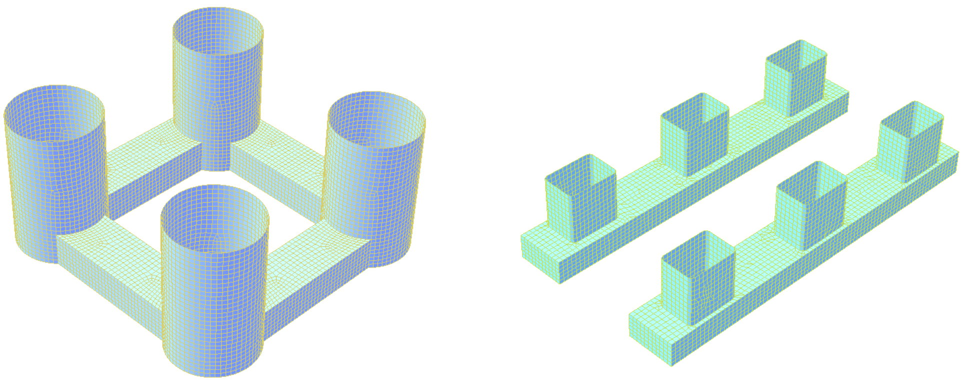

Figure 4.2 Visualization of the panel mesh of TLP (Karagiannopoulos) and TAD (right)

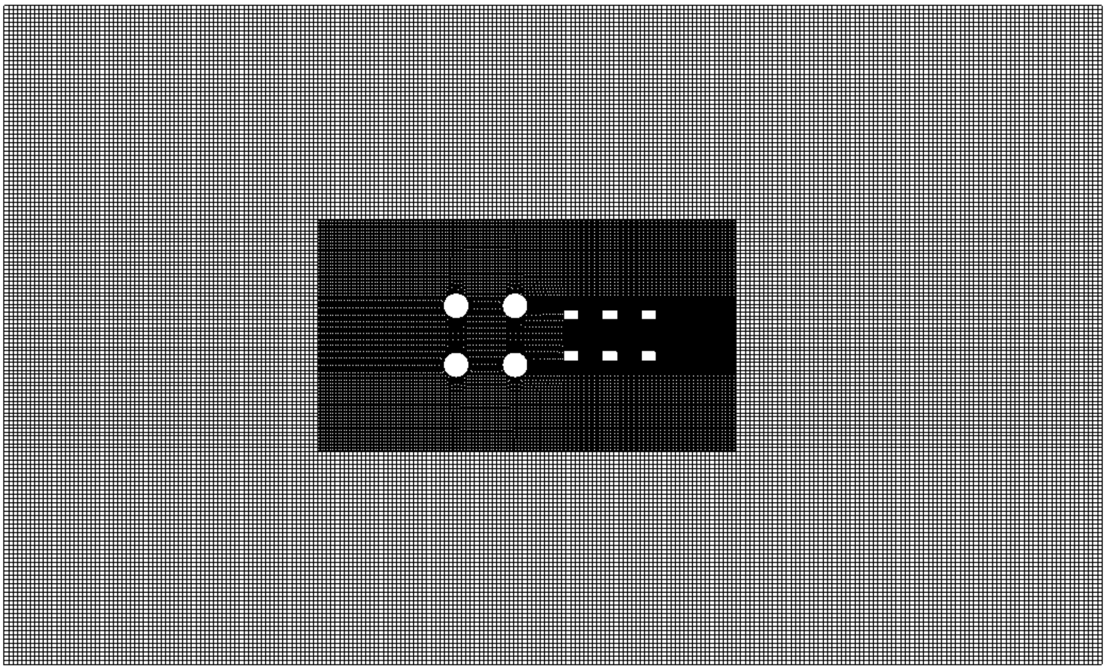

(a) Overall free surface mesh

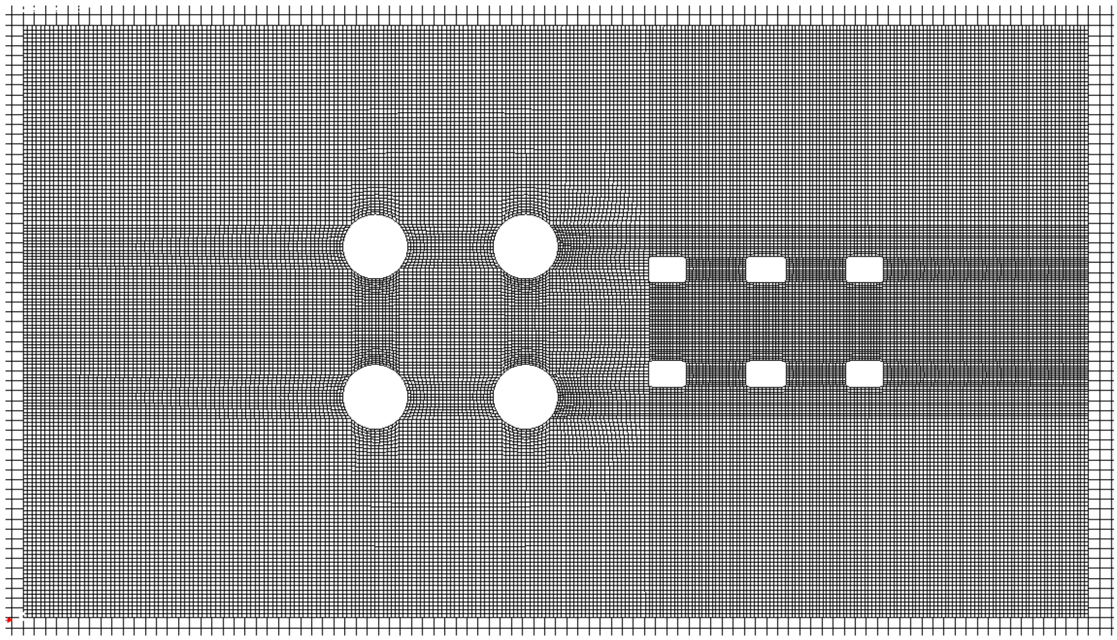

(b) Inner region of free surface mesh

Figure 4.3 Visualization of the second free surface mesh (a) Overall free surface mesh; (b) Inner free surface mesh

There are two kinds of mesh applied in the present numerical model. The panel mesh of structure is shown in Figure 4.2 and free surface mesh is shown in Figure 4.3. The accuracy of the first-order hydrodynamic results' is mainly depended on the panel mesh of the structure (Koo and Kim, 2005). The second-order result is sensitive to the free surface mesh. While much finer mesh is required for the free surface in order to improve the accuracy of the second-order result. There is inner region (fine mesh) near the structure and outer region (coarse mesh) applied in the free surface meshing to achieve the satisfactory accuracy in the second-order results while maintaining the overall computational cost since the water plane of the multi-platforms system is more complex than a single platform.

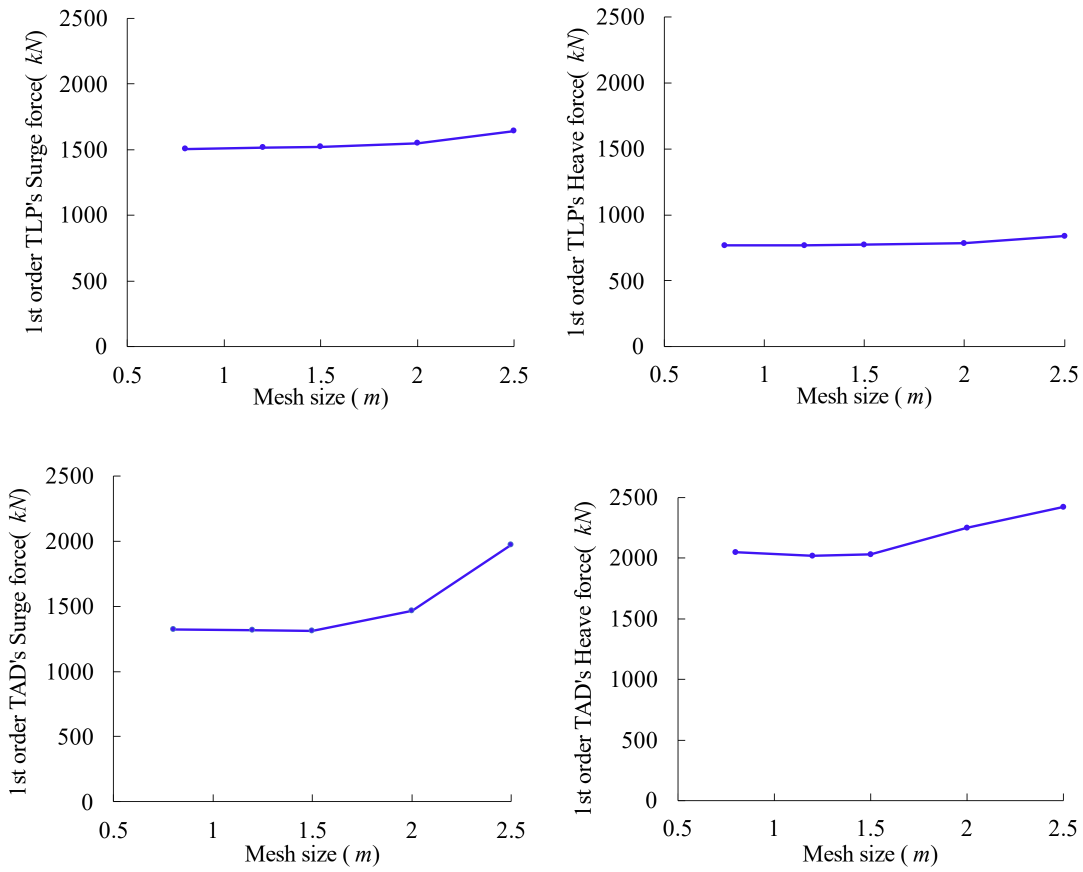

Figure 4.4 First-order surge and heave forces on TLP and TAD in coupled model using different meshes different meshes under 0° incident wave with frequency 1.2rad/s.

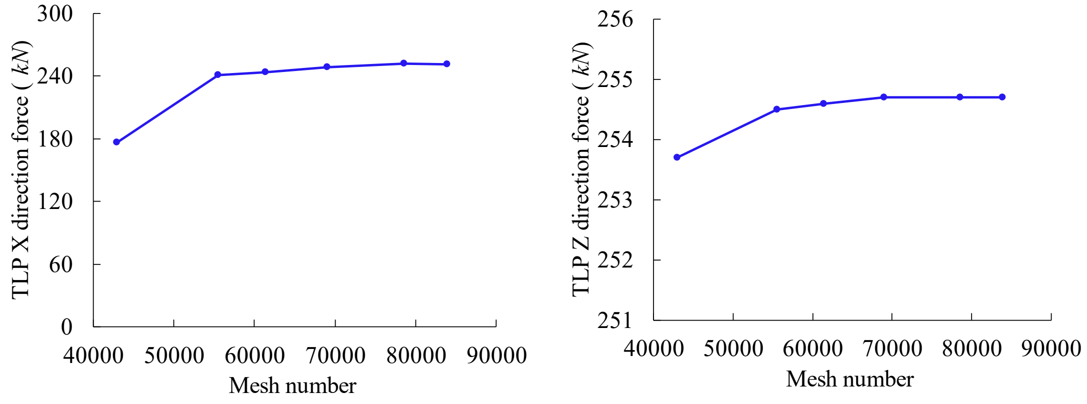

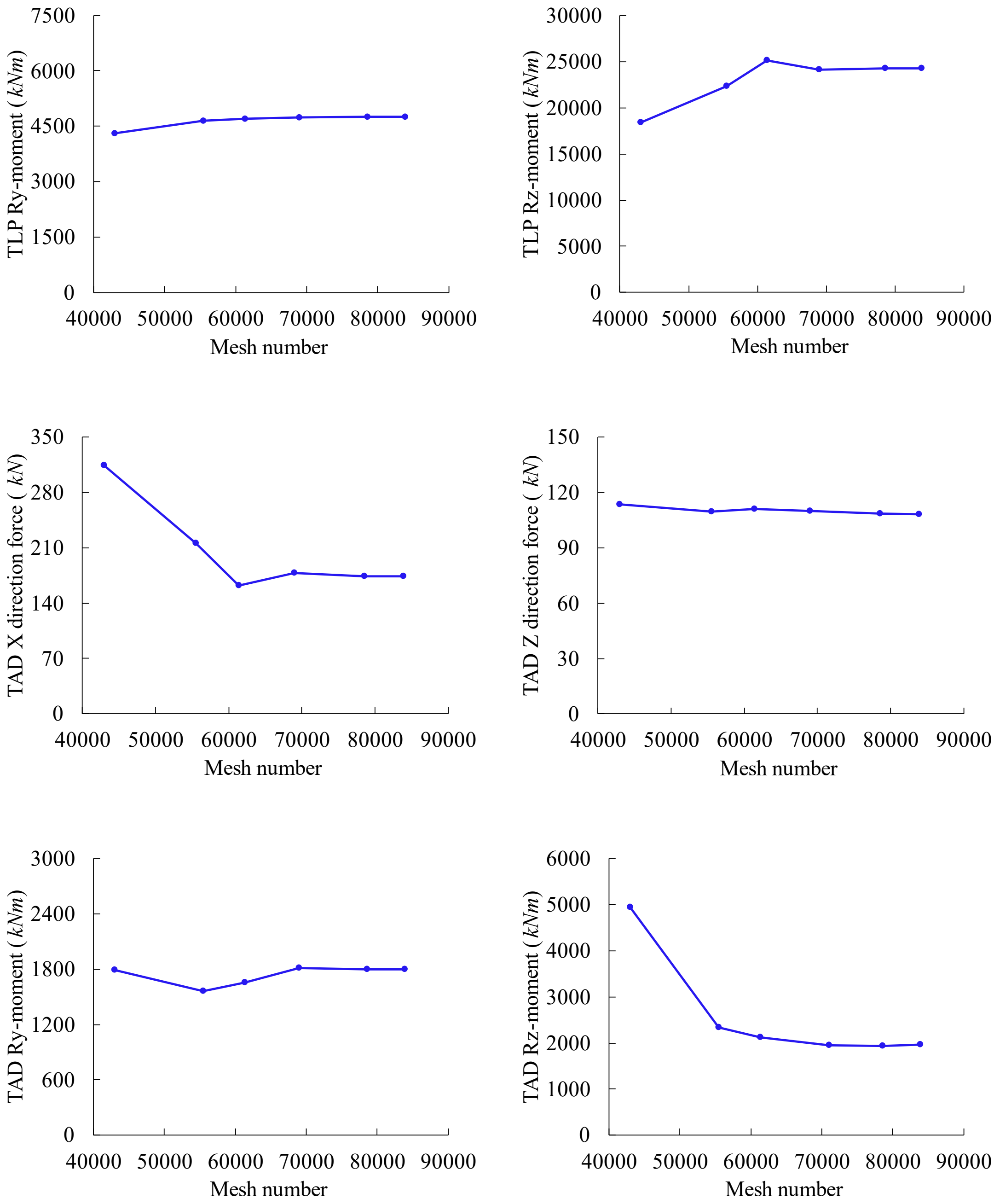

Figure 4.5 Second-order wave force on TLP and TAD in coupled model using different free surface meshes under 0° incident wave with frequency 1.2 rad/s.

The result of the first-order wave load under different panel meshes of TLP and TAD are shown in Figure 4.4. It is noted that the results of the first-order wave load become stable when the mesh size is smaller than 1.5m for both TLP with 6422 panels and TAD with 3988 panels indicating converged results of the first-order solutions.

According to Kristiansen et al. (2004), the second-order results are very sensitive to the free surface mesh. Numerical calculations of the second-order wave load using different free surface meshes are carried out. For the incident wave frequency at 1.2 rad/s, the double frequency for the second-order wave load is 2.4 rad/s which will be the highest incident frequency in this study. The results for the second-order wave load in surge, heave, pitch and yaw direction on both TLP and TAD are shown in Figure 4.5. As can be observed, most results of the second-order wave force become stable for the mesh number equalling or greater than 69004. Considering the balance of results accuracy and computation time, the free surface mesh number with 78588 is selected for the simulations.

4.3 Experimental model of the multi-body platform system

Experiments carried out by Dong et al. (2019) in the deepwater basin of Shanghai Jiao Tong University are used as the primary data to verify the numerical model. The length of the basin is 50m, the width is 40m and the maximum effective depth is 10 m. The large area of movable bottom helps to simulate the variable water depth from 0 to 10 m. A deepwater pit in the basin, with a total depth of 40m, can model the full-length tendon and riser of TLP without truncation. There is a multi-flap wave generator on both sides of the basin. The absorbing beaches are installed in the other two sides to absorb the wave.

The scale of the experimental model is 1:40, and the corresponding experimental water depth is 12.15m. Since there is a deepwater pit in the basin with depth of 40m, the full-length of the 8 tendons and 4 TTRs can be modelled. However, there is still truncations applied to the 4 SCRs and 2 back lines of the TLP and 8 mooring lines in TAD system since the corresponding experimental water depth exceeding the effective depth of basin.

Owing to the complexity of the tendons, risers, and mooring system with nonlinear stiffness, it is quite difficult to model the system accurately in the basin. The tendons are sized to preserve the outer diameter using aluminium tubes and steel wires are placed inside it evenly to match the specified wet weight.

The springs are employed between the aluminium tubes to provide the axial stiffness to whole tendons. There are ball joints at both ends of each tether of tendon to provide the free rotation in all directions. The TTRs are modelled by steel tubes and wires. Springs are also applied in TTRs model to provide the axial stiffness. The SCRs are modelled by steel wires with additional weights. Further details can be found in Biao et al. (2018). The model of whole multi-platform system is systematically in the model test. The pretension of the tendons and mooring lines are adjusted to make sure the whole system model is reliable. The tension transducers are applied to measure the tension along tensions and a non-contact optical motion capturing system is used to collect the motion response of each sub-platform in multi-platform model.

Three different configurations, including TLP only, TAD only and TLP-TAD coupled are tested for comparison. Three main types of experiments are conducted, including decay tests, static offset tests, and irregular wave tests. The waves are described by JONSWAP wave spectrum using significant wave height Hs, peak wave period Tp and spectral peakiness parameter γ. The model test is carried out 22.8 min for each case to achieve the three hours predication which is widely used in the offshore forecast. Dong et al. (2019) provided the details of the experiment.

4.4 Motion of platforms in multi-body system

The results of numerical simulation and the model tests results are compared in this section to validate the accuracy of the numerical model used in the present thesis. Both motion and acceleration of each platform in the multi-body system are validated to confirm the reliability of the numerical model for the coupled TLP-TAD system. The motion of each platform is described respect to the reference coordinate system which is located at the centre of gravity of each platform, fixed in space and coincided with local system at rest.

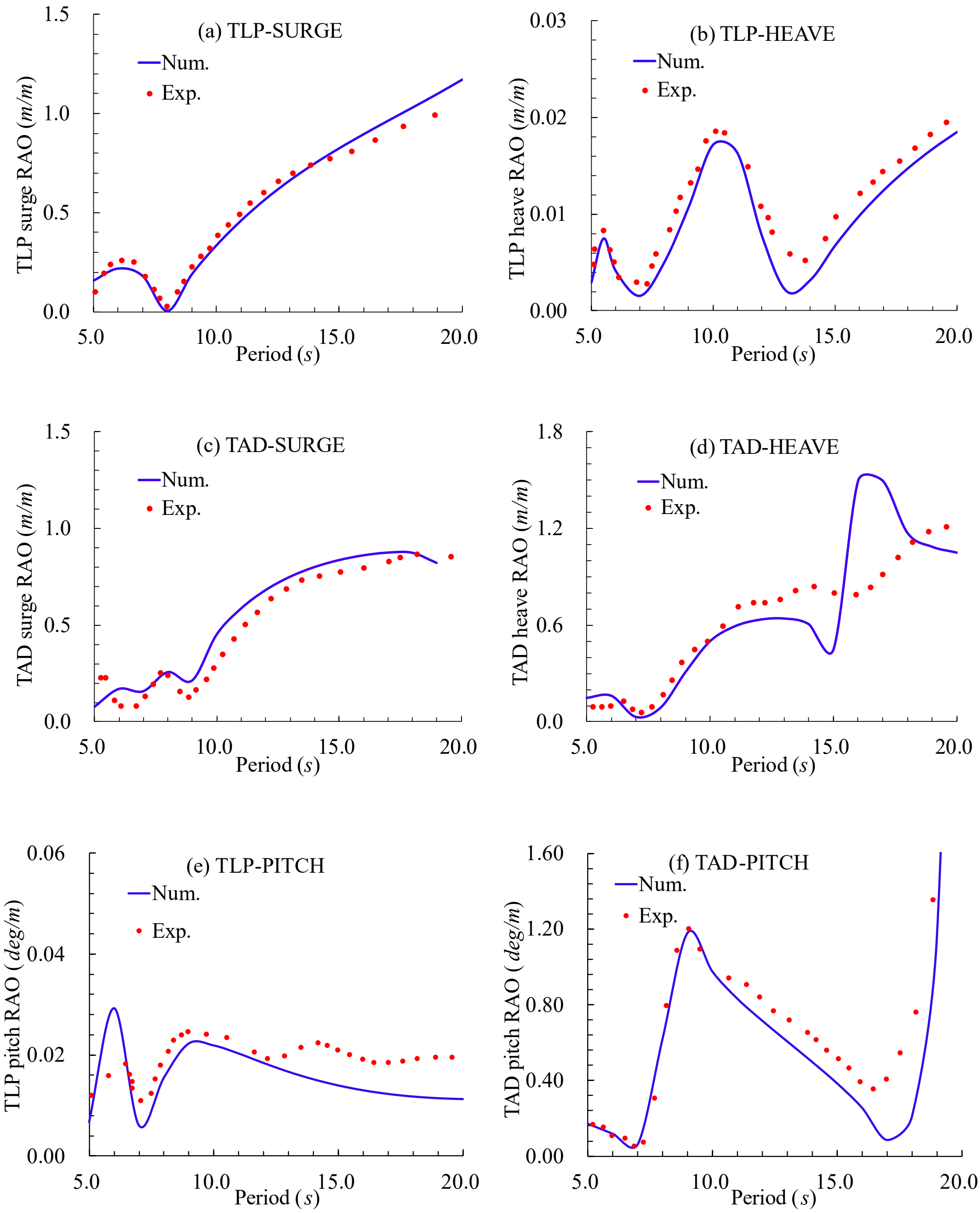

Figure 4.6 Translation motion (surge and heave) and rotation motion (pitch) RAOs of isolated TLP and isolated TAD model under 0° incident wave. (Numerical result Vs. Experiment result of Dong et al. (2019))

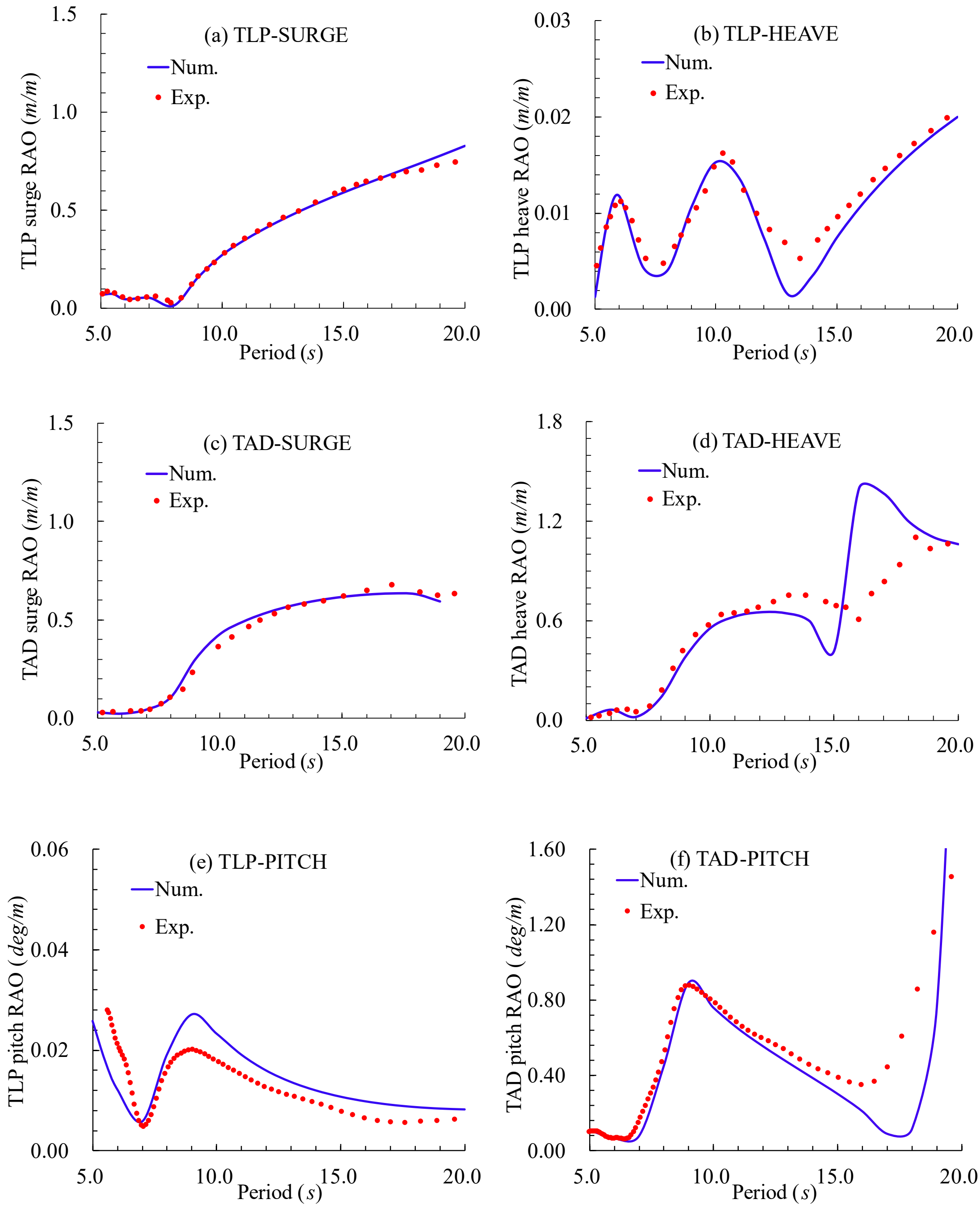

Figure 4.7 Translation motion (surge and heave) and rotation motion (pitch) RAOs of the isolated TLP and the isolated TAD model under 45° incident wave. (Numerical result Vs. Experiment result of Dong et al. (2019))

The global response of isolated TLP and isolated TAD model are analysed as the first step and the results are shown in Figure 4.6 and Figure 4.7 respectively (for both 0° and 45° wave heading as shown in Figure 4.1). Surge, heave and pitch motions are presented since they are more significant under 0° incident wave and 45° incident wave and can subsequently leads to significant impact on the safety of the coupled system both to the platform and the mooring and riser systems in operation. Figure 4.6 and Figure 4.7 show a good agreement in both surge, heave and pitch direction of TLP motion response, except the differences occurring at the trough of heave motion (Figure 4.6 (b) and Figure 4.7 (b)). The discrepancy between the numerical and experiment result of heave motion is due to the viscous damping in model test. The numerical model is established in full scale and calculated based on potential theory. The fluid is assumed as ideal fluid without viscosity. The Reynolds number are lower in model test than that in full scale numerical simulation which result in a higher proportion of viscous damping in the experiment. The other reason for discrepancy observed in the heave and pitch motion (Figure 4.6 (b), (e) and Figure 4.7 (b), (e)) of TLP in both 0° and 45° wave headings is that the amplitude of the heave and pitch motion is very small (smaller than 0.01m and 0.1°), there is a limitation of non-contact optical acquisition system to get a high accuracy measurements during the model test. Additionally, the response of heave motion under 0° and 45° wave headings are practically the same. However, the surge motion under 45° incident waves is reduced significantly compared to that under 0° incident waves primarily due to the wave load in 45° direction being distributed into both surge (inline) and sway (transverse) direction. The TAD surge and pitch motion response from the present numerical simulation has a good agreement with the model test (see Figure 4.7 (c) and (f)). The natural period of heave motion for TAD is observed in the numerical result at approximate 16.5s-17.5s. For the discrepancy of TAD's heave motion amplitude that test data does not show the heave resonance peak maybe due to that the resolution of the incident white noise wave is not sufficiently high. The other possible reason caused discrepancy of the heave motion amplitude at the natural period is the viscous damping is fully accounted in model test in contrast to the numerical simulations based on potential flow theory. Potential damping is typically dominate in the normal range of incident wave period, however, at the resonance response, the viscous damping becomes more critical. This also explained the discrepancy of the pitch motion response of TAD. The heave motions under both 0° and 45° incident wave direction are approximate same. However, similar to TLP, there is a significant reduction of surge and pitch motion under 45°

incident wave compared to that under 0° incident wave. In general, the motion RAOs for isolated TLP and TAD in above directions show an agreement between numerical result and experimental result. The numerical model will be applied to perform the subsequent multi-platform coupled analysis.

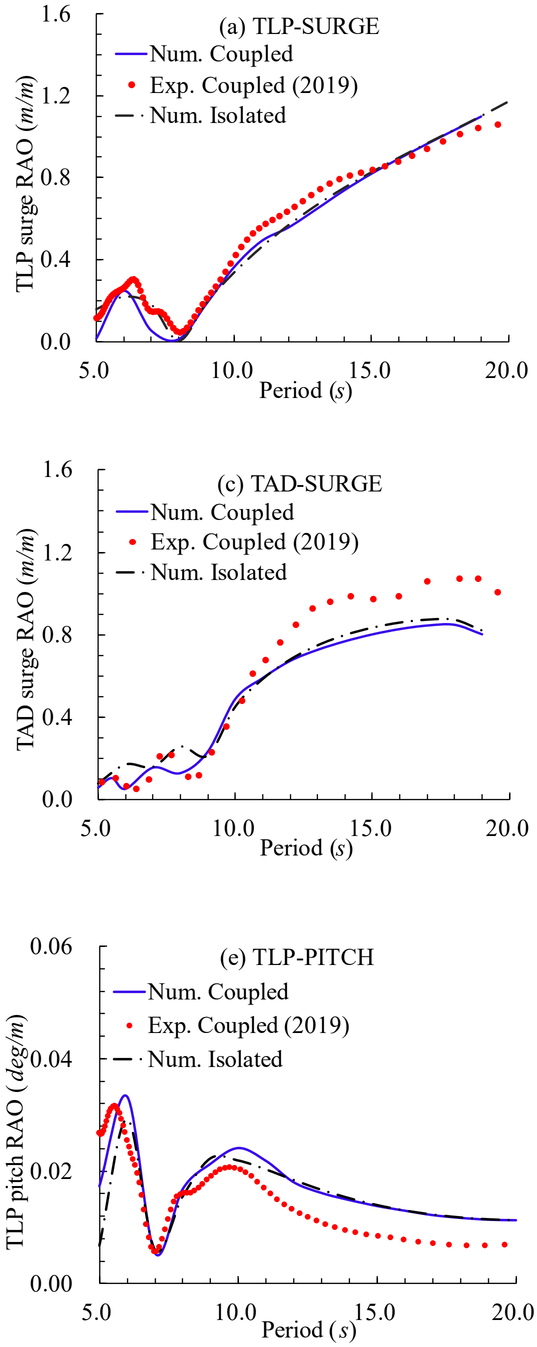

Figure 4.8 Translation motion (surge and heave) and rotation motion (pitch) RAOs of TLP and TAD in coupled system under 0° incident wave. (Numerical result Vs. Experiment result of Dong et al. (2019))

0° wave heading was selected for coupled TLP-TAD configuration to validate the multi-body coupled model. The global motion of the coupled TLP-TAD under 0° wave heading (EC1) is investigated and results are shown in Figure 4.8. The numerical results for the isolated TLP and TAD are also shown in the figure for comparison. Both translation and rotation motion RAOs are obtained. Some discrepancy of the TAD in surge motion and pitch motion (Figure 4.8 (c) and (f)) at large incident wave periods is observed. This is mainly attributed to that for the incident irregular wave spectrum with significant wave period T_s = 7s, there is very limited wave energy in the long wave period beyond 12s. However, the result at the shorter periods like 5s-6s shows a good agreement between numerical and experiment results. The experimental result over the period around 12s is not as accurate as the shorter periods. Similar discrepancy is also reported by Dong et al. (2019) for the comparison of results between the experiments and theoretical study.

There is a slight fluctuation appearing in the short periods in surge of TAD (Figure 4.8 (c)) owing to the hydrodynamic interaction in coupled TLP-TAD system case. The surge motion of TLP in multi-body system is approximately same with TLP in isolation case. However, clear reduction in heave motion for both TLP and TAD (Figure 4.8 (b) and (d)) are observed in coupled TLP-TAD system for large range of wave period comparing with the isolated TLP case. This is attributed to the connecting hawser between two platforms restricting the vertical motions of both TLP and TAD. It is noted that the connecting hawsers are arranged in the horizontal plane at the beginning of simulation. However, considering the narrow spacing between the two platforms especially with the relative motion increasing between the two platforms in multi-body system, the restriction from the connecting hawsers to the vertical plane motions can be significantly increased. Under such condition, the hawser is clearly no longer in the horizontal plane and there will be a force component caused by hawser in vertical direction to restrict the vertical plane motions of the two platforms. Similar to the TLP/TAD in isolation model, there are differences in heave RAOs between model test and numerical result for coupled TLP-TAD model primarily due to the limitation of the incident wave energy. In general, the numerical and experimental results show a good agreement indicating that the numerical model is well established and thus will be employed in the following coupled analysis of the multi-body system. There is a slight amplifying impact of pitch motion in TLP (Figure 4.8 (e)) under the shorter period (5s-6s). This is caused by the adjacent platform providing an addition potential on the TLP since the reflection wave and the first-order pitch moment also shows the same phenomenon.

The statistic results of relative distance measured by the distance between the coupled TLP-TAD connected by hawsers are shown in Table 4.15. It is noted that such relative motion or distance between the two adjacent platforms is dependent on the mechanical property of the hawsers and the hydrodynamic interaction of the two platforms. The results of relative motion for the coupled TLP-TAD system shows good agreement.

Table 4.15 Statistics of relative distance between TLP and TAD in multi-platform model with hydrodynamic interaction

Model	Maximum	Minimum	Range	Mean value	Standard Deviation	Discrepancy
Numerical	25.6m	23.9m	1.7m	24.75m	0.19	0.064
Experimental	23.9m	22.34m	1.64m	23.2m	0.21	

The acceleration of surge and heave for TLP and TAD in head wave (0°) are shown in Table 4.16 to validate the wave force on the coupled TLP-TAD model owing to the sensitivity of surge and heave for TLP and TAD respectively.

In Table 4.16, most statistic values of TLP and TAD acceleration show good agreement with model test except the heave motion of TLP. The heave acceleration of TLP shows a larger discrepancy of standard deviation, and such discrepancy may be caused by the unusual mooring lines specifically including 8 tendons, 4 risers and 6 equivalent catenary lines of TLP. It is worth noting that the arrangement of mooring system in experiment is different to the numerical simulation, however the total vertical force is kept same and the heave acceleration range of TLP between numerical and experiment result shows good agreement indicating the results in heave direction are reliable. The good agreement in acceleration of TLP-TAD model and their relative motion demonstrates that the numerical simulations for both wave load and motion response of the coupled TLP-TAD system are reliable.

Table 4.16 The acceleration of TLP/TAD in numerical simulation and model test

Acceleration of TLP/TAD	Model	Maximum	Minimum	Range	Standard Deviation
Surge acceleration of TLP	Numerical	0.3677	-0.3925	0.7602	0.09518
	Experiment	0.392	-0.403	0.795	0.103
Heave acceleration of TLP	Numerical	0.1531	-0.1549	0.308	0.04868
	Experiment	0.147	-0.154	0.301	0.029
Surge acceleration of TAD	Numerical	0.285	-0.3026	0.588	0.073
	Experiment	0.32	-0.331	0.651	0.083
Heave acceleration of TAD	Numerical	0.1941	-0.1956	0.3897	0.056
	Experiment	0.192	-0.168	0.36	0.048
Pitch acceleration of TLP	Numerical	0.1955	-0.185	0.3805	0.039
	Experiment	0.252	-0.259	0.511	0.052
Pitch acceleration of TAD	Numerical	0.4756	-0.5374	1.013	0.137
	Experiment	0.399	-0.418	0.817	0.11

4.5 Wave force on TLP and TAD in multi-body platform system

4.5.1 First-order wave load on TLP and TAD in multi-body coupled model

The wave loads on TLP and TAD in both coupled TLP-TAD model and isolated TLP/TAD model with identical 0° incident wave (from negative *x*-direction shown in Figure 4.1) are shown in Figure 4.9 and Figure 4.10 respectively. The general trend of the first-order wave load in surge and heave directions on TLP and TAD for coupled TLP-TAD model and isolated model are similar. However, it can be clearly observed that there is a higher peak of wave load in surge direction on TLP at wave period around 6.5s (Figure 4.9 (a)). Since the TLP is at the upstream position (with 0° incident wave as shown in Figure 4.1), the only difference between isolated TLP and coupled TLP-TAD model is the existence of adjacent TAD downstream introducing the hydrodynamic interaction between two platforms. It indicates that the interaction between two platforms in coupled model is directly responsible to an increased amplitude of the first-order surge force on TLP at short wave period around 6.5s (Figure 4.9 (a)). The heave force on TLP (Figure 4.9 (b)) in coupled model shows fluctuating pattern and increasing with rising period compared to a rather smooth increasing trend after an initial peak at low period for the TLP in isolation. This demonstrates that the interaction between two platforms of coupled TLP-TAD model leads to oscillatory heave force on TLP though it is positioned upstream (with 0° incident wave as shown in Figure 4.1) in addition to the increased first-order surge force on TLP. This interaction also has impact on the moment in pitch direction as shown in Figure 4.9 (c). The moment in pitch direction is higher in coupled which is similar to that in surge force and there is also a fluctuating pattern in pitch moment like heave force. As shown in the Figure 4.9 (a), (b) and (c), with the increase of the incident wave period, the difference of the first-order wave loads between coupled model and isolated model becomes smaller indicating weakened interaction between TLP and TAD as the incident wave period increases.

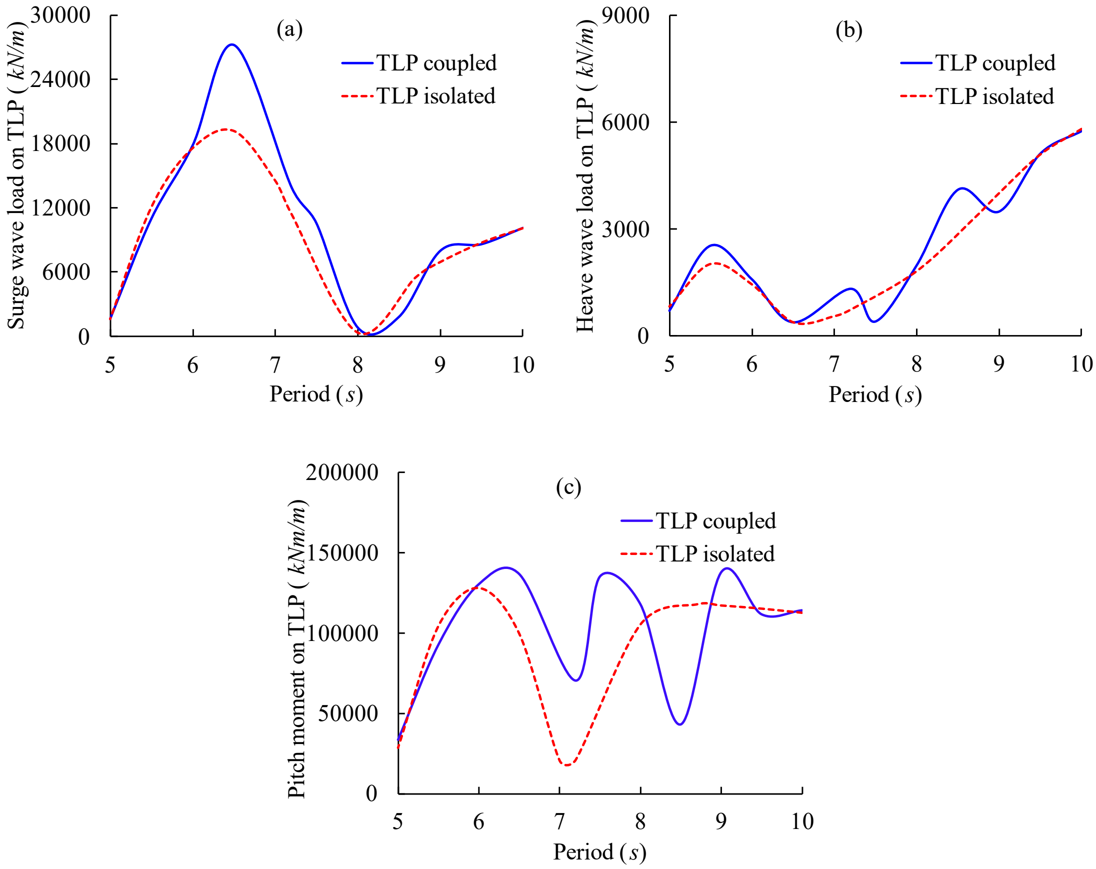

Figure 4.9 First-order wave load RAOs on TLP in (a) surge, (b) heave and (c) pitch under 0° incident wave

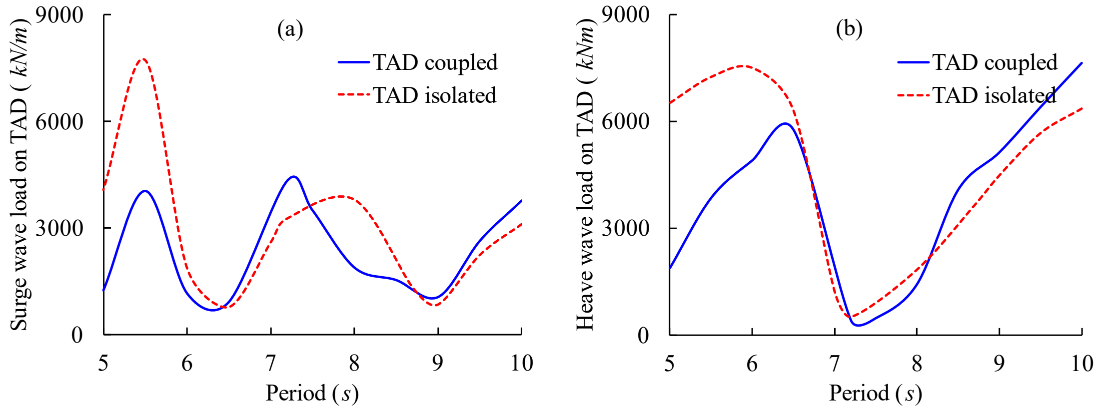

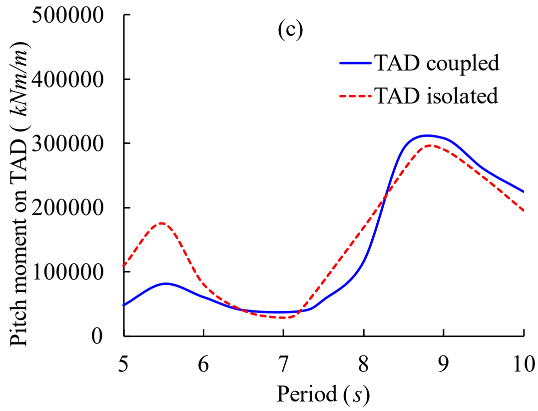

Figure 4.10 First-order wave load on TAD in (a) surge, (b) heave and (c) pitch under 0° incident wave

The first-order wave force and moment on TAD in surge, heave and pitch direction is shown in Figure 4.10. Shielding effect caused by the upstream TLP can reduce the wave load on TAD since it is located at the lee position of the configuration for the multi-body model. It can be clearly observed that the wave load in both surge and heave on TAD are reduced significantly by the adjacent TLP especially at the wave period around 5s-6.5s owing to the shielding effect. There is a large reduction of the incident wave energy caused by shielding effect leading to the lower wave load on TAD. In addition, with weakened incident wave on the TAD, the interaction between bodies is also weakened. It is noted that the shielding effect becomes weak with increasing incident wave period because the ratio of the diameter of upstream structure (D) and incident wavelength (λ) becomes smaller. Consequently, the interaction between two platforms becomes stronger since less reduction of incident wave caused by shielding effect as incident wave period increase. Both shielding effect and hydrodynamic interaction between bodies have impacts on the wave load on TAD. As shown in Figure 4.10 (a), (b) and (c), with the increasing wave period (6.5s-10s), the first-order wave loads on TAD in coupled model are sometimes larger than that in isolated model. This indicates that the shielding effect is not uniform across the incident wave period and additional factor due to the interaction between the two bodies in the coupled model may also contribute to the increase of wave load on TAD. It is noted that the influence of such interaction also exists in the shorter periods (5s-6.5s), though it is not dominant. Shielding effect and interaction among the two adjacent bodies become weak with increasing incident wave period since the ratio of the diameter of upstream structure (D) and incident wavelength (λ) becomes smaller. The wave force in coupled TLP-TAD model sometimes becomes higher indicates that shielding effect reduce more rapidly which makes the interaction between the two bodies more dominant resulting higher wave force on TAD in coupled model.

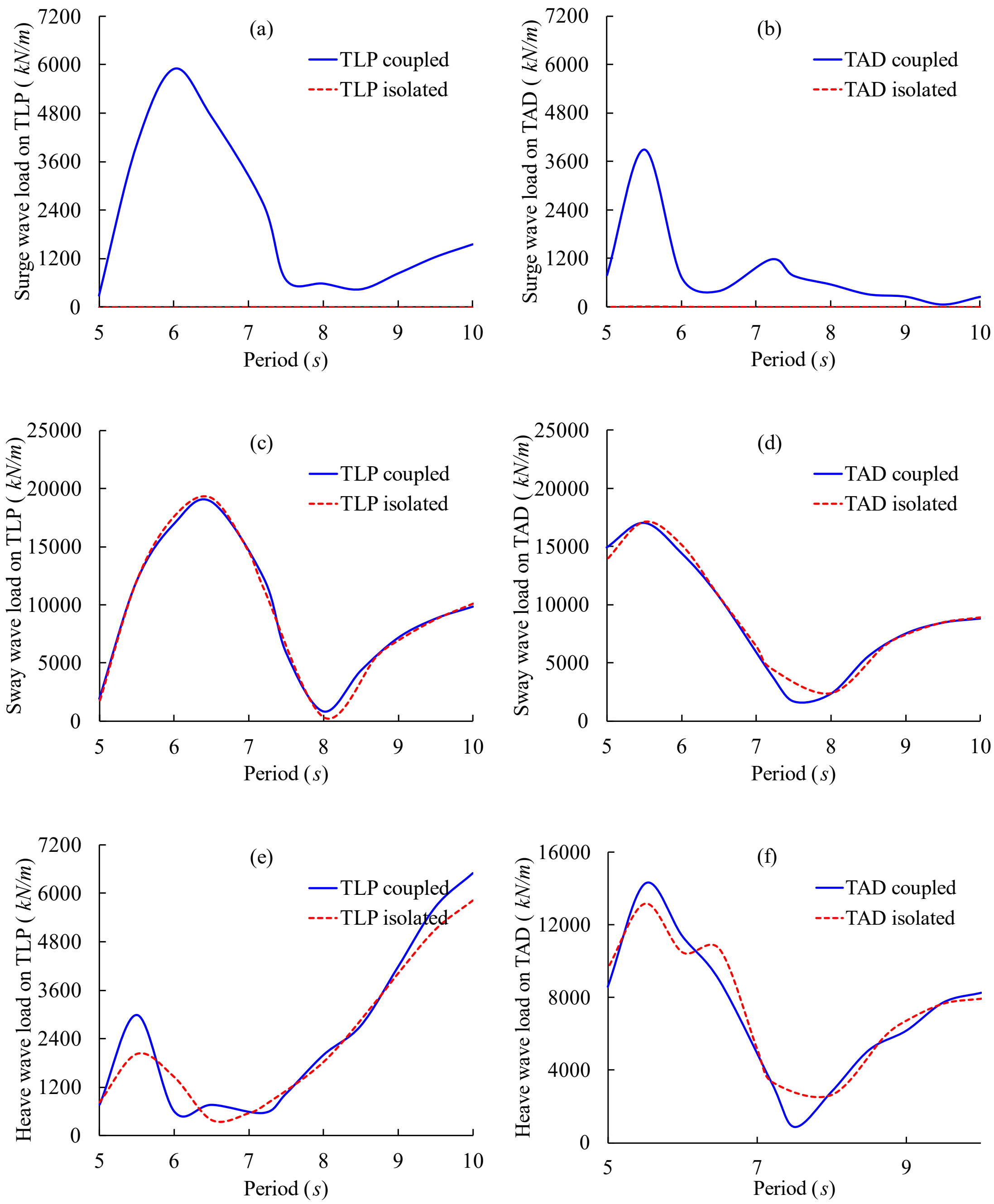

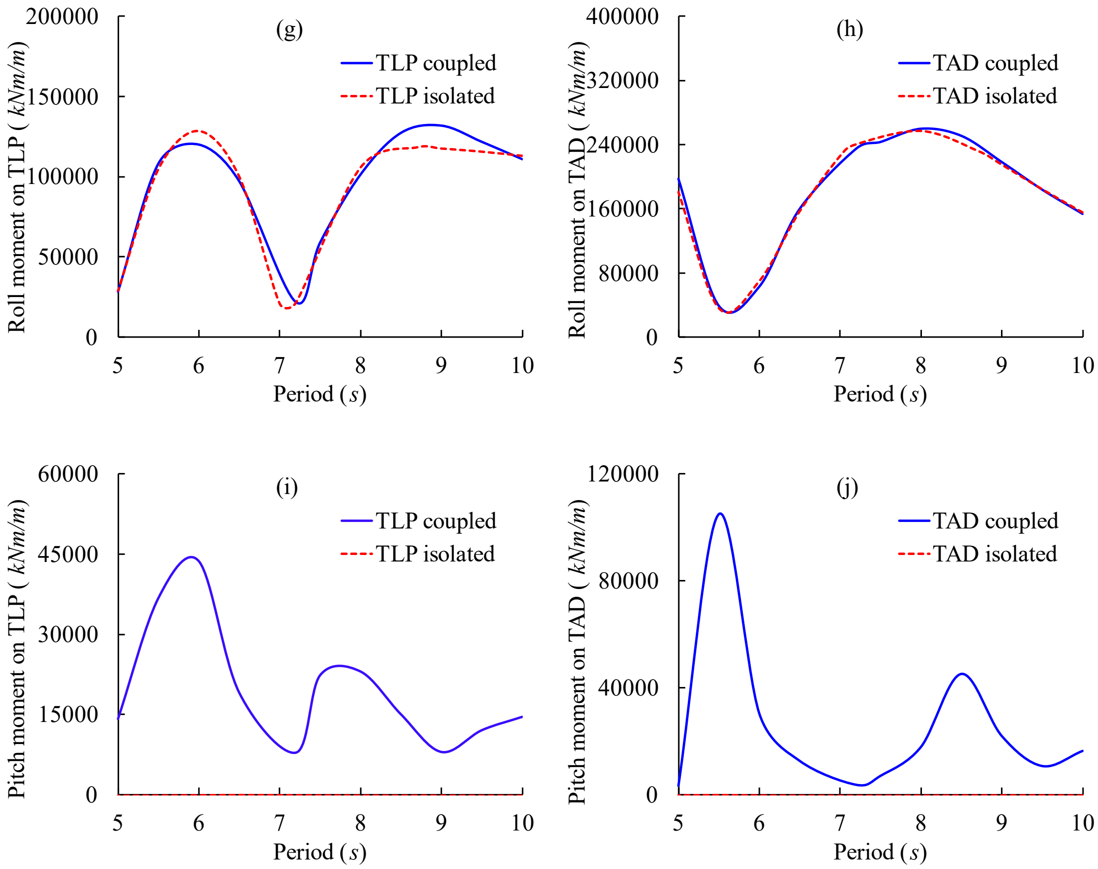

Figure 4.11 First-order wave load on TLP in (a) surge, (c) sway, (e) heave (g) roll and (i) pitch and TAD in (b) surge, (d) sway, (f) heave, (h) roll and (j) pitch under 90° incident wave

To further examine the impact on wave loads due to interaction between adjacent platforms in multi-body system, a 90° incident wave which is from the negative *y*-axis (beam sea condition) is selected to investigate the wave load on TLP and TAD. There is no shielding effect on either TLP or TAD under the beam sea. The first-order wave load on TLP and TAD in translation and rotation are shown in Figure 4.11. The surge force and pitch moment on TLP and TAD isolated model is seen very small comparing to those in the coupled model as shown in Figure 4.11. However, the first-order wave force in sway, heave and moment in roll on TLP and TAD in coupled TLP-TAD model are similar to that in isolated TLP/TAD model. In contrast to the isolated platform model, this indicates that interaction between two platforms in the coupled model introduces the first-order wave load in surge direction under beam sea condition. This is mainly due to the fact that the TLP and TAD in multi-body coupled model are arranged in surge direction. The surge components of diffraction and radiation caused by one body impact on the other resulting in much larger surge forces on the TLP and TAD respectively in multi-body model. In addition, the first-order heave forces on TLP and TAD in coupled model and isolated model are similar indicating little impact of interaction between platforms on the first-order heave force.

4.5.2 Second-order wave load on TLP and TAD in coupled model

The accurate estimate of sum-frequency wave force is crucial to the design of tendons preventing the undesired high-frequency "springing" and "ringing" of TLP in irregular wave. Such nonlinear effect can be further complicated by the interaction of the adjacent floating structures in the multi-body system. In the present study, near-field integral method is applied to calculate the complete second-order quadric transfer function (QTF) matrix which is then used to calculate the sum-frequency wave load on TLP. When the incident irregular wave components' periods are equal ($T_1 = T_2$), the sum-frequency wave load problem under irregular wave becomes identical to the double-frequency wave load problem in regular wave which is shown in the diagonal terms of the sum-frequency QTF matrix.

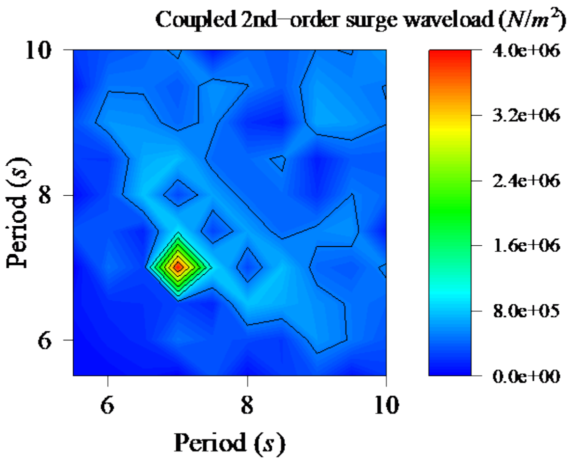

(a)

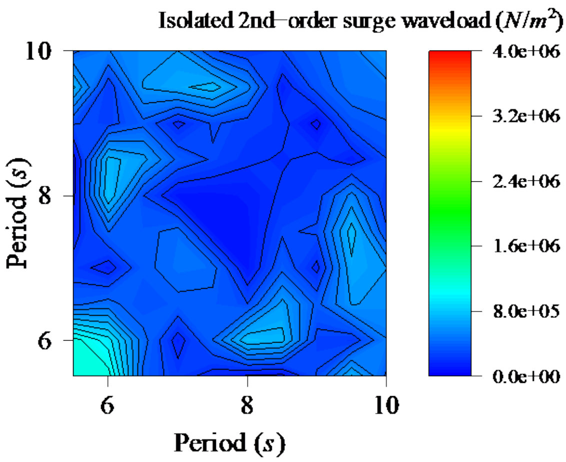

Isolated 2nd–order surge waveload (N/m^2)
Period (s)
Period (s)
4.0e+06
3.2e+06
2.4e+06
1.6e+06
8.0e+05
0.0e+00

(b)

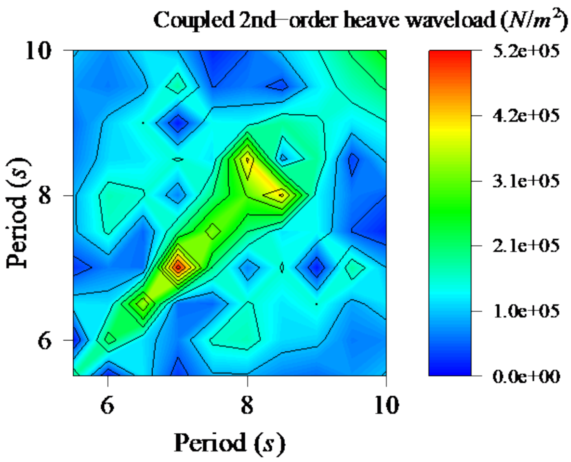

Coupled 2nd–order heave waveload (N/m^2)
Period (s)
Period (s)
5.2e+05
4.2e+05
3.1e+05
2.1e+05
1.0e+05
0.0e+00

(c)

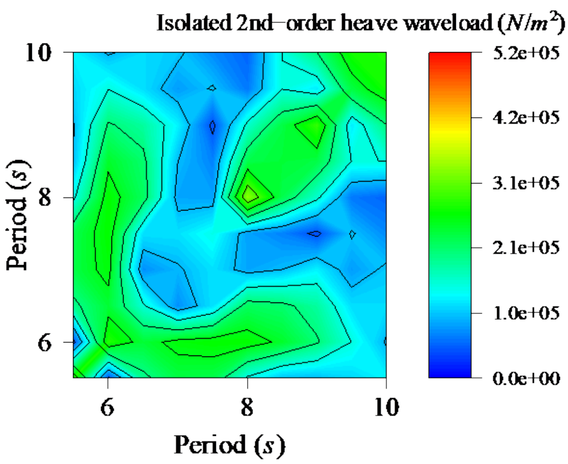

Isolated 2nd–order heave waveload (N/m^2)
Period (s)
Period (s)
5.2e+05
4.2e+05
3.1e+05
2.1e+05
1.0e+05
0.0e+00

(d)

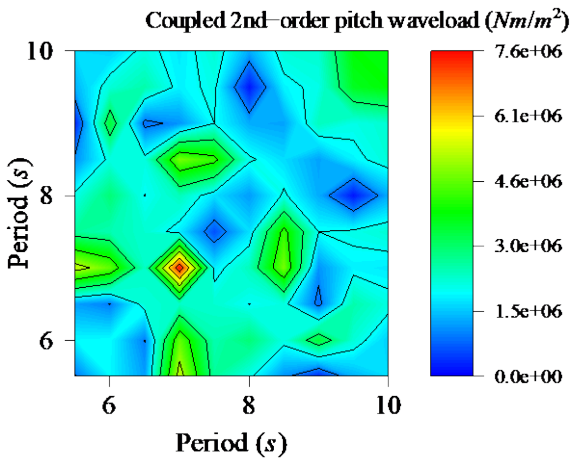

(e)

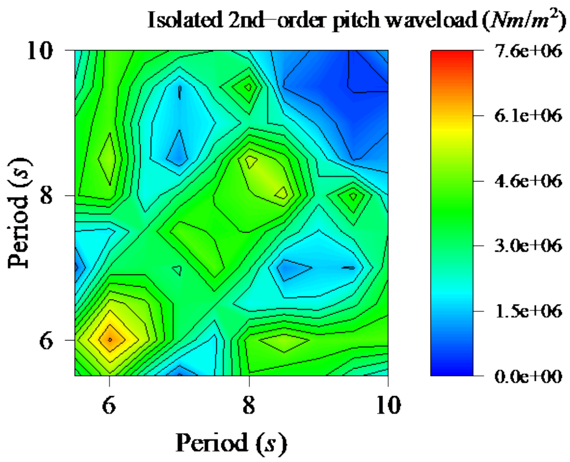

(f)

Figure 4.12 Sum-frequency QTF matrix for wave loads on TLP under 0° incident wave. Surge force on TLP in: (a) Coupled TLP-TAD model, and (b) Isolated TLP model; Heave force on TLP in: (c) Coupled TLP-TAD model, and (d) Isolated TLP model; Pitch moment on TLP in: (e) Coupled TLP-TAD model, and (f) Isolated TLP model.

The sum-frequency wave loads on TLP in coupled model in both surge, heave and pitch directions are compared with those in TLP in isolated model under 0° incident wave in Figure 4.12. Because of the existence of the adjacent TAD, the sum-frequency wave load QTF have been altered. There is a peak value at $T_1 = T_2 = 7.1s$ of the TLP's surge sum-frequency QTF matrix in coupled model (Figure 4.12 (a)) comparing with the TLP in isolated model (Figure 4.12 (b)). It is noted that the peak of sum-frequency wave load in surge on isolated TLP model occurs at the wave periods around $T_1 = T_2$=5.5s and it is lower than that in coupled model. When the incident wave components' periods $T_1 \neq T_2$, the sum-frequency surge force in coupled model is slightly higher than those in isolated model. The significant higher peak value at the diagonal line of the sum-frequency QTF matrix observed in coupled model (Figure 4.12 (a)) is caused by the existence of the TAD in coupled model. It means that the maximum double-frequency wave load on TLP becomes higher due to the interaction with the adjacent TAD. Similar to surge force, there is also an obvious peak when $T_1 = T_2$ in heave sum-frequency force QTF matrix (Figure 4.12 (c)). Most of double-frequency wave loads in isolated model (Figure 4.12 (d)) are seen lower than those in coupled model (Figure 4.12 (c)) where a peak of wave load is observed in the diagonal line of the sum-frequency heave force QTF matrix. However, when the $T_1 \neq T_2$, the sum-frequency heave forces on TLP in coupled model (Figure 4.12 (c)) are smaller than those in TLP in isolated model (Figure 4.12 (d)) especially at the area representing combination of wave components frequencies $T_1 =$ 6s to 9s and $T_2 =$ 6s to 9s indicating that the interaction with the adjacent TAD can change the distribution of the sum-frequency wave force and increase the maximum value at double-frequency of the second-order wave force in heave direction. There is a trend of sum-frequency pitch moment QTF in Figure 4.12 (e) and (f) which is similar to that of heave force. The peak force and moment in heave and pitch at $T_1 = T_2 \approx 7s$ become much higher and other sum-frequency wave load QTF ($T_1 \neq T_2$) become lower since the existence of the adjacent platform. Such larger increase in double-frequency wave force is main characteristics which can lead a highly nonlinear "ringing" response and fatigue damage to tendons and risers.

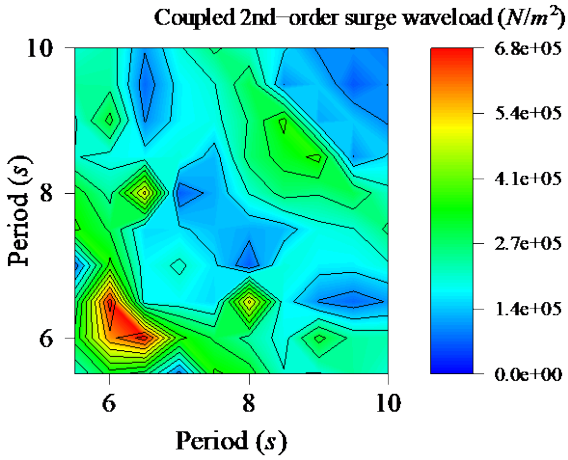
Coupled 2nd–order surge waveload (N/m^2)
Period (s)
Period (s)
10
8
6
6
8
10
6.8e+05
5.4e+05
4.1e+05
2.7e+05
1.4e+05
0.0e+00

(a)

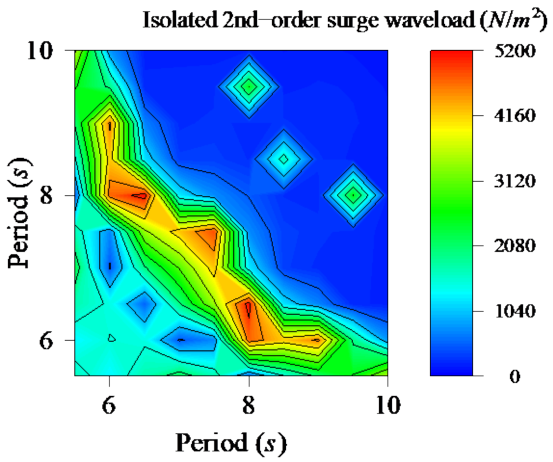
Isolated 2nd–order surge waveload (N/m^2)
Period (s)
Period (s)
10
8
6
6
8
10
5200
4160
3120
2080
1040
0

(b)

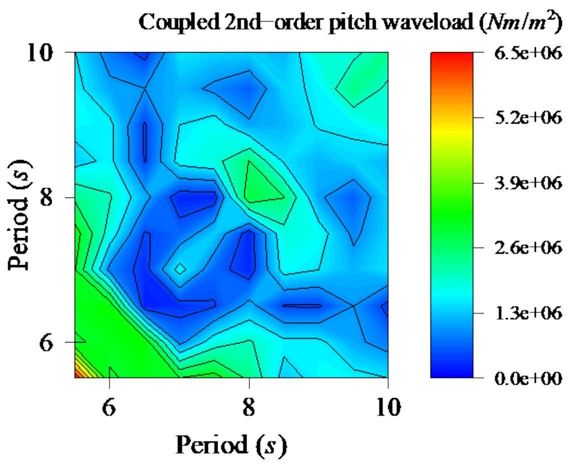
Coupled 2nd–order pitch waveload (Nm/m^2)
Period (s)
Period (s)
10
8
6
6
8
10
6.5e+06
5.2e+06
3.9e+06
2.6e+06
1.3e+06
0.0e+00

(c)

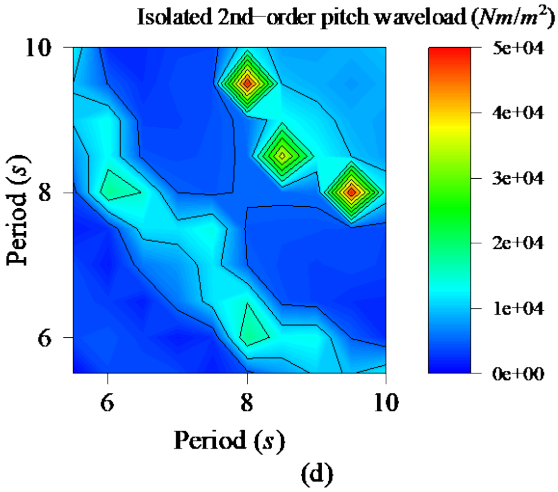

Figure 4.13 Sum-frequency QTF matrix of TLP under 90° incident wave. Surge force on TLP in (a) Coupled TLP-TAD model, and (b) Isolated TLP model; Pitch moment on TLP in (c) Coupled TLP-TAD model, and (d) Isolated TLP model.

Sum-frequency wave loads on TLP under beam sea (90° incident wave) are also investigated in the present study. Without shielding effect, the interaction between two bodies is the only factor influencing the wave load on TLP and TAD in coupled model under the beam sea. It is noted that the legends of the second-order surge force in Figure 4.13 (a) and (b) and pitch moment in Figure 4.13 (c) and (d) are different since the interaction between TLP and TAD results in much higher sum-frequency wave load in surge and pitch direction on TLP in coupled model than that in the isolated model as shown in Figure 4.13. However, the sum-frequency heave force on TLP in coupled model is lower than that in isolated model under the beam sea as shown in Figure 4.14 (a) and (b) owing to the interaction between TLP and TAD. According to Liu et al. (1995), the second-order heave force on isolated TLP is lower when the incident wave is not from the head direction since the dominated free surface force term are lower. There is also modification of sum-frequency QTF in sway (Figure 4.14 (c) and (d)) and roll (Figure 4.14 (e) and (f)) direction. The sum-frequency QTF values in sway becomes slightly higher since the existence of the adjacent TAD. The QTF matrix distribution of sum-frequency moment in roll direction is changed more significantly. The peak value of QTF becomes higher and concentred at the diagonal line at $T_1 = T_2 \approx 8.5s$. The QTF values at $T_1 \neq T_2$ become lower. It is noted that the total sum-frequency velocity potential used for calculation of TLP sum-frequency force in the coupled TLP-TAD model can be divided into three components, i.e., the incident wave potential, diffraction potential by TLP and the diffraction potential by TAD. The combined velocity potential is no longer in the direction which is vertical to the columns' arrangement direction of TLP due to the additional diffraction potential by TAD. Consequently, the adjacent TAD has great impact on the sum-frequency heave, sway force and pitch moment on TLP by altering the total second-order sum-frequency velocity potential with additional potential by TAD.

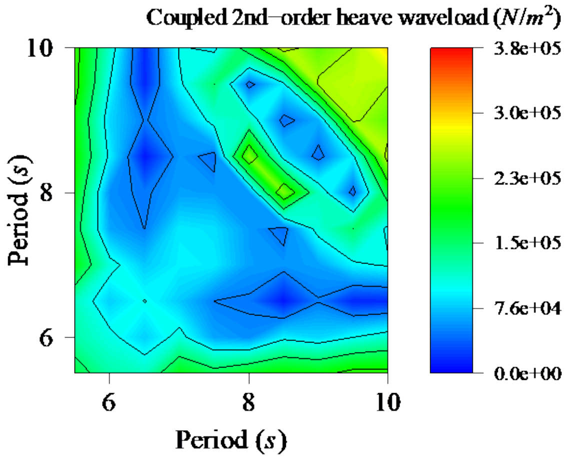

(a)

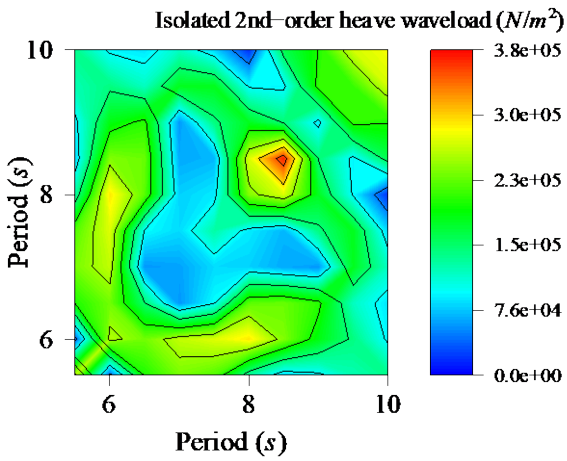

(b)

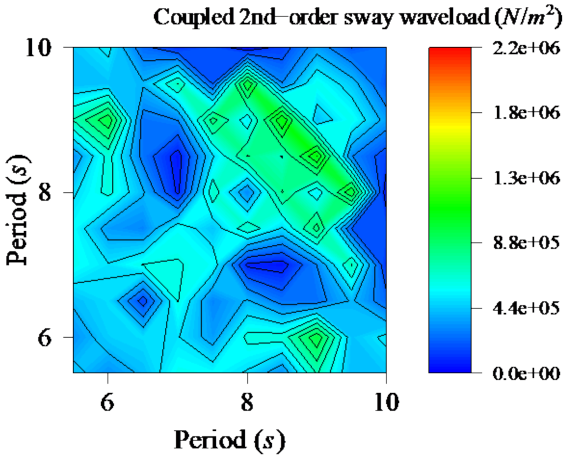
Coupled 2nd–order sway waveload (N/m^2)
Period (s)
Period (s)
10
8
6
6
8
10
2.2e+06
1.8e+06
1.3e+06
8.8e+05
4.4e+05
0.0e+00

(c)

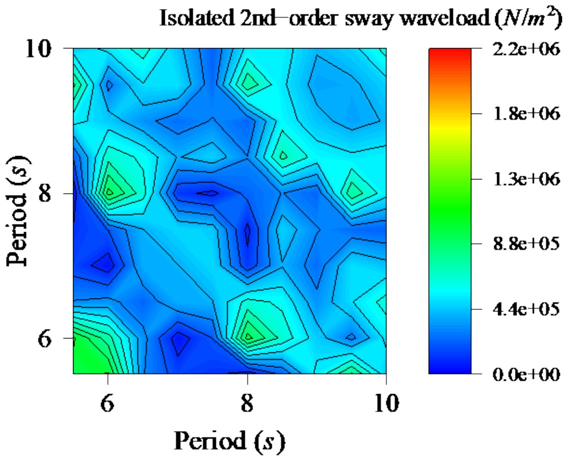
Isolated 2nd–order sway waveload (N/m^2)
Period (s)
Period (s)
10
8
6
6
8
10
2.2e+06
1.8e+06
1.3e+06
8.8e+05
4.4e+05
0.0e+00

(d)

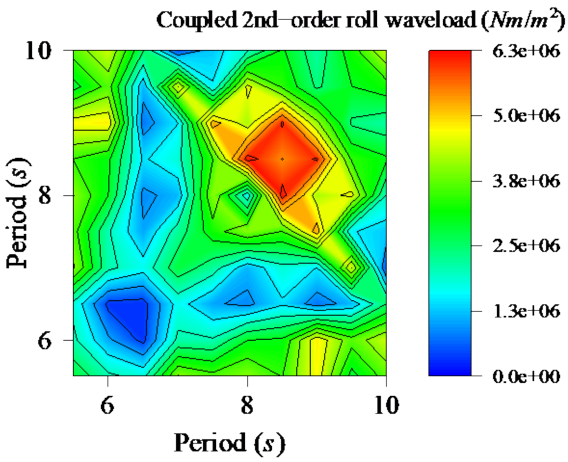
Coupled 2nd–order roll waveload (Nm/m^2)
Period (s)
Period (s)
10
8
6
6
8
10
6.3e+06
5.0e+06
3.8e+06
2.5e+06
1.3e+06
0.0e+00

(e)

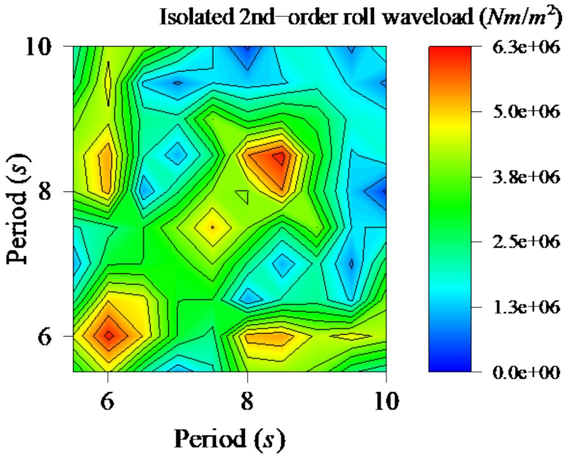

(f)

Figure 4.14 Sum-frequency QTF matrix of TLP under 90° incident wave. Heave wave load on TLP in (a) Coupled TLP-TAD model, and (b) Isolated TLP model. Sway wave load of TLP in (c) Coupled TLP-TAD model and (d) Isolated TLP model. Roll wave load of TLP in (e) Coupled TLP-TAD model and (f) Isolated TLP model.

The prediction of low-frequency wave load on floating platform is very important especially for semi-submersible like TAD. Full difference-frequency QTF matrix can be calculated using near-field integral or mid-field integral method. Since it is very time consuming to calculate the full QTF matrix, Newman approximation is often applied in engineering design for calculation of the wave drift load on TAD (Newman, 1974, Newman, 1985).

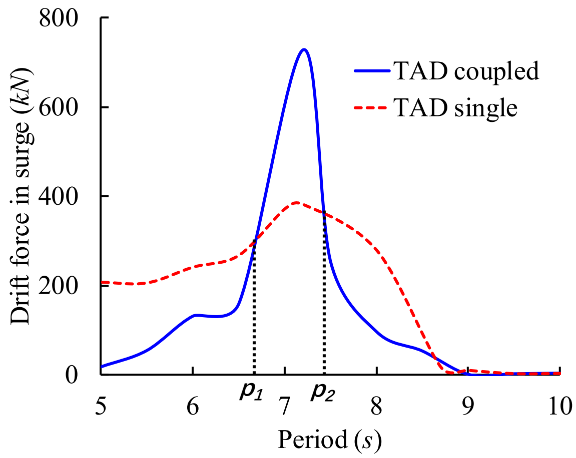

Figure 4.15 Surge different-frequency drift force on TAD under 0° incident wave in coupled TLP-TAD model

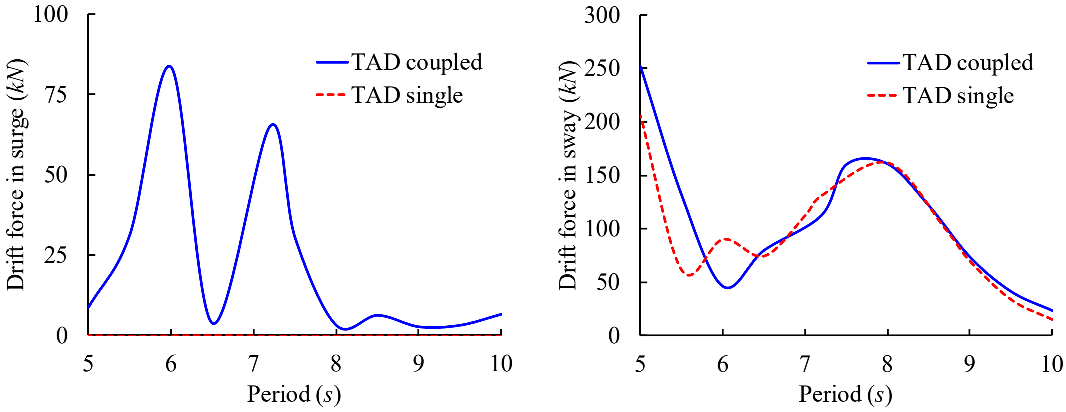

Figure 4.16 Different-frequency drift force on TAD under 90° incident wave in coupled TLP-TAD model and isolated TAD model

The surge wave drift load on TAD in coupled TLP-TAD model under 0° incident wave is shown in Figure 4.15. The wave load on TAD is influenced by interaction between the two adjacent bodies and shielding effect in coupled model. It is clearly seen in Figure 4.15 that, as the TAD is located at the lee position, the shielding effect makes the drift force on TAD in coupled model lower than that of TAD in isolation for wide range of period. However, Figure 4.15 also shows that the drift force on TAD is significantly higher in coupled model under the incident wave periods ranging between P1 to P2 and becomes lower after P2 indicating that the interaction between the two bodies amplifies the wave drift load on TAD. In fact, both shielding effect and interaction between TLP and TAD exists across the period range. Similar to the first-order surge force on TAD, the shielding effect is dominating when the wave period between 5s to P1 making the drift force on TAD in coupled model lower. However, the shielding effect decreases while the interaction increases with increasing wave period, and the competing effects on drift force on TAD in surge from the interaction and the shielding reach balance at P1, a crossing point, beyond that a rapid increasing trend of drift force in coupled model and overtaking that of isolated model. It is a clear indication that interaction is dominating factor to the drift force over shielding effect between P1 and P2. The drift force on TAD in coupled model is seen a rapid decrease after reaching its peak until the second crossing point P2, followed by shielding effect becomes dominating influence over the interaction between the two platforms.

To further demonstrate that the impact of interaction between two adjacent floating bodies on the drift force on TAD in coupled model, the beam sea condition is also selected in the investigation of wave drift load on TAD (Figure 4.16). Without shielding effect under 90° incident wave, Figure 4.16 shows that the wave drift force on TAD in surge direction for the coupled model is much larger than that in isolated model. However, the wave drift load on TAD in sway direction for both coupled model and isolated model are similar. The impact of interaction on wave drift load is much more significant in surge direction owing to the arrangement of TLP and TAD in surge direction.

4.6 Wave load on TLP and TAD under irregular wave condition in time domain

Wave load on coupled TLP-TAD model under EC1 and EC2 with 0° and 90° incident waves (head sea and beam sea condition) are further analysed in time domain. The parameters of the incident irregular waves have been described in Section 2. The surge and heave forces on TLP in coupled model under EC1 are shown in Figure 4.17, which are obtained by performing the fast Fourier transform of corresponding wave load time series. The first-order surge force on TLP in coupled model is slightly higher than that of isolated TLP model and the peak of sum-frequency wave force in surge direction on TLP in coupled model is nearly 3 times higher than the isolated TLP model (Figure 4.17 (a)). It indicates that the interaction between two platforms has impact on the surge wave load on TLP even it is in the upstream position of the configuration. The first-order heave forces are similar for both coupled model and isolated model (Figure 4.17 (b)). The existence of the TAD does not appear to have significant impact on the first-order heave force on TLP under the head sea condition and this is consistent to that demonstrated in Section 4.2.1 (see Figure 4.9 (b)). However, the sum-frequency heave forces on TLP in coupled model and isolated TLP model are different in Figure 4.17 (b). There is a peak point for the second-order force on TLP in coupled model at P1 in Figure 4.17 (b). This can be further examined using QTF matrix shown in Figure 4.12 (c). There is a peak of the second-order heave force for sum-frequency QTF in Figure 4.12 (c) at the diagonal line representing the double-frequency wave load ($T_1 = T_2 = 7.1$s) making the peak of sum-frequency force at $T = 3.57$s shown in Figure 4.17 (b).

In isolated model, there is no obvious peak of the sum-frequency force in Figure 4.17 (b). It is worth noting that the sum-frequency heave force is mainly contributed by the sum-frequency effect while $T_1 \neq T_2$ especially when T_1 = 6s to 9s and T_2 = 6s to 9s as shown in sum-frequency QTF matrix (Figure 4.12 (d)). Since the sum-frequency heave force at the area representing combination of wave components T_1 = 6s to 9s and T_2 = 6s to 9s are similar in QTF matrix, there is no significant peak of the sum-frequency heave force at the corresponding period from 3s to 4.5s in Figure 4.17 (b).

In the pitch direction, is should be noted that the existence of the TAD increase the first-order pitch moment on TLP around the period around 6s-8s. This is also obtained in Figure 4.9 (c). For the second-order pitch moment, the sum-frequency pitch moment in coupled model is more concreted at the T= 3.5s which is caused by the double-frequency $T_1 = T_2$ =7.1s. In the isolated model, second-order pitch moment is distributed from 3s to 4.5s since some of sum-frequency pitch moment is contributed by the sum-frequency effect while $T_1 \neq T_2$ especially when T_1 = 6s to 9s and T_2 = 6s to 9s as shown in sum-frequency QTF matrix (Figure 4.12 (f)).

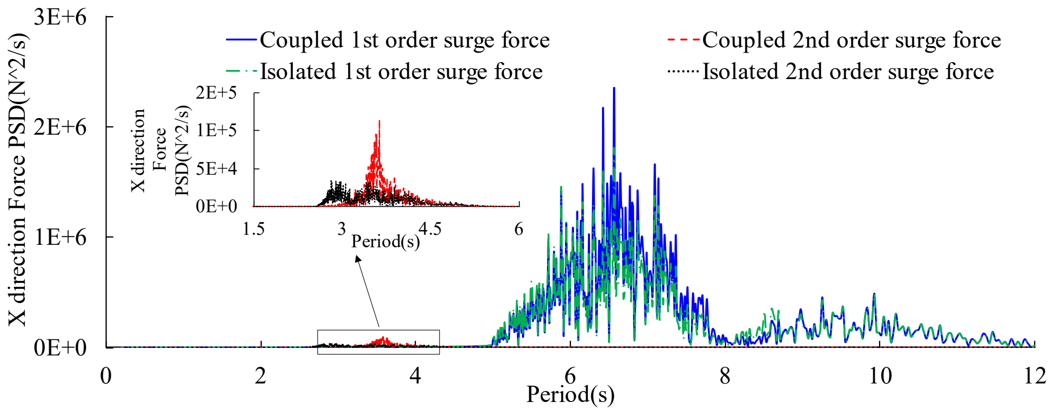

(a)

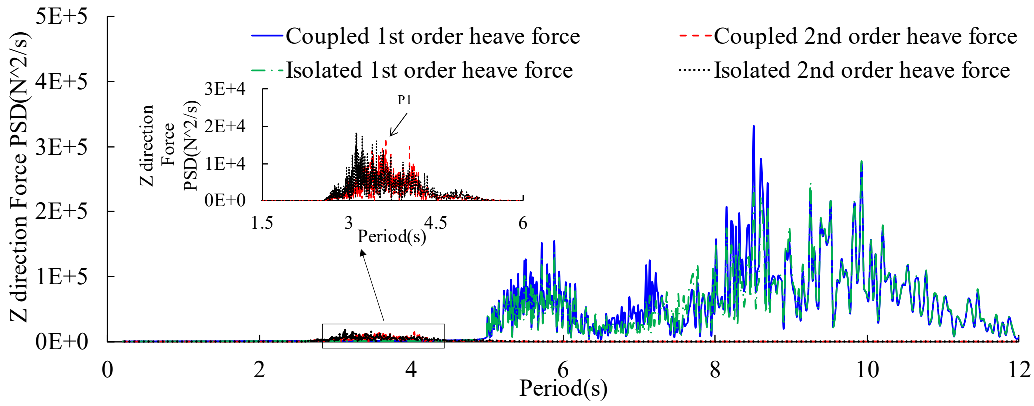

(b)

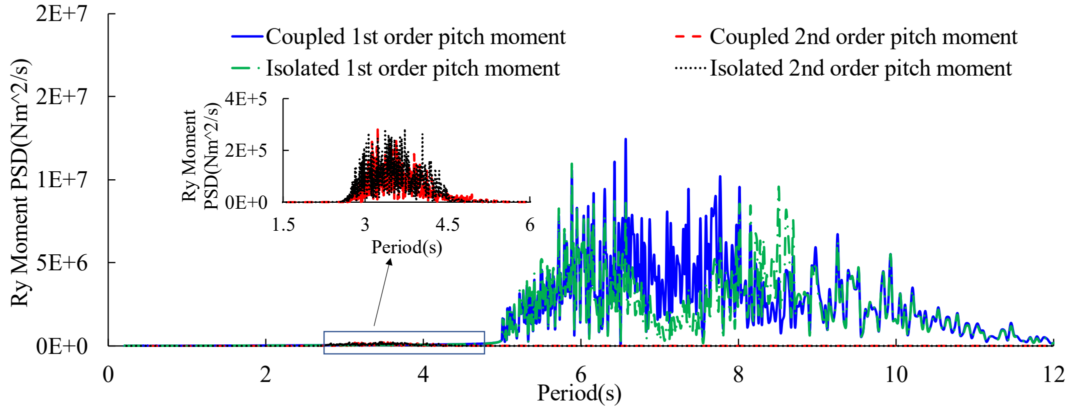

(c)

Figure 4.17 PSD (Power Spectral Density) of and the first-order and the second-order wave loads on TLP in coupled model and isolated TLP model under EC1: (a) surge; (b) heave; (c) pitch

Similar to TLP in coupled TLP-TAD model, the first-order wave force on TAD under EC1 in surge, heave and pitch direction are also calculated and shown in Figure 4.18 (a), (b) and (c) respectively. The wave forces on these directions in isolated model appear to be approximately 87% in surge, 32% in heave and 55% higher than those in coupled model for the period between 5s-6.5s. However, the first-order wave force (both surge force in Figure 4.18 (a), heave force in Figure 4.18 (b) and pitch moment in Figure 4.18 (c)) in coupled model and isolated model become similar with the increasing period (T>7s). These first-order wave forces calculated in time domain under the irregular wave condition also validate the characteristics of the wave load on TAD shown in Figure 4.10.

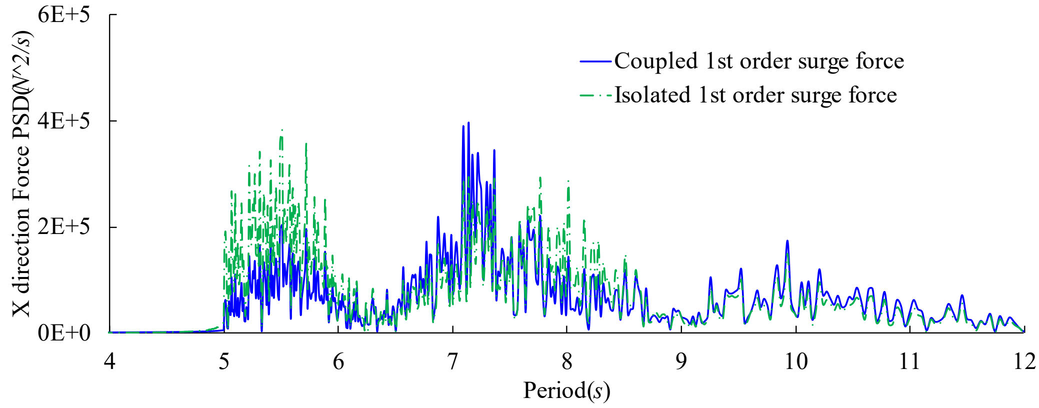

(a)

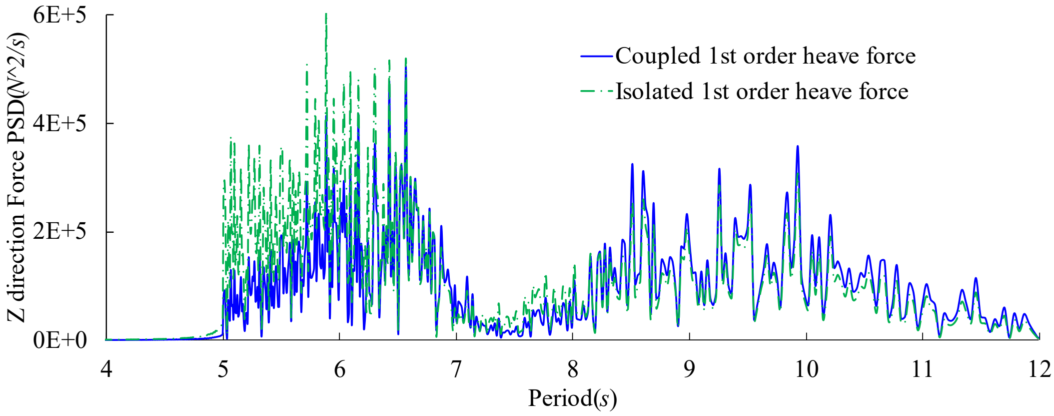

(b)

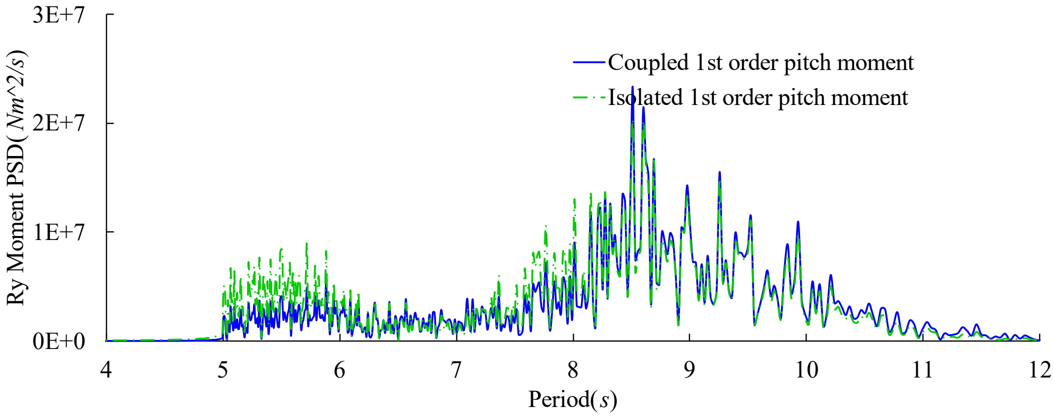

(c)

Figure 4.18 PSD (Power Spectral Density) of wave load on TAD in coupled model and isolated TAD model under EC1: (a) surge; (b) heave; (c) pitch

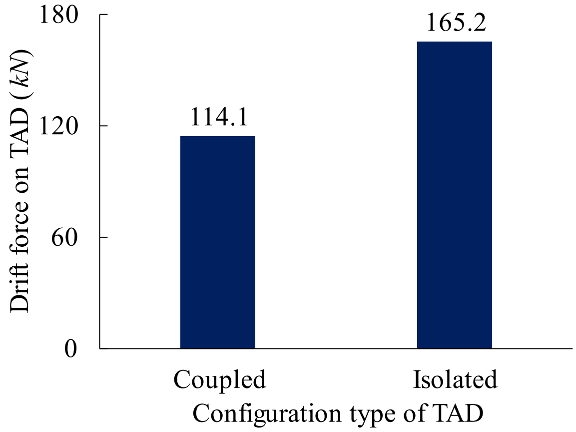

Figure 4.19 The mean value of the wave drift load (surge) on TAD in coupled model and isolated TAD model under 0° incident wave condition

Figure 4.19 shows that the mean value of drift force in surge direction on TAD in coupled model is lower than that in TAD in isolated model under the 0° irregular wave. For a wave spectrum with energy distribution of the incident wave around 5-10s under EC1, there are many wave components considered at different periods in Figure 4.19. The mean value of the surge drift force on TAD in coupled model under EC1 is lower indicating that shielding effect is still dominating under the irregular wave condition with consideration of all incident wave components.

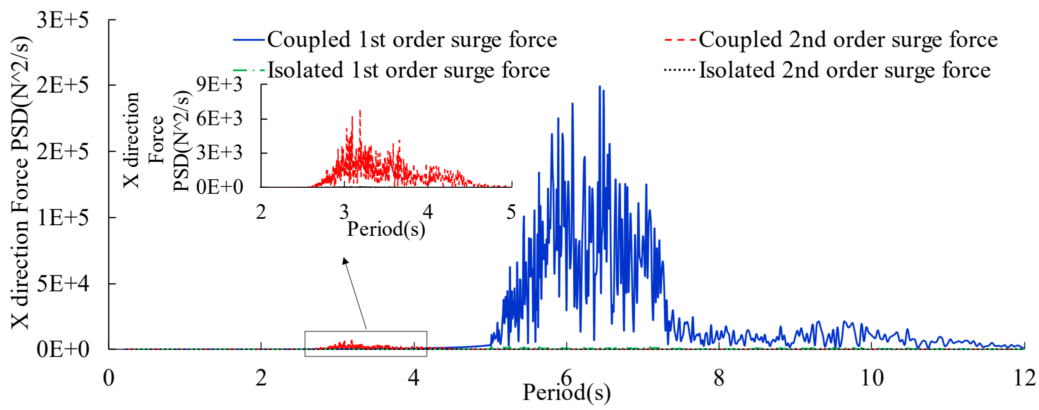

(a)

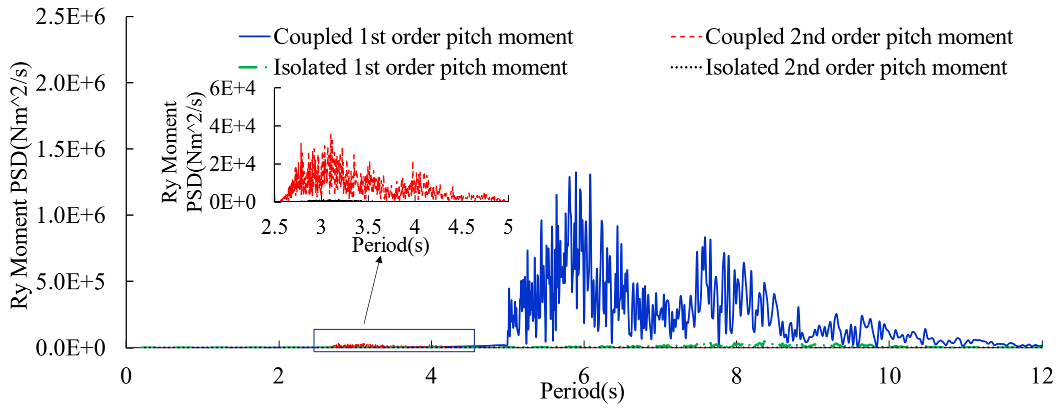

(b)

Figure 4.20 PSD (Power Spectral Density) of (a) surge force and (b) pitch moment on TLP in coupled model and isolated TLP model under beam sea

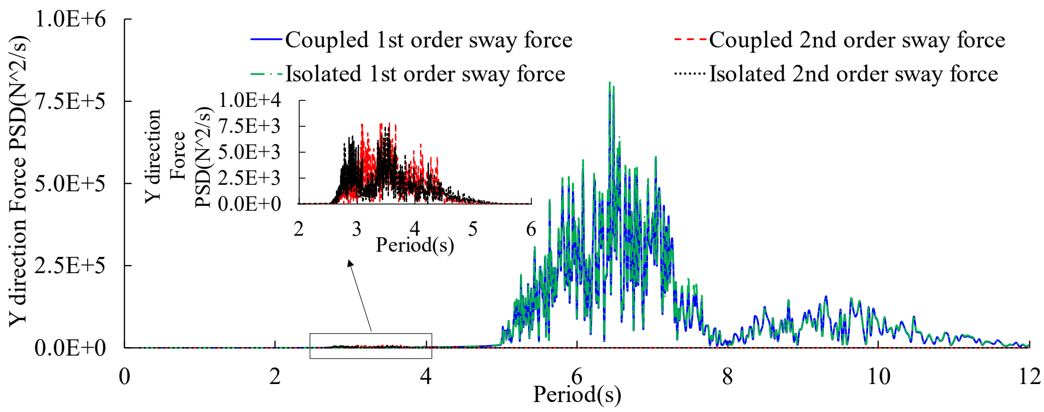

(a)

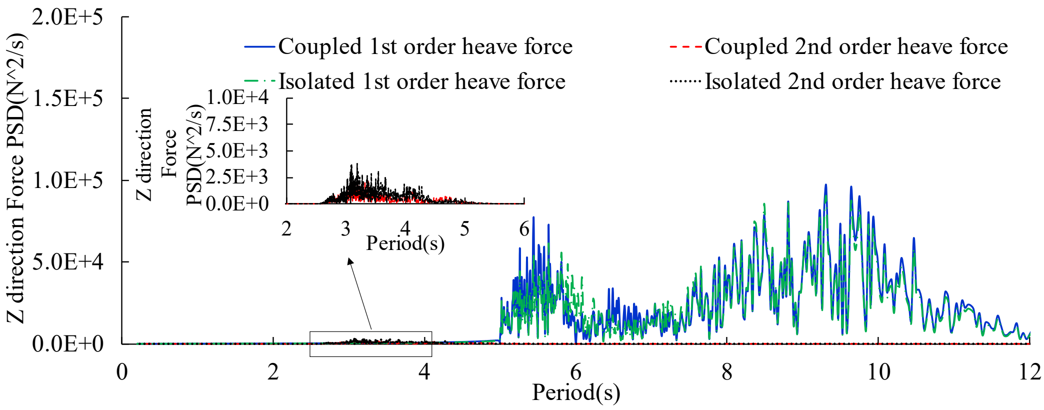

(b)

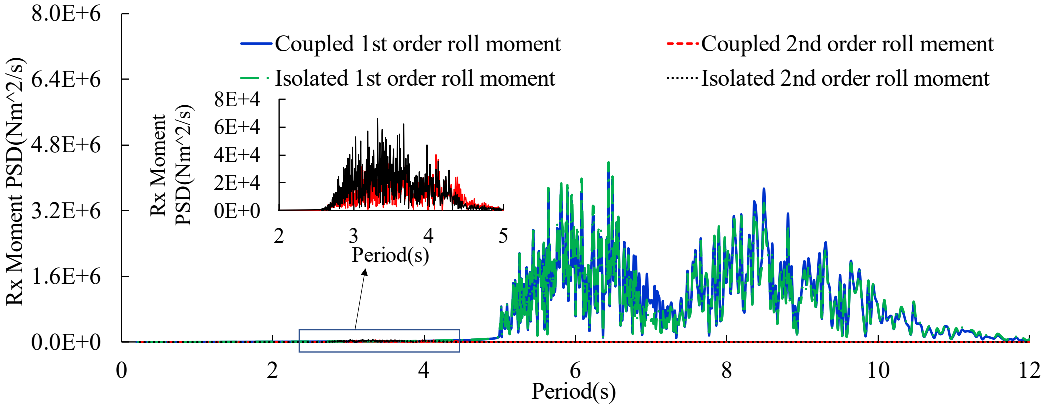

(c)

Figure 4.21 PSD (Power Spectral Density) of sway force (a), heave force (b) and roll moment on TLP in coupled model and isolated TLP model under beam sea

The surge force and pitch moment on TLP in both coupled and isolated model under the beam sea is shown in Figure 4.20. The sum-frequency and wave frequency surge load and pitch moment on isolated TLP model are significantly lower than that in the coupled model which is consistent to the features observed in Figure 4.11 and Figure 4.13 since the potential caused by adjacent platform is mainly passed along the arrangement direction (in the present study is surge direction). The first-order wave force and sum-frequency wave force on TLP in sway, heave and roll direction are shown in Figure 4.21. There is no significant difference between the first-order wave force on TLP in coupled model and the isolated model. However, the sum-frequency wave force on TLP in sway shows different distribution with increasing wave period in coupled model and the isolated model. The peak value of heave force due to sum-frequency in isolated model is about 45% higher than that in coupled model which is also observed in Figure 4.13 (c) and (d). The sum-frequency moment in roll on TLP in coupled is much lower than that in isolated model. This can be explained by the QTF matrix in coupled and isolated model. In isolated model, the highest value of QTF matrix occurs at the diagonal line $T_1 = T_2$ and the values at the other area that $T_1 \neq T_2$ are also very large. With the adjacent platform, the values in diagonal line of QTF matrix becomes slightly higher, but the values at area with $T_1 \neq T_2$ decrease significantly. Thus, the sum-frequency moment in roll on TLP in coupled model is lower than that in isolated TLP model since the incident wave in EC2 contains many components with different wave periods.

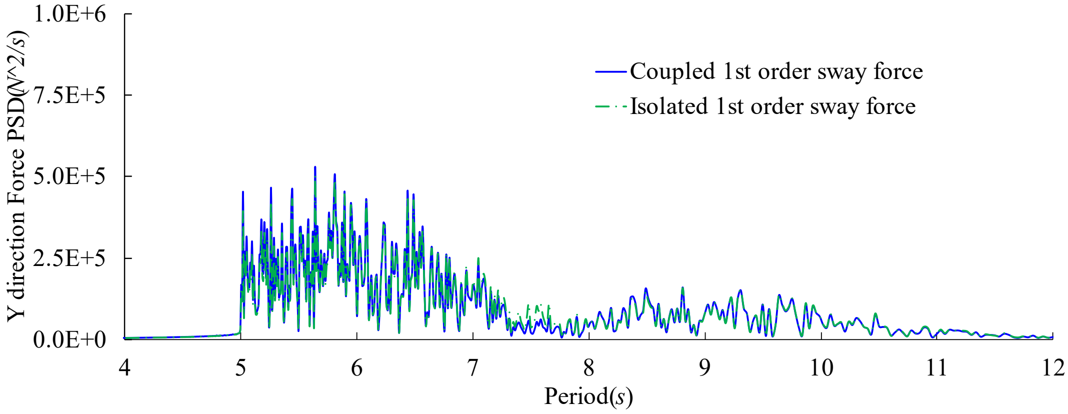

(a)

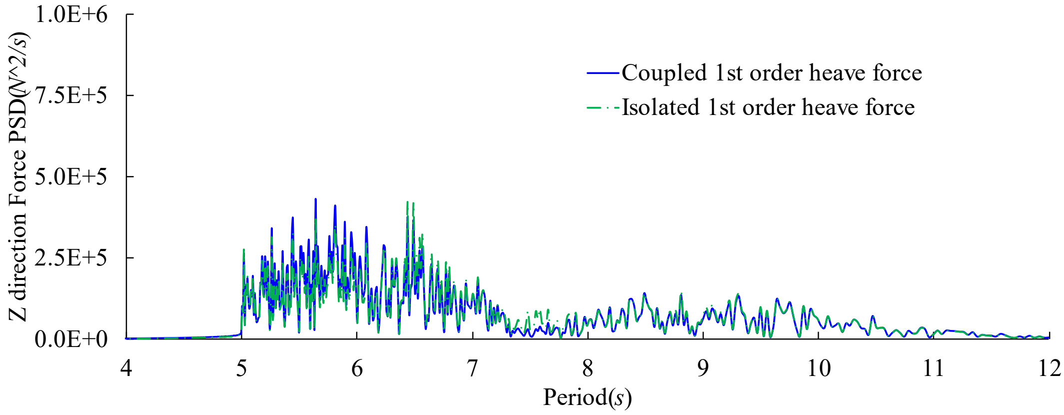

(b)

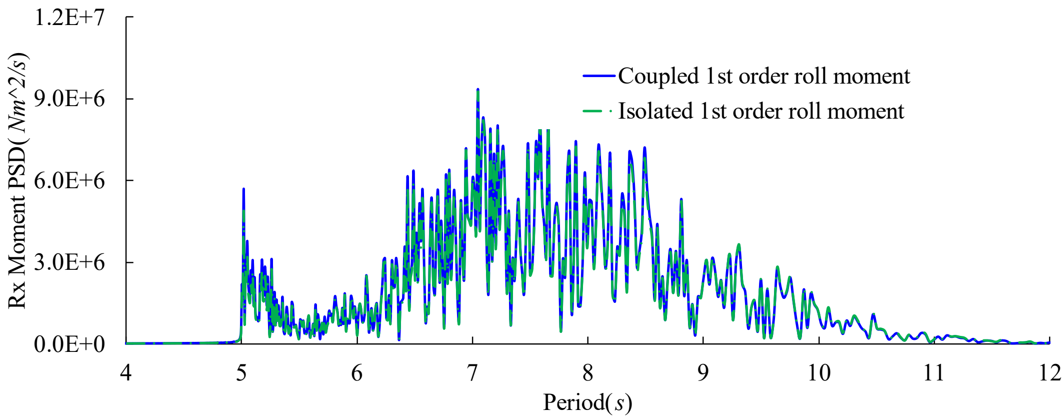

(c)

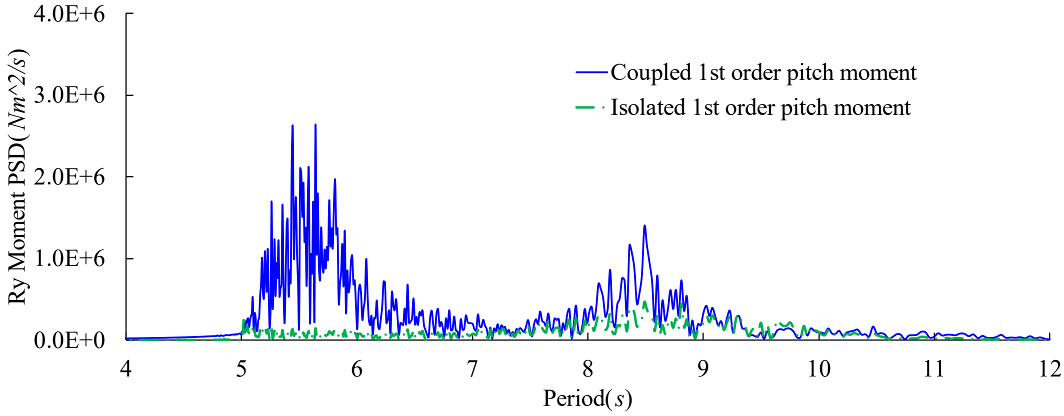

(d)

Figure 4.22 PSD (Power Spectral Density) of sway force (a), heave force (b), roll moment (c) and (d) pitch moment on TAD in coupled model and isolated TAD model under beam sea

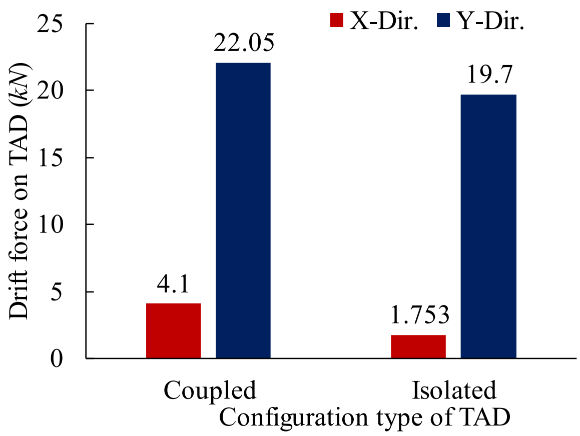

Figure 4.23 The mean value of the wave drift force in X-direction (surge) and Y-direction (sway) on TAD in coupled model and isolated TAD model under the beam sea

The sway and heave force on TAD in multi-platform coupled model and isolated model under the beam sea condition is shown in Figure 4.22. The wave frequency load on TAD in both models are similar which is a further validation to the features observed in Figure 4.11 (d), (f), (h) indicating that the interaction between two floating bodies in coupled model has little impact on the first-order wave force in sway, heave and roll direction. However, the pitch moment in coupled model is much larger than that in isolated model shown in Figure 4.22 (d) indication that the existence of adjacent platform provides an addition diffraction and radiation potential on TAD which is also validated in Figure 4.11 (j). The mean value of the wave drift load in surge and sway direction under the beam sea condition is shown in Figure 4.23 without shielding effect between the two bodies. The mean value of the wave drift load on TAD in sway direction is slightly higher (10.6%) in coupled model while the surge drift force in coupled model is more than twice of that in the isolated model. This indicates the interaction between two adjacent floating bodies in coupled model can increase the wave drift load in surge direction owing to the bodies are arranged in surge direction. This characteristic of wave force in platforms arrangement in coupled model should be considered in prediction of relative motion and practical design of the gangway between platforms.

4.7 Surface elevation around the multi-platform system

Two dominating hydrodynamic aspects are crucial in the design of floating offshore structures, namely surface elevation and wave loads. Thus, the surface elevation characteristics around the multi-platform system are investigated in this section. For the complex configuration of multiple platform system, wide range of incident wave parameter can impact on the hydrodynamic of the system. Thus, five incident wave directions from 0° to 180°, and four wave periods are considered in the investigation. The detailed wave conditions are listed in Table 4.17. The maximum total surface amplitude η, which can be expressed as:

$$\eta = MAX\ Re\{\eta^{(1)} e^{-i\omega t} + \eta^{(2)} e^{-i2\omega t} + \bar{\eta}\} \tag{4.1}$$

where $\eta^{(1)}$, $\eta^{(2)}$ and $\bar{\eta}$ are time-independent surface elevation which is discussed in Section 2.6 and 2.7. The radiation wave is included since the radiation potential is considered in total potential in the calculation of surface elevation.

Table 4.17 Wave conditions applied in modelling surface elevation characteristics around multi-platform system

No.	Period(s)	Frequency(rad/s)	Direction
1	15.7s	0.400	

2	12.0s	0.523	0°, 45°, 90°,
3	8.5s	0.739	135°, 180°
4	6.6s	0.951	

The surface elevation for the 0° incident wave is plotted in Figure 4.24. With different incident wave periods, the water field around the multi-platform system is very different. Under the long incident wave periods (see Figure 4.24 (a) and (b)), the surface elevations under the decks of both platforms are higher than those of other areas. The surface elevation under the deck of the two platforms is the combination of the incident wave, scattered wave, and radiated wave. Since the incident wavelength is large, the diffraction caused by structures is not strong as shown in Figure 4.24 (a) and (b). The surface elevation around the multi-platform system becomes higher and the peak surface elevation is captured around locations between columns #1&#3, A&B and D&E in Figure 4.24 (c). The peak occurs at the upstream position of the whole system near the column #1 and #3. Since the incident wavelength becomes shorter, the diffraction becomes stronger than that in Figure 4.24 (a) and (b) making the peak surface elevation occur at the upstream position. It is noted that there are also peaks of surface elevation occurring at the space between column A&B and column D&E in Figure 4.24 (c) because of the reflection wave caused by the flat part of the TAD columns. There is a peak surface elevation between the downstream columns (#2 and #4) of TLP as the incident wave period t = 6.6s (Figure 4.24 (d)) since the existence of the adjacent TAD. There is also a peak surface elevation occurring between column A and column C of TAD caused by the adjacent TLP. Since the space between column A and column C of TAD are narrower than TLP's columns, the wave diffracted by TLP becomes more difficult to pass the columns of TAD and causes strong diffraction and reflection leading to the peak surface elevation between column A and column C. It indicates that the hydrodynamic interaction caused by the external platform will amplify the surface elevation in the multi-platform system. It should be noticed that this feature of peak surface elevation can potentially cause damage to the bridge between platforms.

The maximum surface elevation around the multi-platform system under 45° incident wave is shown in Figure 4.25. The surface elevation amplitude is seen with slight increase when the incident wave period is large since the weak diffraction caused by the incident wave with longer wavelength in Figure 4.25 (a) and (b). The surface elevation at column 2 of TLP and the space between columns A and B of TAD is slightly higher than other positions at incident wave period t=8.5s (Figure 4.25(c)) which is mainly due to the hydrodynamic interaction between TLP and TAD. There are higher peaks of surface elevation near columns #3 and #4 when the incident wave period is 6.6s (Figure 4.25 (d)). Since column #4 is near the TAD and influenced by the TAD more significantly, which is also validated the surface elevation's amplification caused by the hydrodynamic interaction. Column #3 is located at upstream position when the incident wave from 45° as shown in Figure 4.1. There is a peak surface elevation at column #3 of TLP. Since column #4 near the adjacent TAD leading to that the surface elevation around the column #4 being influenced by the TAD, there is a peak surface elevation observed around column #4 in Figure 4.25 (d). Both peaks of surface elevation positions are not facing incident wave directly because of the diffracted and radiated wave caused by the adjacent TAD. The diffraction and radiation of TAD has altered the surface elevation around the TLP in terms of both the value and locations of the peak surface elevation which is clearly no longer symmetric. This is also a demonstration that the interaction between the two adjacent structures in the multi-platform system needs to be taken into consideration in the air gap design and surface elevation prediction.

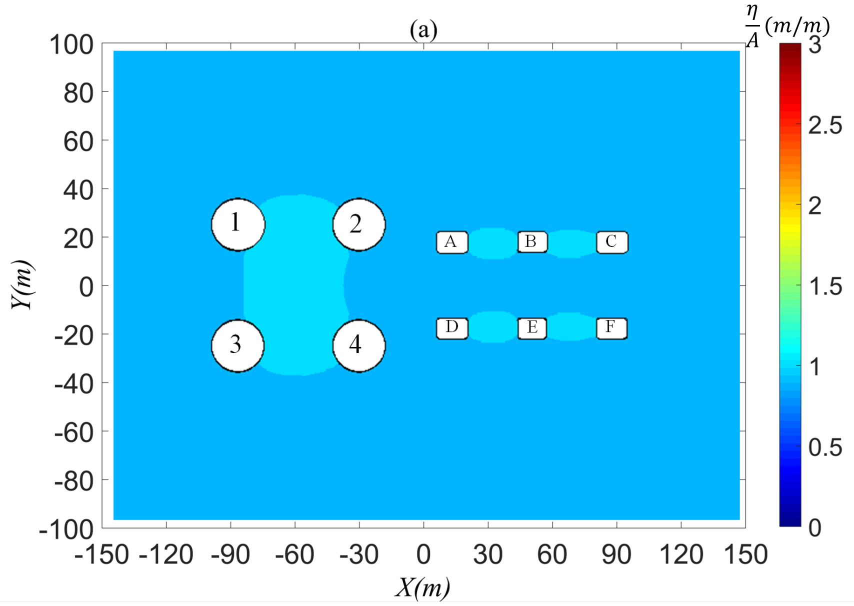

(a) Incident wave period t = 15.7 s

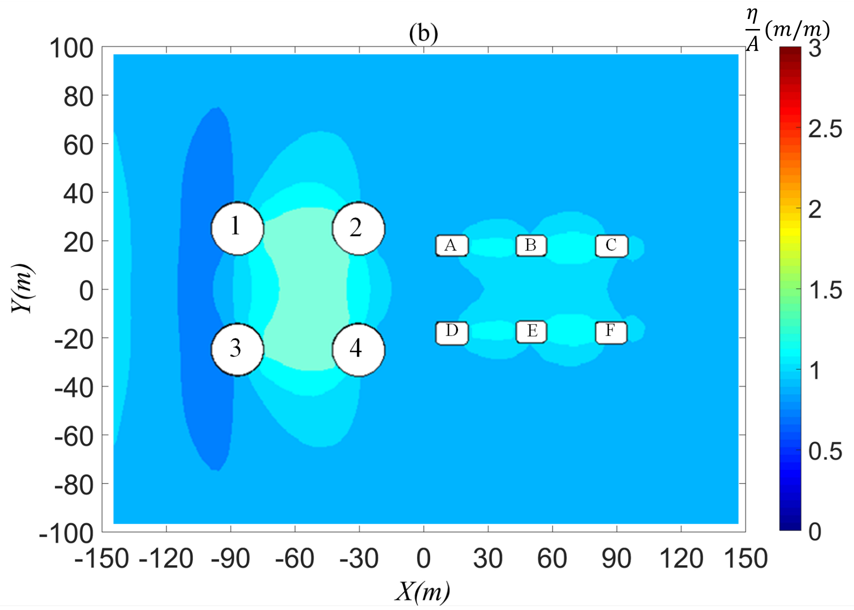

(b) Incident wave period t = 12.0 s

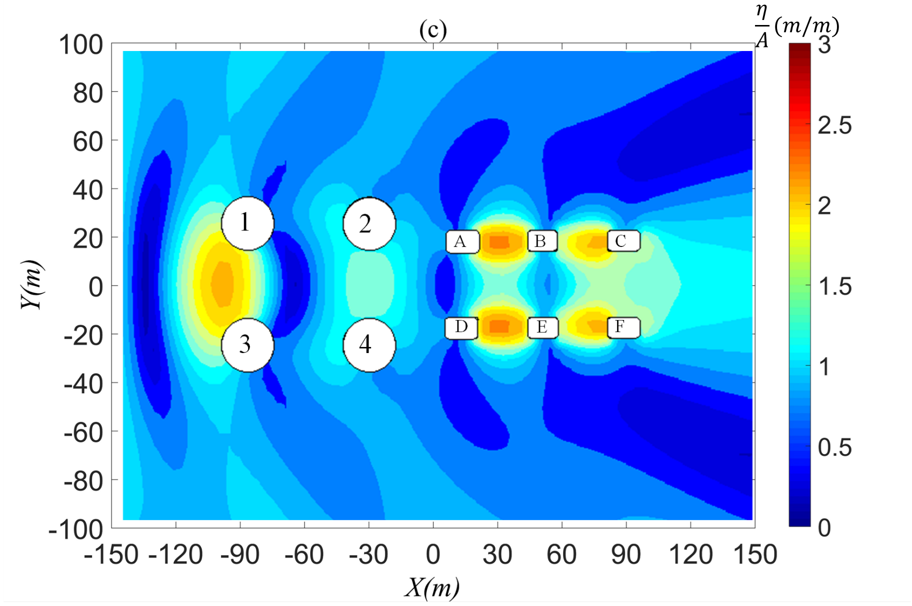

(c) Incident wave period t = 8.5 s

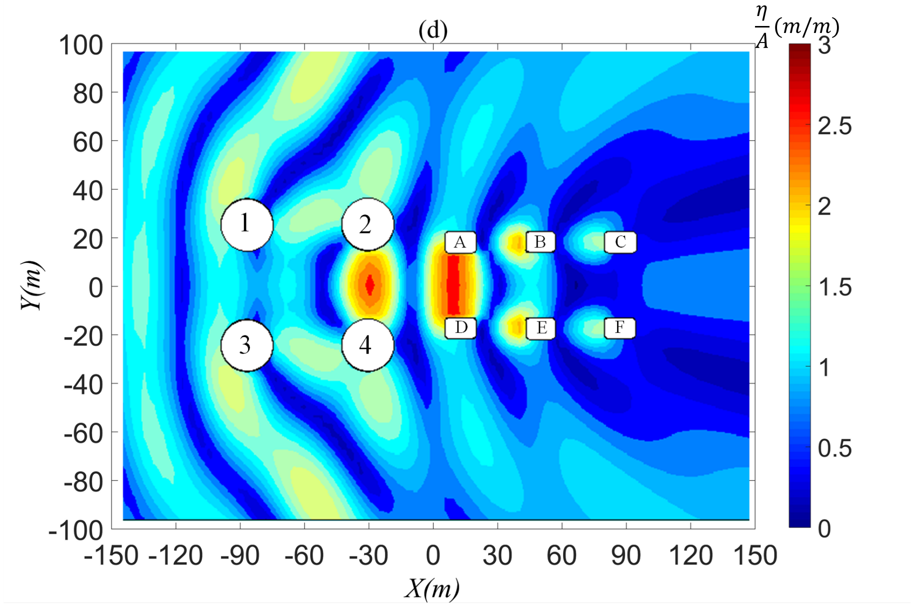

(d) Incident wave period t = 6.6 s

Figure 4.24 Maximum surface elevation (m) around coupled TLP-TAD platform system under 0° incident wave with 1m amplitude.

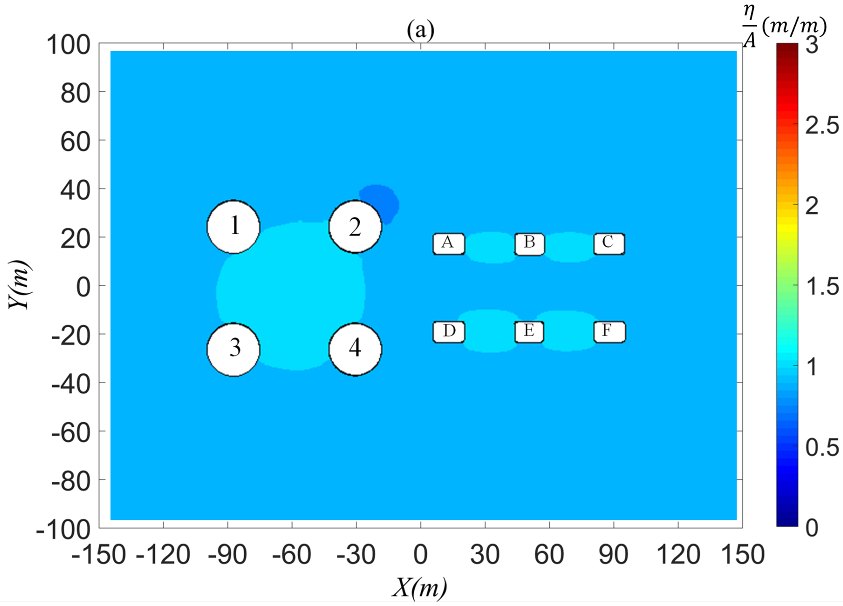

(a) Incident wave period t = 15.7 s

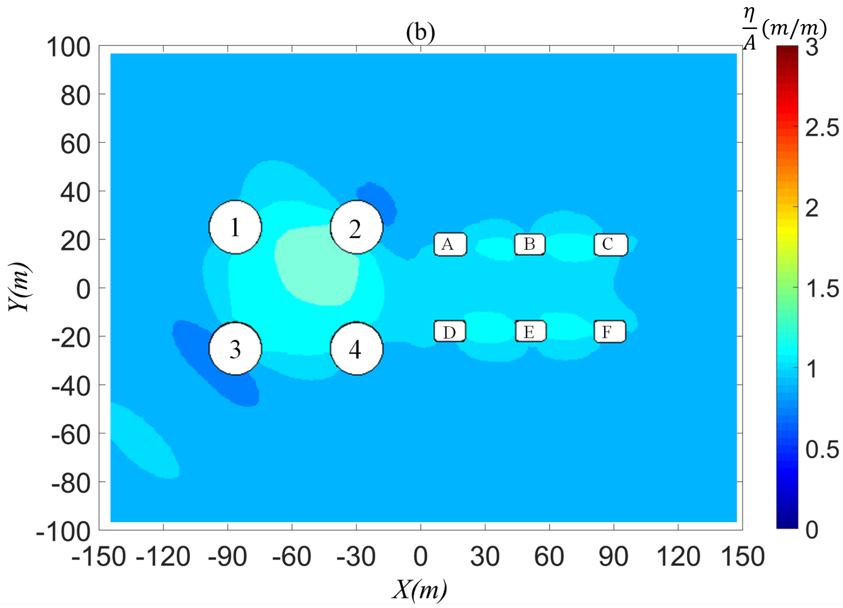

(b) Incident wave period t = 12.0 s

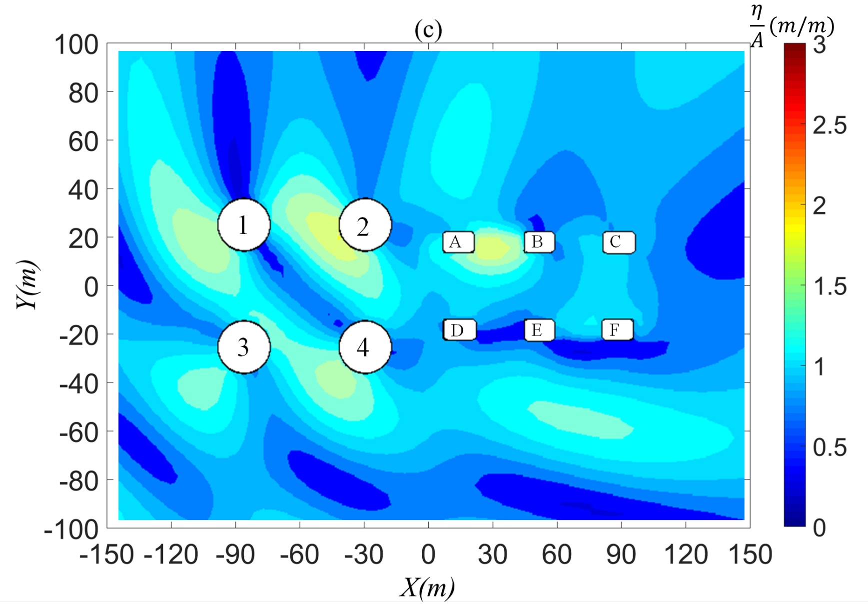

(c) Incident wave period t = 8.5 s

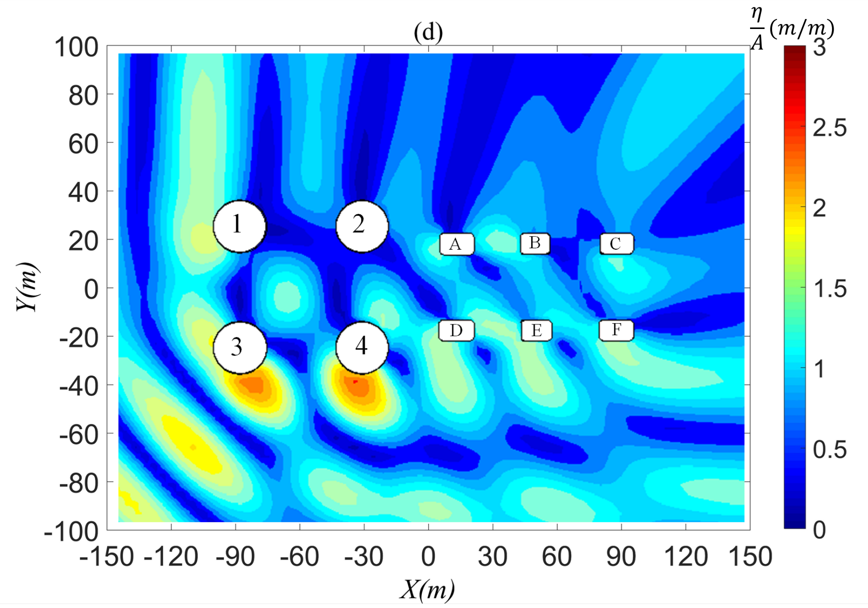

(d) Incident wave period t = 6.6 s

Figure 4.25 Maximum surface elevation (m) around coupled TLP-TAD platform system under 45° incident wave with 1m amplitude.

In Figure 4.26 and Figure 4.27, the incident wave direction is 90° and 135° respectively. When the incident wave direction is 90°, Figure 4.26 shows that the impact of the hydrodynamic interaction on the surface elevation is not significant for incident waves with relatively longer wave periods as shown in Figure 4.26 (a), (b) and (c). However, with the shorter period incident wave t = 6.6s (Figure 4.26 (d)), the diffraction becomes stronger making the peak surface elevation occur near column D and space between column E and F of TAD. Since the existence of TLP, the diffracted and radiated wave caused by TLP are combined with the wave around TAD leading to the peaks of surface elevation. Additionally, the flat part of the columns of TAD also strengthens the reflection of waves generating the peak surface elevation between columns. When the incident wave is from 135° direction (see Figure 4.27), the peak surface elevation between the two platforms is hardly observed. When the incident wave period is 8.5 s as shown in Figure 4.27 (c), there are two peaks surface elevation at the space between column B and C, and D and E of TAD. However, the amplitude of peak surface elevation is not large since the weak diffraction caused by the columns of TAD. When the incident wave period is 6.6 s (see Figure 4.27 (d)), the peaks of surface elevation occur at columns #4, E and F. The amplitude of peaks is much higher than that under 8.5 s incident wave since shorter incident wavelength caused stronger diffraction and the flat part of columns of TAD. Due to the existence of TAD, the position of the peak surface elevation near column #4 of TLP is influenced by the diffracted wave and radiated wave caused by TAD moving significantly towards column #3 of TLP.

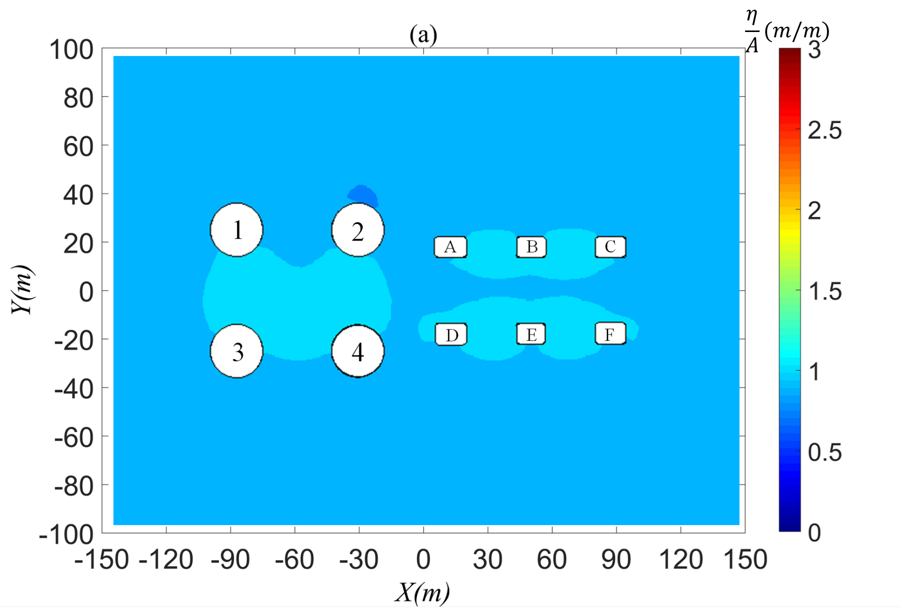

(a) Incident wave period t = 15.7 s

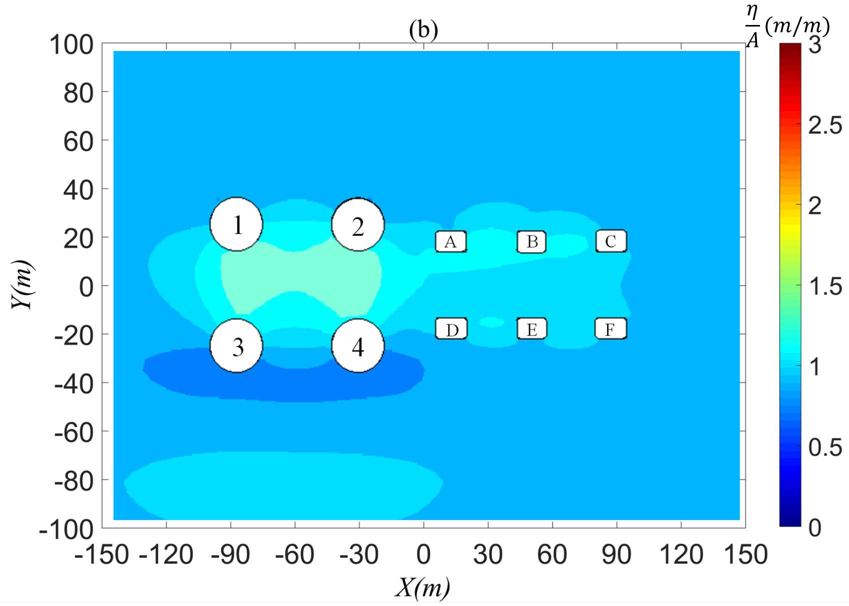

(b) Incident wave period t = 12.0 s

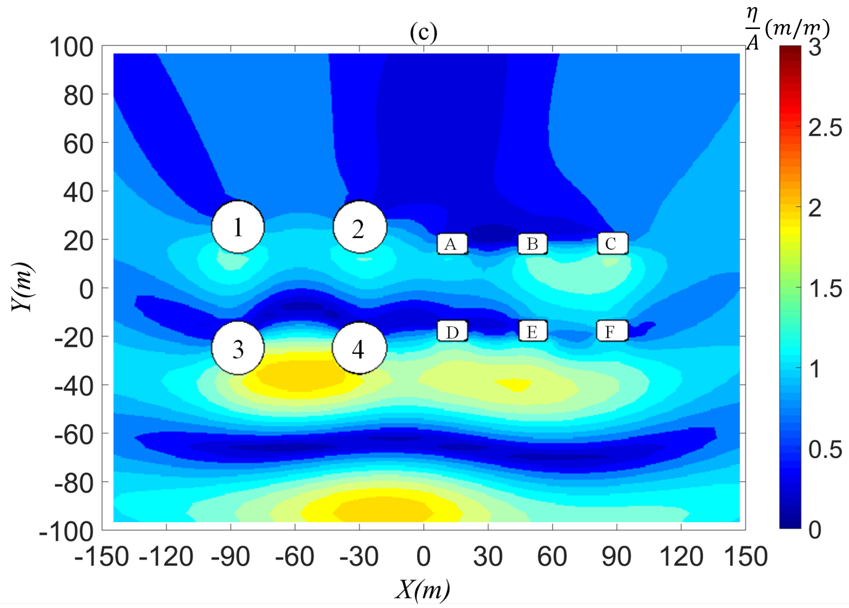

(c) Incident wave period t = 8.5 s

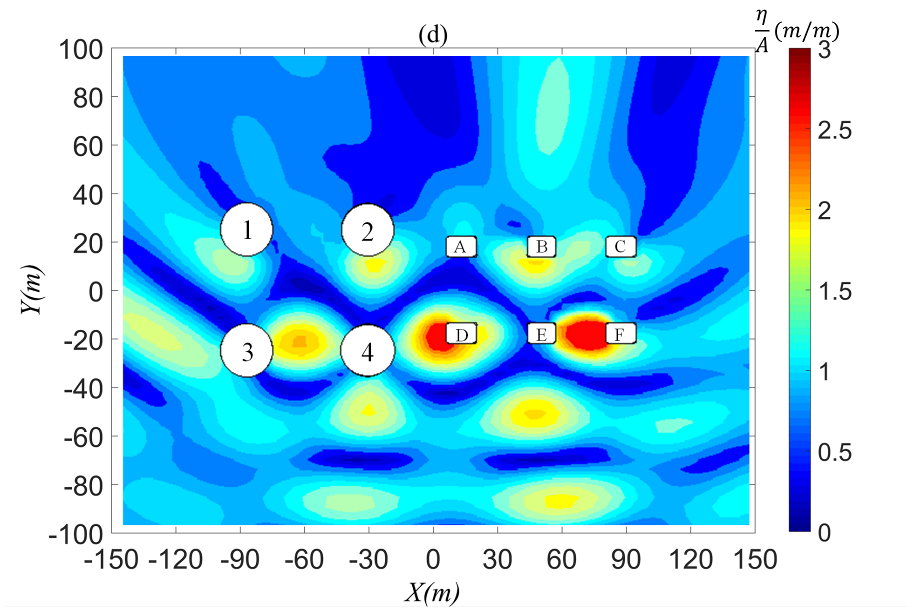

(d) Incident wave period t = 6.6 s

Figure 4.26 Maximum surface elevation (m) around coupled TLP-TAD platform system under 90° incident wave with 1m amplitude.

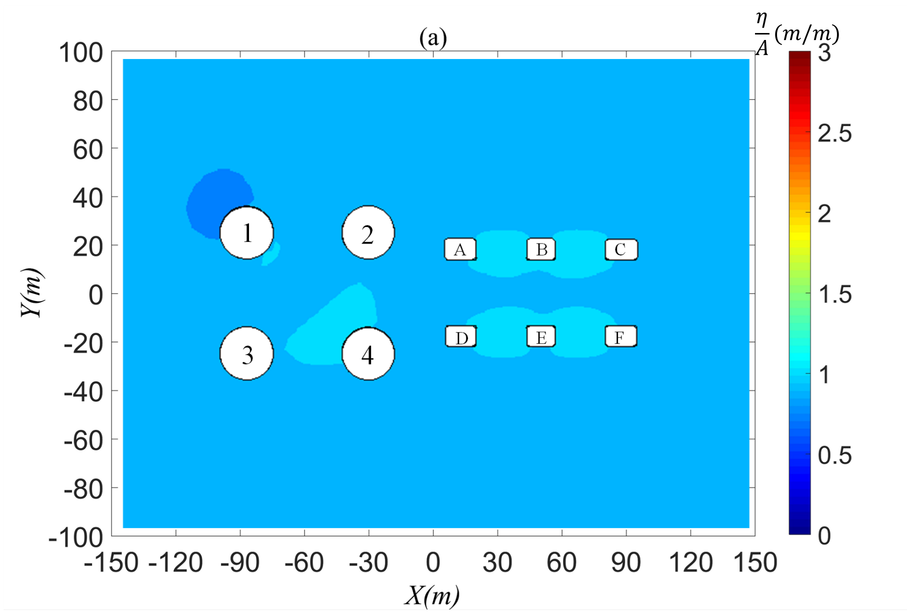

(a) Incident wave period t = 15.7 s

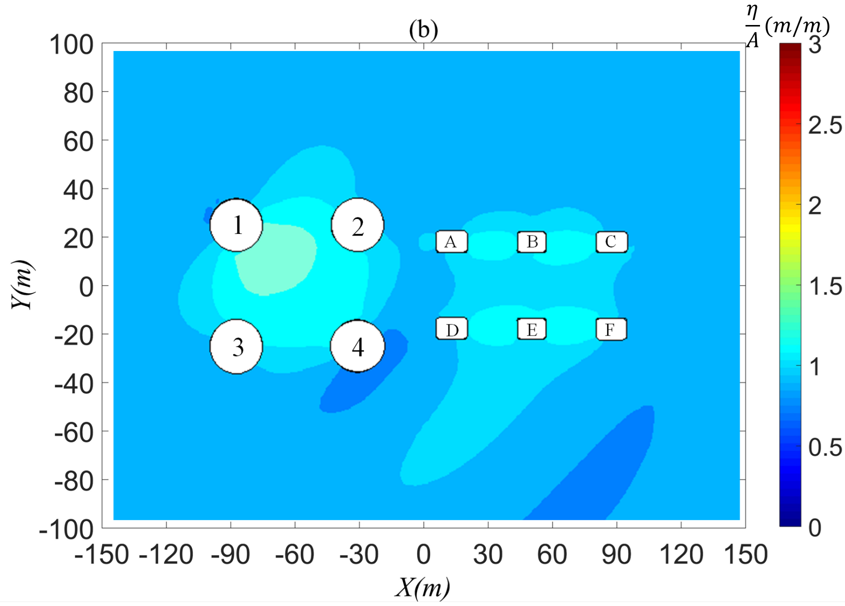

(b) Incident wave period t = 12.0 s

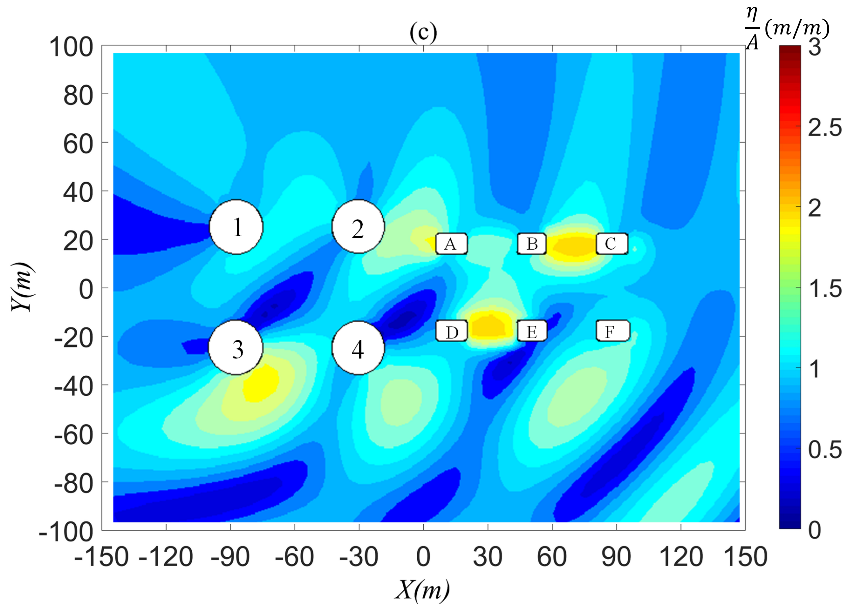

(c) Incident wave period t = 8.5 s

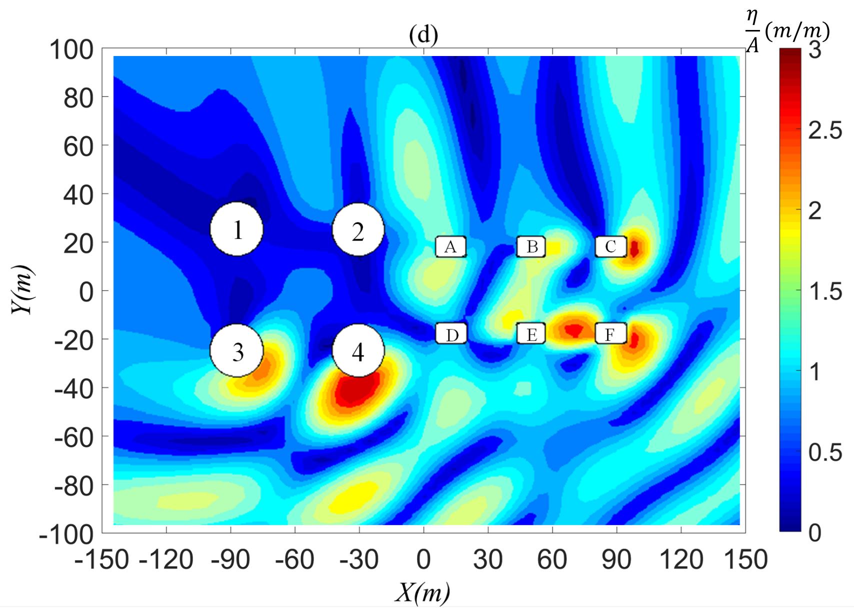

(d) Incident wave period t = 6.6 s

Figure 4.27 Maximum surface elevation (m) around TLP-TAD platform system under 135° incident wave with 1m amplitude.

When the incident wave is set to 180° (from the positive of the *x*-axis) as plotted in Figure 4.28, the TAD is at the upstream position. Under the long incident wave period (see Figure 4.28 (a) and (b)), there is no significant peak surface elevation under the deck of the TLP and the TAD in the multi-platform system since the long incident wavelength. When the incident wave is 8.5 s (see Figure 4.28 (c)), the impact of hydrodynamic interaction between two platforms on the surface elevation becomes more significant, leading to the peaks surface elevation formed between two platforms and the peaks at the space between columns A and B and space between columns D and E. However, when the incident wave period decreases further to 6.6 s (Figure 4.28 (d)), there is not distinct peak surface elevation can be observed between the two platforms. However, there is an obvious peak surface elevation near columns C and F, which are the upstream columns of the TAD since there is a strong shielding effect caused by TAD at the 6.6s' incident wave.

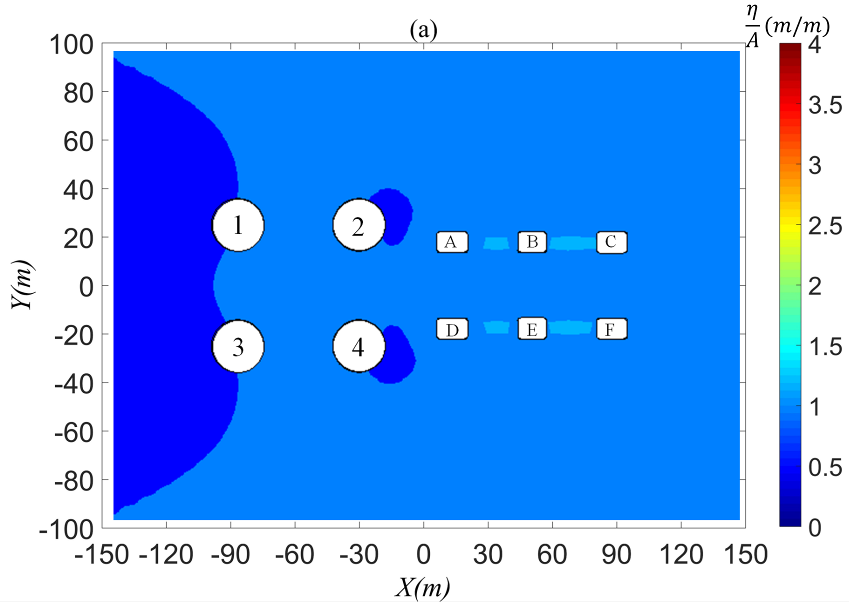

(a) Incident wave period t = 15.7 s

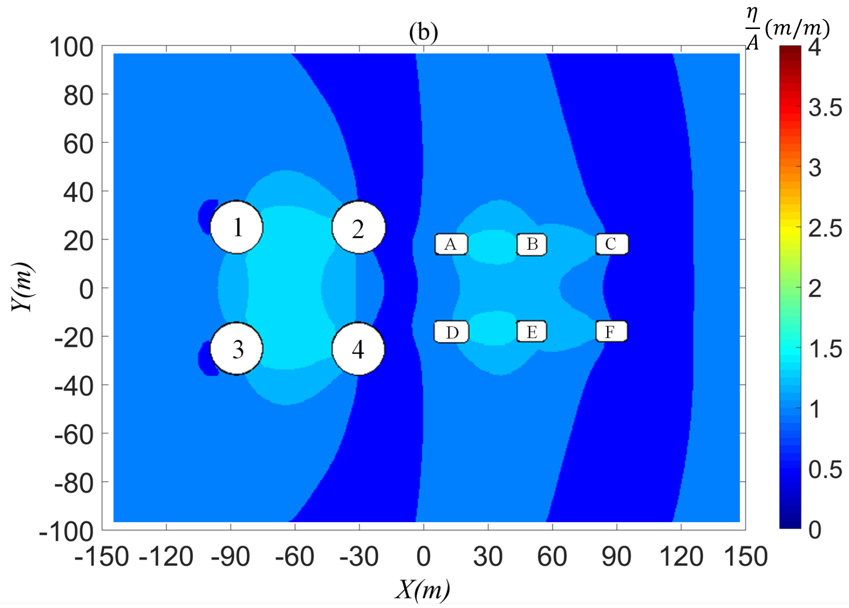

(b) Incident wave period t = 12.0 s

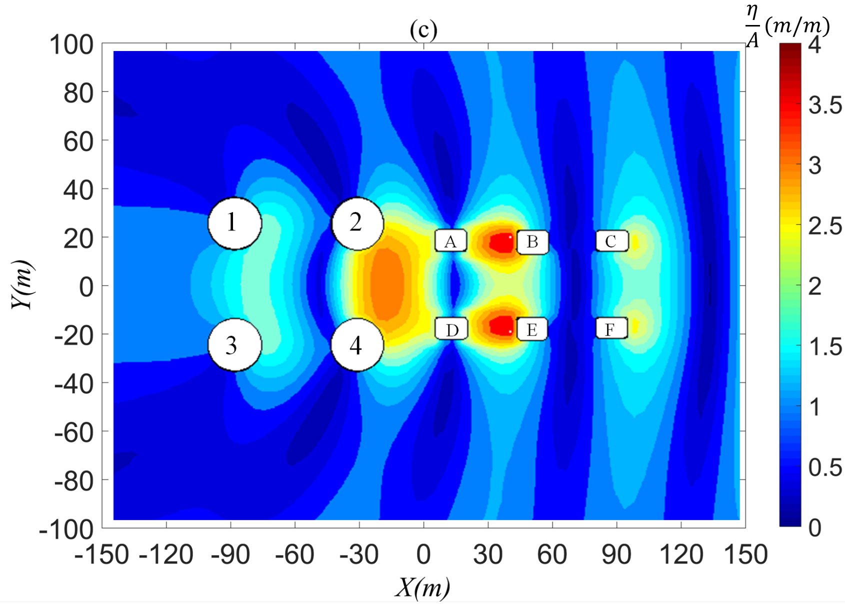

(c) Incident wave period $t = 8.5$ s

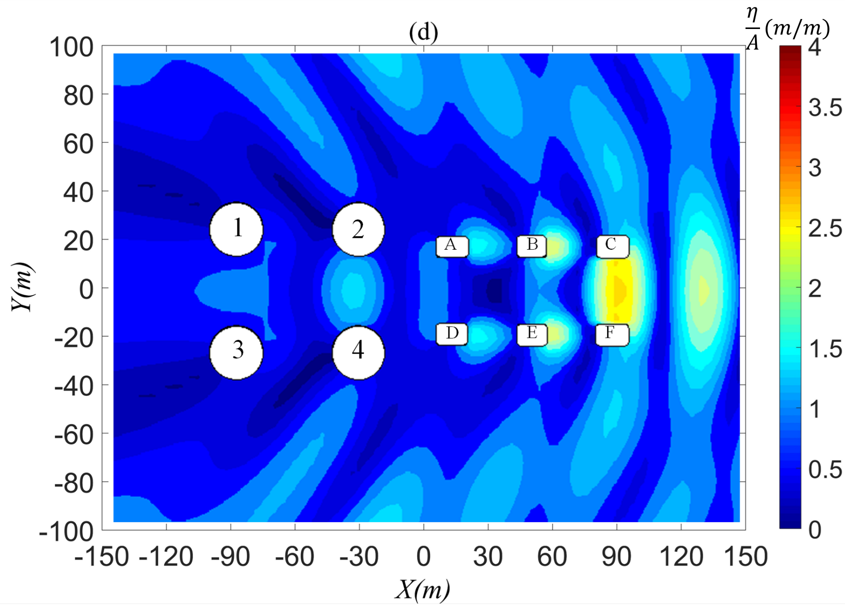

(d) Incident wave period $t = 6.6$ s

Figure 4.28 Maximum surface elevation (m) around coupled TLP-TAD platform system under 180° incident wave with 1m amplitude.

4.8 Summary

The coupled TLP-TAD platform system under incident waves of different wave properties and directions are investigated based on numerical simulation. The numerical model is rigorously validated with the experiment results. The global motion response of the multi-body system and the wave force on platforms are examined in detail. Both frequency and time domain approaches are adopted in numerical simulation to consider the effect of hydrodynamic interaction between two bodies and nonlinear effects. Based on the present numerical study, the main conclusions are as follow:

- The interaction between two adjacent floating bodies increases both the first-order and the second-order wave force on the two bodies along their arrangement direction in multi-body system. For the structure at the lee position, both shielding effect and the interaction between the two bodies have great impact on the wave force. This should be taken into the consideration in the prediction of the relative motion and design of the gangway between platforms.

- Under the beam sea condition, the wave loads in surge direction (which is transverse to the incident wave) on TLP/TAD in coupled model cannot be neglected since the diffraction and radiation in surge direction caused by adjacent platform. This should be considered in the gangway design between two platforms.

- The influence of interaction between the two bodies on TLP's sum-frequency heave force in multi-body system is highly dependent on the wave direction. The peak value of sum-frequency QTF matrix in coupled model under head wave is much higher than that of isolated TLP model. The sum-frequency QTF matrix under the beam sea in coupled model is lower than that of isolated TLP model. This characteristics of sum-frequency in heave is a crucial design feature to avoid the significant nonlinear (high-frequency "springing" and "ringing") wave load which often induces TLP undergoing resonant motion in vertical planes and further leads to fatigue load to tendons and risers in TLP-TAD coupled model.

- The drift force on TAD in surge are increased by the interaction between the two floating bodies. Meanwhile, the shielding effect is also existing across period in head sea condition. The combination of these two effects may lead the drift force on TAD much higher in some range of wave period and leads the top tension of mooring lines of TAD increase suddenly.

- The diffraction and radiation of the platforms in the multi-body platforms system is considered in the simulation of the free surface around the two platforms system. The impact on the surface elevation around multi-body platforms due to the existence of the other adjacent platform is taken into consideration. Due to the interaction between two platforms contained in the system, the peak surface elevation can occur at the space between two platforms. This indicates that the surface elevation should be simulated with the existence of the other adjacent platform when it comes to the air gap design for the multi-body platforms system.

5 Interaction of Offshore Support vessel with adjacent offshore wind turbine during maintenance operation

5.1 Operation and maintenance of offshore wind farms using offshore support vessel

With the rapid development of the renewable energy, offshore wind farms attracted much attention due to abundant wind resource in the ocean. The percentage of the wind energy increase rapidly in the last decade. By the end of 2020, the fixed offshore wind power capacity has reached 28000MW and the floating offshore wind power has reached the 82MW (Selot et al., 2019). The first offshore wind farm is the Vindeby wind farm which is established in Denmark in 1991 (Feng and Shen, 2015) and decommissioned in 2017 (Technology, 2017). The Vindeby wind farm is installed along the coast and its water depth is only 4m. However, there are vast sites suitable for wind farms far from the coast. The wind farms are moving far off the coast since there is more abundant wind source. The first commercial floating wind turbine Hywind Scotland is located at 18 miles from the coast of Peterhead, Scotland. Due to the water depth of the wind farm position is more than 100 meters, the fixed wind turbine is no longer suitable. A 5MW floating offshore wind turbine (FOWT) is employed in the Hywind project. According to the European Energy (2020), there are another six offshore floating wind turbine projects will be completed before 2023. The design life of the offshore wind turbines are usually 25-35 years. By increasing number of wind turbines being installed in the sea, there is a significant demand for offshore support vessels to carry out the necessary and regular maintenance and inspection tasks required for the safe operation of offshore wind farms. Vessel based inspection systems are used by most operators for regular inspections and maintenance regarding scour, corrosion, weld, and structural inspections.

The Operation and Maintenance (O&M) costs are significant part of the overall lift-cycle cost for an offshore wind farm. According to Carroll et al. (2016), Johnston et al. (2020) and Selot et al. (2019), the O&M cost is approximately 20-25% of the levelized cost of energy (LCOE), which represents the average lift-cycle of the electricity generated from a given power source per megawatt-hour. Compared to operating costs, maintenance costs are more important in controlling the LCOE (Ren et al., 2021b). In maintenance activities, many service providers often use larger vessels like service operation vessel (SOV). However, SOVs' cost and fuel consumption are very high during maintenance activities. The common method to reduce the cost of maintenance is optimizing the plan and schedule of SOVs service. There are several models are created to optimize the planning and scheduling of maintenance. Dai et al. (2015) applied the concept of "maintenance grouping", which enables maintenance tasks of different types scheduled in the same planning period, or even in the same visit, in the maintenance strategy. Two mathematical methods called art-flow and path-flow are introduced by Stålhane et al. (2015) to study the planning and scheduling the maintenance tasks. An optimization was conducted by Lazakis and Khan (2021) by optimizing entire maintenance task sequence to reduce the overall cost and increase the operational window.

There are studies focusing on connections between the Service operation vessel (SOV) and offshore wind turbines. Li (2021) conducted the investigation of the walk bridge between wind turbine and SOV. A new concept of crew transfer vessel (CTV) was introduced by Endrerud et al. (2015) and compared with the SOV containing accommodation, crane and workshop facilities. There are two kinds of maintenance: corrective tasks and preventive tasks (Stålhane et al., 2015). Some of the maintenance activities require vessel to stay at the turbine for the duration of the operation like inspection of the foundation using remotely operated underwater vessel (ROV). Often, large vessels originating from the oil & gas sector are used to conduct these tasks using ROV for visual inspections, video recording and testing of cathodic protection systems. These vessels however, while offering increased payloads and stability in harsher environmental conditions typically suitable for deepwater offshore oil and gas production, do not offer a significant increase in operational time that offsets their increased daily costs that can be approximately five to ten times of the small vessels. A single point mooring system (SPMS) (Figure 5.1) was recently developed for small offshore support vessel which can significantly cut the complexity and cost of conducting sub-sea inspection and maintenance operations on the rapidly increasing number of offshore wind turbine structures deployed in the North Sea where complex combinations of wind, wave and current can lead to significant downtime. With the SPMS, the vessel achieves a stable position under the wind, wave, and current forces by utilising a single rope/mooring line to restrain motion at a fixed radius around the offshore wind turbine foundation. This allows the ROV to be deployed over the stern or side of the vessel, conducting sub-sea inspections around 30 - 45 metres, with closer moorings possible if required. The connection mooring line makes the vessel and the offshore wind turbine combined multi-body system. This wind turbine and offshore support vessel multi-body system is different from aforementioned TLP-TAD system since the distance is much larger than the diameter of the structure (about 3 times of the wind turbine supporting column's diameter).

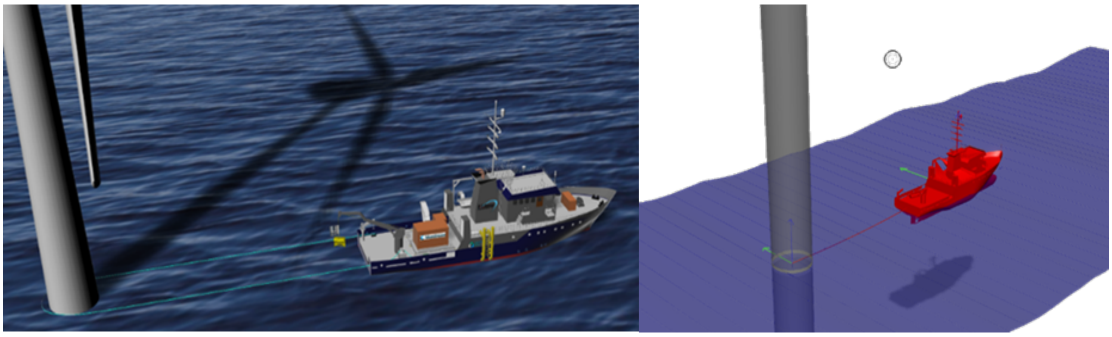

Figure 5.1 The arrangement of single point mooring system (SPMS) model

The hydrodynamic interaction between the wind turbine and offshore support vessel is not dominated in the coupled simulation under such situation, however, the mooring line between offshore support vessel and fairlead on wind turbine column plays a vital role in the relative response of multi-body system. The research described in this chapter is based on the numerical simulation using the approach similar to that in Chapter 4 complimented by comprehensive filed data obtained in the real-world field operation of offshore wind farm service. To achieve this, original drawings of the vessel are used to set up the numerical model including hull form, mass and buoyancy and accurate weight distribution. As safety criteria, limits have been defined for the motion of the vessel in all six degrees-of-freedom and the accelerations experienced on the working deck, as both of these determine the suitability of launching and recovering an ROV over the stern or side of the vessel. To represent the fixed and floating wind turbines, this study has modelled a mono-piles/tripods bottom fixed wind turbines and the Hywind Spar floating wind turbine. The configuration of the offshore wind turbine and offshore support vessel are shown in Figure 5.1. The hydrodynamic parameters are calculated using Wamit through HydroD and time domain coupled analysis is operated in SIMA v4.0.

5.2 Model set-up of the offshore wind turbine and offshore support vessel

5.2.1 Offshore support vessel

The offshore support vessel employed in the study is a small support vessel. The main particulars of the vessel are shown in Table 5.1.

Table 5.1 Particulars of offshore support vessel

Dimensions	Unit	Value
Length overall	m	38.92
Length between Perpendiculars	m	32.10
Length waterline	m	34.60
Breadth Moulded	m	9.20
Depth Moulded	m	4.50
Draught Design Water Line	m	3.10
Displacement at Design Water Line	m^3	495.0
LCG from AP	m	15.47
VCG from BL	m	4.25
Mass	ton	393

5.2.2 Fixed/Floating offshore wind turbine

To represent the fixed and floating wind turbines, this study has modelled a mono-piles bottom fixed wind turbines and the Hywind Spar floating wind turbine.

The fixed wind turbine with a tripod support structure is considered as a fixed offshore wind turbine for this project (Figure 5.2). The height of the tower is set to be 120m and the diameter of the column of the support structure is 6.5m.

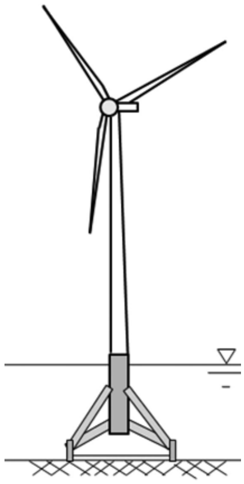

Figure 5.2 Configuration of fixed offshore wind turbine

The floating offshore wind turbine considered in this study is Hywind spar as shown in Figure 5.3. The particulars of Hywind spar wind turbine is listed in Table 5.2 the below (Myhr et al., 2011):

Table 5.2 Particulars of Hywind spar wind turbine

Dimensions	Unit	Value
Depth to Platform Base Below WL (Total Draft)	m	120
Elevation to Platform Top (Tower Base) Above WL	m	10
Depth to Top of Taper Below WL	m	4
Depth to Bottom of Taper Below WL	m	12
Platform Diameter Above Taper	m	6.5
Platform Diameter Below Taper	m	9.4

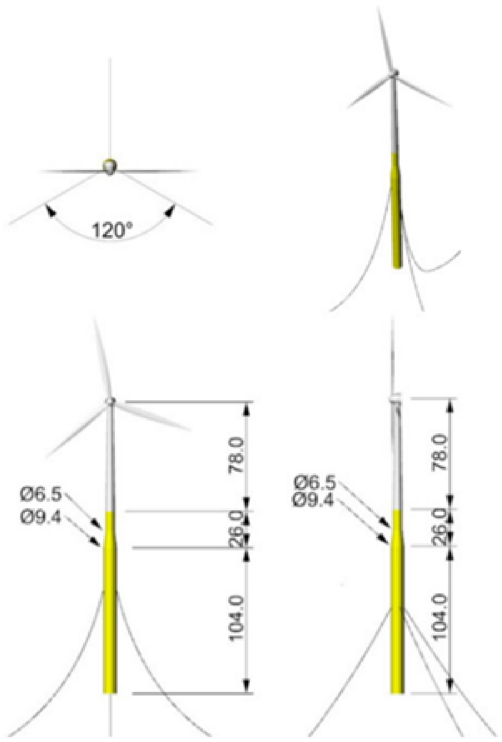

Figure 5.3 Configuration of Hywind Spar floating offshore wind turbine

5.2.3 Mooring system

The single rope/mooring line to restrain motion of the vessel at a fixed radius around the foundation is a 3-strand Superflex polyester rope with dimension of 24 mm which is the same as used in the vessel. The cholesteric of mooring line shows in Figure 5.4. The MBL (Minimum Breaking Limitation) of the mooring rope is 10 tonnes. The load vs elongation of the mooring line shows in Table 5.3.

Table 5.3 The load vs Elongation of the mooring line

Elongation (%)	Force (N)
0.049	318.19
0.075	3210.88
0.100	10081.04

0.122	19482.25
0.138	30329.86
0.155	50940.26
0.163	66850.11
0.167	78782.44
0.183	89268.48
0.189	100116.09
0.195	108432.59
0.199	111686.85

In the field operation, one end of the mooring line secured to the bollard at deck, then the mooring line bypass the turbine structure and the other end of the mooring line attaches to the fixed dynamometer to vessel structure for reading the tension. The vessel and the mooring are a passive system. There is no winch force just a maximum load on the system based on the load cell and mooring line specification. As the ship mooring system is passive, there is no rated pull force.

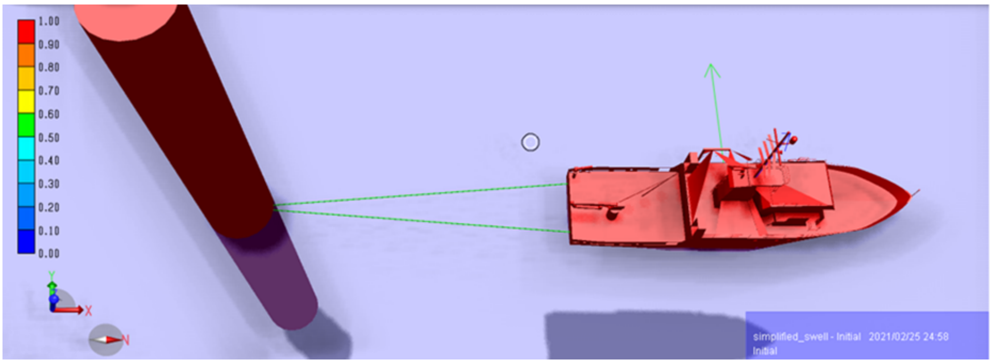

Figure 5.4 Connection between vessel & turbine assembled in modelling

To simplify the modelling aimed at reducing computational timing, the connection between offshore support vessel and wind turbine are simplified in the present project into two lines which are attached to same point in the middle of the wind turbine's structure and two separate fairleads on offshore support vessel. The fixed wind turbine is also simplified into a cylinder with a constant force at the head of the cylinder which represents the wind force on the turbines. The configuration of the simplified model is shown in Figure 5.4.

5.2.4 Wind force

The wind force operated on the wind turbine and the vessel. In the present case, the wind force on wind turbine is set as a constant force operated on the top of the cylinder. The wind force on the vessel is calculated according to the Eq. (2.97) in Chapter 2 that:

$$F_{wind} = \frac{1}{2}\rho v^2 C_{wind} A \tag{5.1}$$

where ρ is the air density, ν is the incoming wind speed, C_{wind} is the wind coefficient and the A is the project area of the member which is normal to the direction of the force. The project area and the wind coefficient are depended on the structures crossing section and their arrangements. The shielding effect of the wind force between different structures should be taken into account. The details of wind coefficients on different cross sections and shielding effect coefficients are provided in the DNV-RP-C205.

5.3 Interaction between offshore wind turbine and offshore support vessel

5.3.1 Full scale test and numerical simulation environment condition

Several simulations of representative weather conditions for North Sea locations are verified in order to calibrate the model with measured test data from the inspection campaign which was scheduled to take place across a number of offshore wind farms in 2020. This will allow for data collection at a large number of offshore structures with different support structure design which assisted for data analysing and validation of the numerical system, as well as any optimisations applied at full scale.

The environmental data collected from weather forecast for wind farm. By selecting four offshore wind turbines from the field, selecting the environmental conditions for the exact time while the vessel hang to the specific turbine (Table 5.4).

Table 5.4 Environmental data collected from weather forecast

	Wind(m/s)		Wave(m)		Swell(m)		Current(m/s)	
	Dir.	Value	Dir.	Value	Dir.	Value	Dir.	Value
26	NW/150	2.4-3.6	NW/150	0.2	SE/220	0.2	NW/125	0.07-0.15
72	NW/125	3.6-7.9	NW/125	0.5	SW/250	0.2	SE/325	0.14-0.22

5.3.2 Mesh convergence of the offshore support vessel model

Since there are two bodies in the hydrodynamic interaction calculation in the present study, the panel mesh for wind turbine and vessel are needed. The hydrodynamic parameters are calculated for the two structures connected by the SPMS. Mesh convergence analysis is conducted in the present study as shown in Figure 5.5.

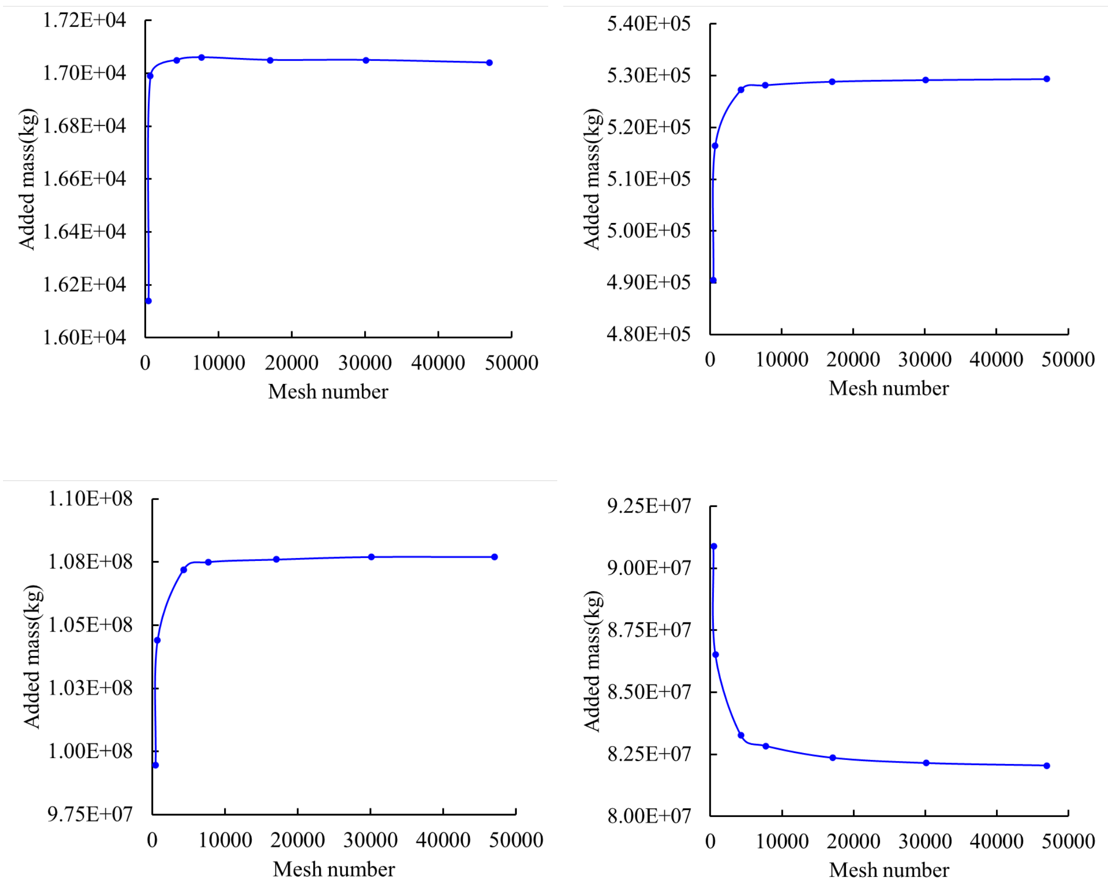

Figure 5.5 Mesh convergence of offshore support vessel panel model. (a) Surge added mass of offshore support vessel; (b) Heave added mass of offshore support vessel; (c)Roll added mass of offshore support vessel; (d)Yaw added mass of offshore support vessel.

The wind turbine has been simplified to a simple cylinder, so it is very easy to reach the convergence with increasing panel meshes. Once the panel mesh of offshore support vessel reaches the convergence, the meshes of wind turbine and vessel panel model can be determined.

The added mass in different direction for offshore support vessel with different meshes are calculated and shown in Figure 5.5. The added mass in surge, heave and roll direction converged very fast with increasing mesh number. The added mass in yaw direction is most difficult hydrodynamic parameter reaching convergence with the increasing mesh number. When the mesh number larger than 20000, the added mass converged in all direction.

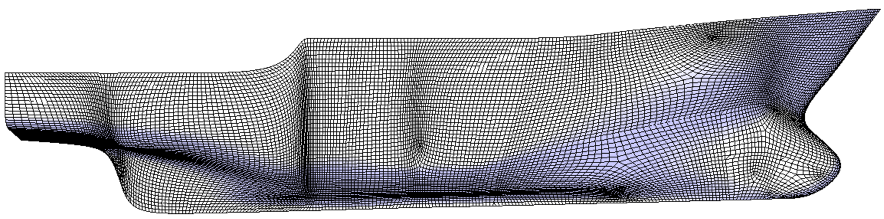

Figure 5.6 Visualization of the panel mesh of offshore support vessel

5.3.3 Validation of the force along the connecting lines

The numerical model is further validated by comparison with the full-scale measurements obtained from operation at sea during offshore wind farm services. The environmental information of wind and current from MetOcean services is applied in the simulation. The detailed environmental condition is shown in Table 5.4. The maximum and mean tension in the mooring lines between offshore support vessel and wind turbine (Figure 5.7) are applied to validate the accuracy of the numerical simulation in this chapter.

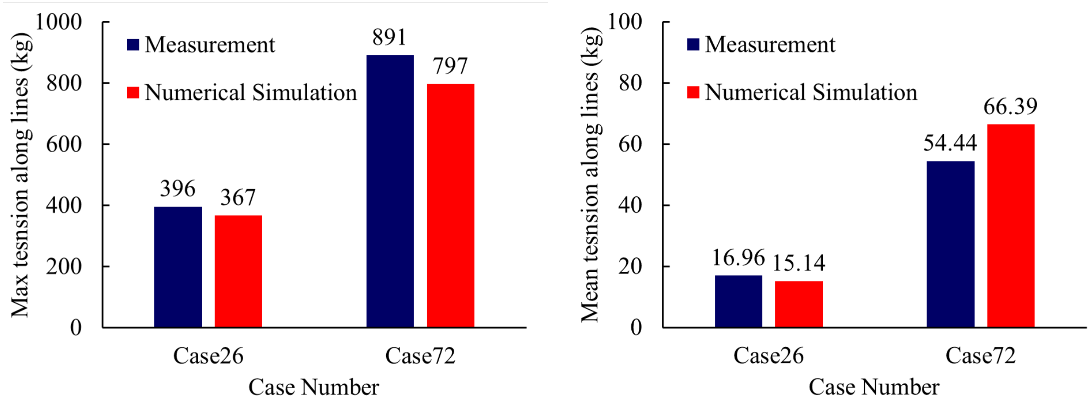

Figure 5.7 Maximum and mean tension along the connection mooring lines between wind turbine and offshore support vessel

There are two sets of environmental conditions are employed in the simulation and compare with the full-scale results. The wind and current velocity are adjusted in the range given in Table 5.4. According to Figure 5.7, both maximum tension and mean tension along the connecting mooring lines between wind turbine and offshore support vessel under two conditions obtained from numerical simulation and full-scale measurements are similar. The difference of maximum and mean force along connecting lines in Case 72 are slightly larger than those in Case 26. The difference may be caused by the wind and current coefficients of offshore support vessel since the wind and current coefficients of the offshore support vessel are estimated by a vessel which is similar to the offshore support vessel in the present study. Comparisons show that discrepancies between the present numerical solutions and the field measurements are approximately 7.3% for maximum tension and 10.7% for mean tension in the connecting mooring lines in Case 26 and 10.5% for maximum tension and 20.1%for mean tension in connecting lines in Case 72.

5.3.4 Relative Motion of the wind turbine and offshore support vessel and dynamic tension in the connecting mooring line

The vessel is tied to the wind turbine during the operation. The motion of the offshore vessel is restricted by the mooring lines between the vessel and wind turbine. In this chapter, there are 3 conditions (Table 5.5) are considered to investigate the motion characteristics of offshore support vessel connecting to wind turbine during operation. The directions of the wave and current is set at the same direction from 0°. The difference between wind and wave direction is set from 0° to 30° which covers 95% of wind-wave difference range at sea (Bachynski et al., 2014). Both fixed and floating offshore wind turbine are employed in the numerical simulation. The distance between centre of the supporting column of the wind turbine and the centre of vessel at original position is 56.5m.

Table 5.5 Environmental conditions applied in the numerical simulation

Environmental Conditions	Wind speed(m/s)	Significant wave height (m)	Peak wave period (s)	Current velocity (m/s)
LC	3.4	0.4	4.5	0.5
MC	5.4	0.8	5.5	0.75
HC	7.9	1.3	6.5	0.75

The motion of the offshore vessel and the force along the mooring lines connecting them are calculated using the present numerical model. The environmental conditions are increasing from low condition (LC) to high condition (HC) with increasing wave, wind and current speed.

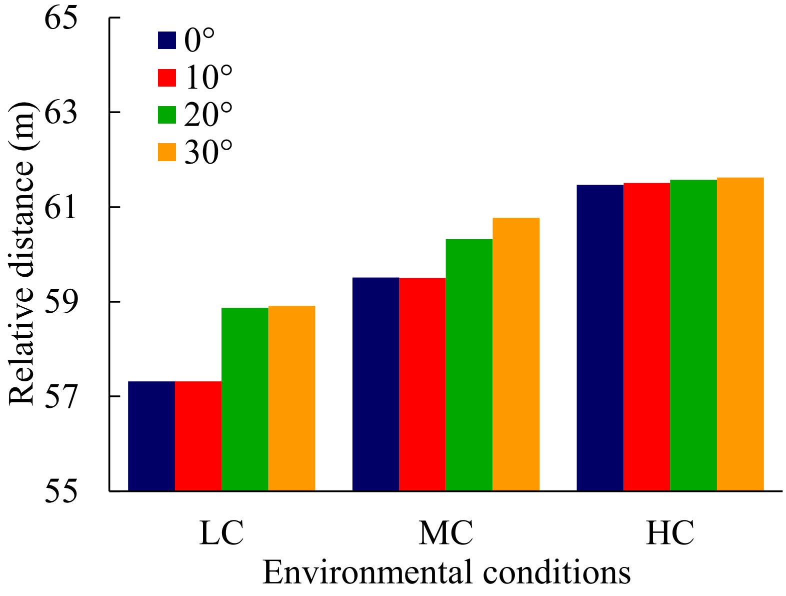

Figure 5.8 Relative distance between fixed wind turbine and offshore support vessel under different environmental conditions and wind-wave misalignment

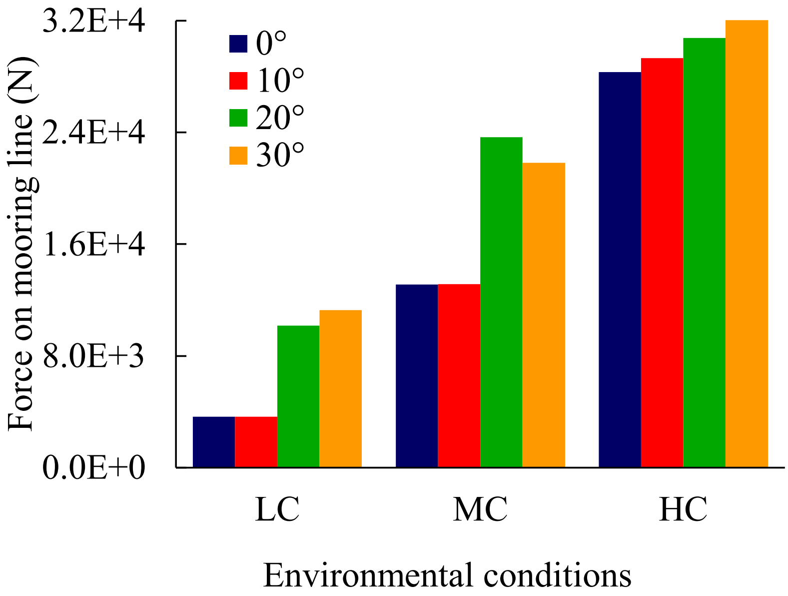

Figure 5.9 Tension in the mooring lines between fixed wind turbine and offshore support vessel under different environmental conditions and wind-wave misalignment

Figure 5.8 shows the relative distance between the centre of the fixed wind turbine and offshore support vessel. It can be seen that the relative distance changes little when the misalignment is small (0° and 10°) under LC and MC conditions. However, with the misalignment increasing from 10° to 20°, the distance rises sharply and keeps in a stable level with increasing misalignment from 20° to 30°. When the environmental condition is high, the wind-wave misalignment have little impact on the relative distance as shown in Figure 5.8. It indicates that the wind direction is more dominant effect when the environmental condition is low. While the impact of the wind-wave misalignment on the relative distance is obvious in the range between 10° to 20°, it is less so for other misalignment range. This may depend on the wind force component comparing to the total environmental load. Under low environmental condition (e.g., 1.5 m/s), both wave and wind impact are small which resulting in the weak impact of the misalignment. As evident in Figure 5.8 and Figure 5.9, under high environmental condition (HC), the wind-wave misalignment is less dominant compared to low environmental condition (LC) and medium environmental condition (MC). Consequently, the critical value of wind-wave misalignment for the distinct jump of relative distance and tension in the connecting lines will change with wind strength as shown in Figure 5.10 and Figure 5.11. In this thesis, the LC condition is selected for further investigation with different wind speed.

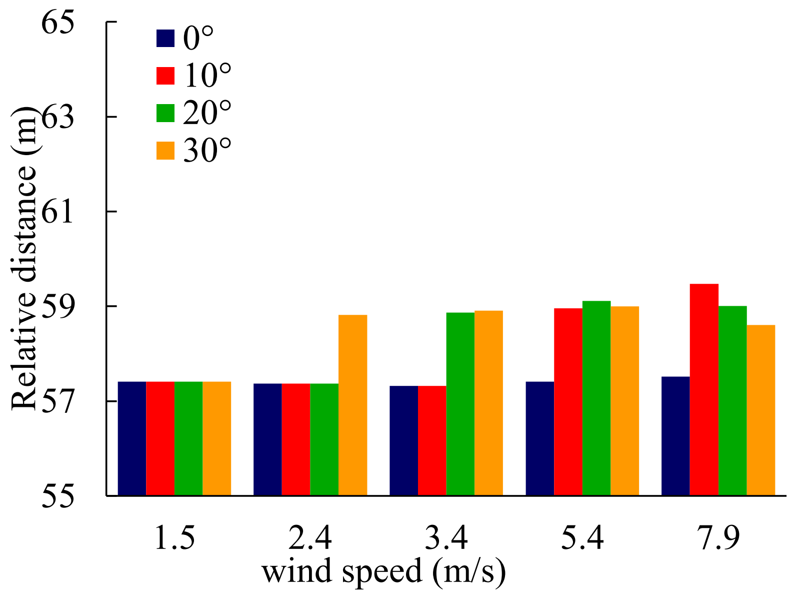

Figure 5.10 Relative distance between fixed wind turbine and offshore support vessel under LC condition with different wind speed and wind-wave misalignment

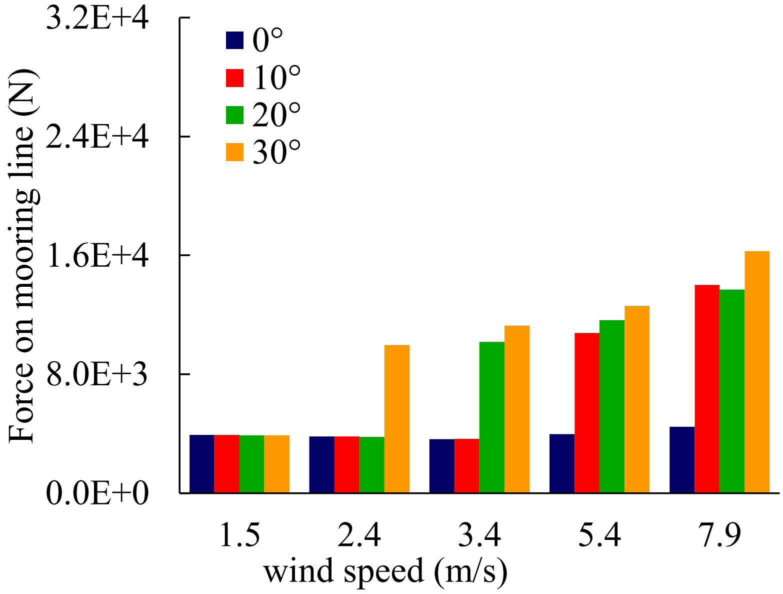

Figure 5.11 Tension in mooring line between fixed wind turbine and offshore support vessel under LC condition with different wind speed and wind-wave misalignment

The relative distance and tension in the connecting mooring line between wind turbine and offshore support vessel under different wind speeds are shown in Figure 5.10 and Figure 5.11 respectively. The wave condition and current speeds are set as constant which is same to the LC condition. The direction of wind and current are also set from 0°. It is noted that a critical value of wind-wave misalignment which leads the distinct jump of relative distance and tension in the connecting line is changing from more than 30° to less than 10° with increasing wind speed from 1.5m/s to 7.9m/s. The critical value of wind-wave misalignment is given approximately since the limitation of the cases with different misalignments considered in the study. For instance, at wind speed 2.4 m/s, a clear jump is observed for a critical value of wind-wave misalignment approximately 30°. However, the impact of wind-wave misalignment on the relative motion and the tension in the connecting line are rather small before and after the critical value. This verified that the sudden jump of the relative distance and tension in the connecting mooring line is the consequence of the combined effect of the wind strength and the wind-wave misalignment. It also indicates that the wind-wave misalignment needs to be considered during field operation.

The relative distance and tension the mooring line are calculated under the conditions that the base direction (wave directions) is 0° and wind direction is changing from 0° to 30°. It is worth noting that during the offshore support vessel operation at sea, the base direction is random. The relative distance and the tension in connecting line under different base direction and wind-wave misalignment are further investigated in detail.

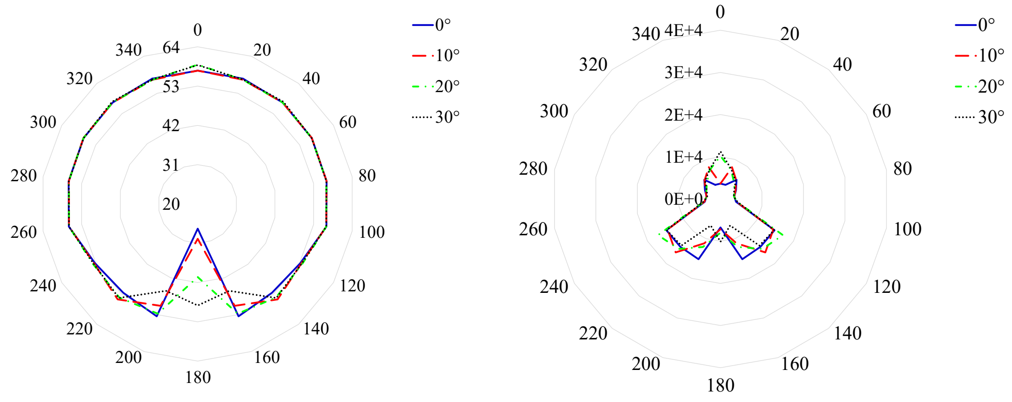

Figure 5.12 Maximum relative distance and maximum tension in the connecting mooring line (right) under the LC condition with different wind-wave misalignment

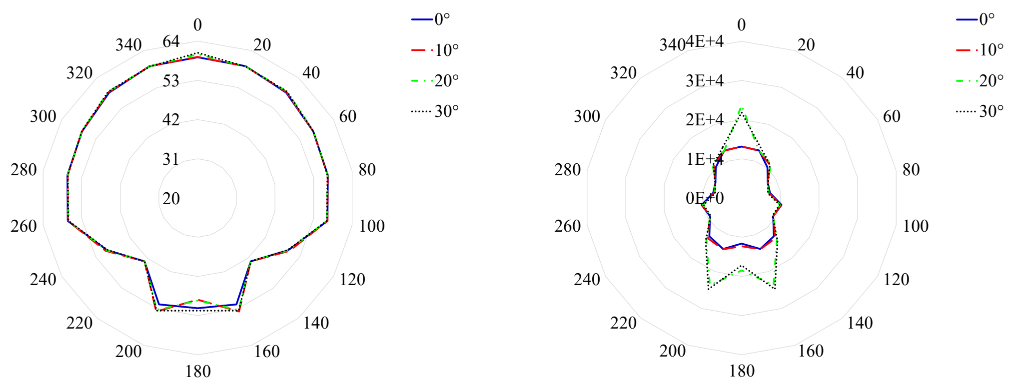

Figure 5.13 Maximum relative distance and maximum tension in the connecting mooring line (right) under the MC condition with different wind-wave misalignment

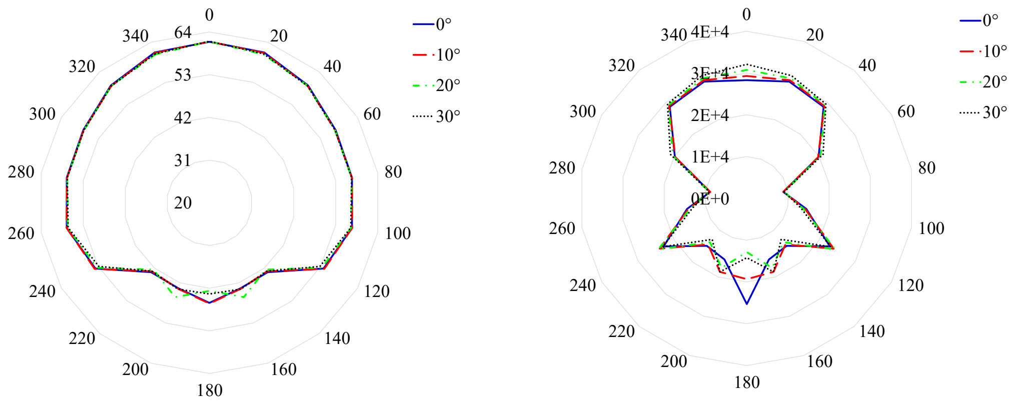

Figure 5.14 Maximum relative distance and maximum tension in the connecting mooring line (right) under the HC condition with different wind-wave misalignment

The maximum relative distance and the maximum tension in the connecting mooring line under different environmental conditions with different wind-wave misalignment are shown in Figure 5.12-14. The base directions (incident wave direction) are selected from 0° to 180°. Since the coupled wind turbine-vessel model is symmetrical, the relative distance and the tension curves are also symmetrical. For all environmental conditions (LC, MC, HC), it is seen that the misalignment has significant and varied impact on both relative distance and tension in the connecting lines when the base direction is around 0° and 180°. However, for the base direction in the range of 60° to 120°, the relative distance and the tension in the connecting lines are similar under different wind-wave misalignments as the four lines of different colours representing the four misalignments being overlap each other. Since the projection of the coupled model changes little in the direction ranging from 60° to 120°, the wind force only changes slightly leading to the smaller difference of relative distance and tension in the connecting line under different wind-wave misalignment.

5.3.5 Dynamics analysis of coupled system of floating wind turbine and offshore support vessel

There is a clear trend of offshore wind development progressively moving towards further offshore due to the increased wind energy density. Serval prototypes of floating offshore wind turbines are recently installed and connected to local grid, and a number of large-scale wind farms with floating offshore wind turbines are proposed around the world. This section presents a hydrodynamic study of coupled system of floating wind turbine and offshore support vessel representing the real-world offshore wind farm service operation.

The maximum relative distance and the maximum tension in the connecting lines between floating wind turbine and offshore support vessel are calculated to investigate the impact due to the motion of the floating wind turbine on the maximum relative distance and the maximum tension in the connecting line.

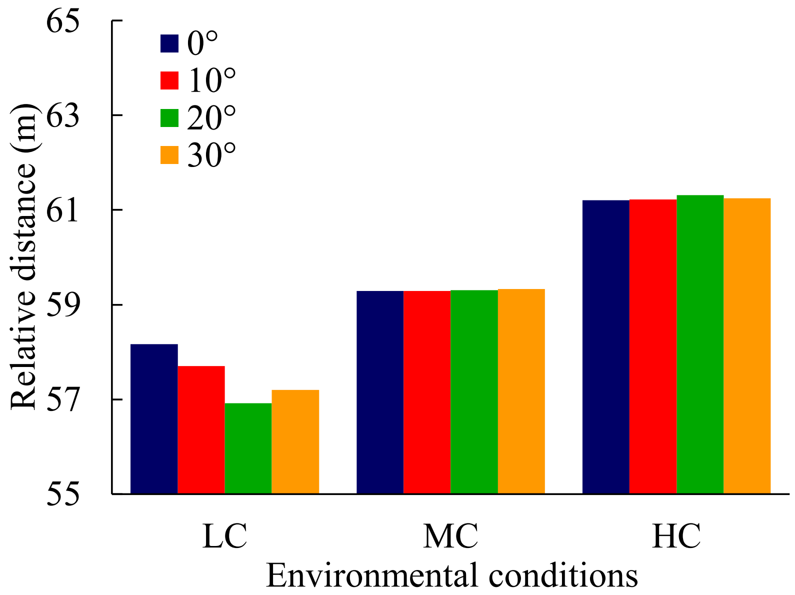

Figure 5.15 Maximum relative distance between floating wind turbine and offshore support vessel under different environmental conditions and wind-wave misalignment

Figure 5.15 shows that the relative distance between the floating wind turbine and the offshore support vessel decreases as the misalignment increases for the low environmental condition (LC) applied. However, the misalignment appears to have little impact on the relative distance for the medium and high environmental conditions (MC and HC) considered in the simulation. It indicates that the maximum relative distance is more sensitive to the wind-wave misalignment at low environmental condition.

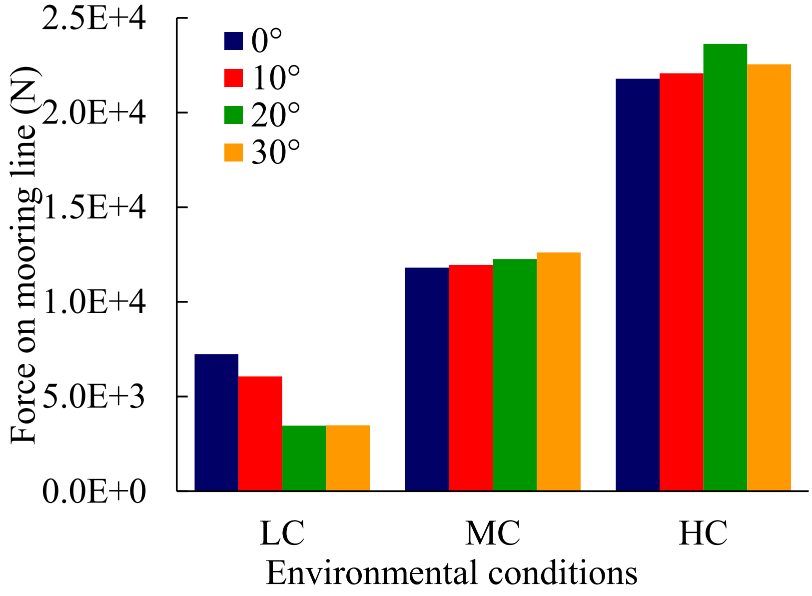

Figure 5.16 Force along the mooring lines between floating wind turbine and offshore support vessel under different environmental conditions and wind-wave misalignment

Comparing to the coupled system of a fixed wind turbine and offshore support vessel, Figure 5.16 shows that the wind-wave misalignment has greater impact on the maximum tension in the connecting line under the low environmental condition (LC) and the tension tends to decrease as the misalignment increases. In contrast to that, the misalignment of wind-wave appears to have little impact on the higher environmental conditions (MC and HC).

The maximum relative distance and the maximum line tension with different wind speed under LC condition for wave and current are calculated to examine the details of the wind impact. The wind speed is set from 1.5 m/s to 7.9 m/s (with the original wind speed is 3.4 m/s) and four wind-wave misalignments (0°, 10°, 20° and 30°) are considered.

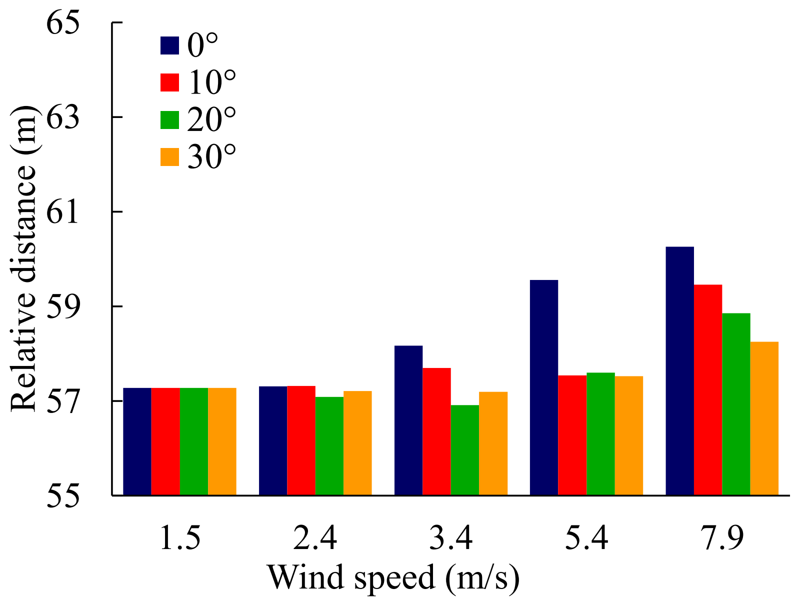

Figure 5.17 Maximum relative distance between floating wind turbine and offshore support vessel under LC condition with different wind speed and wind-wave misalignment

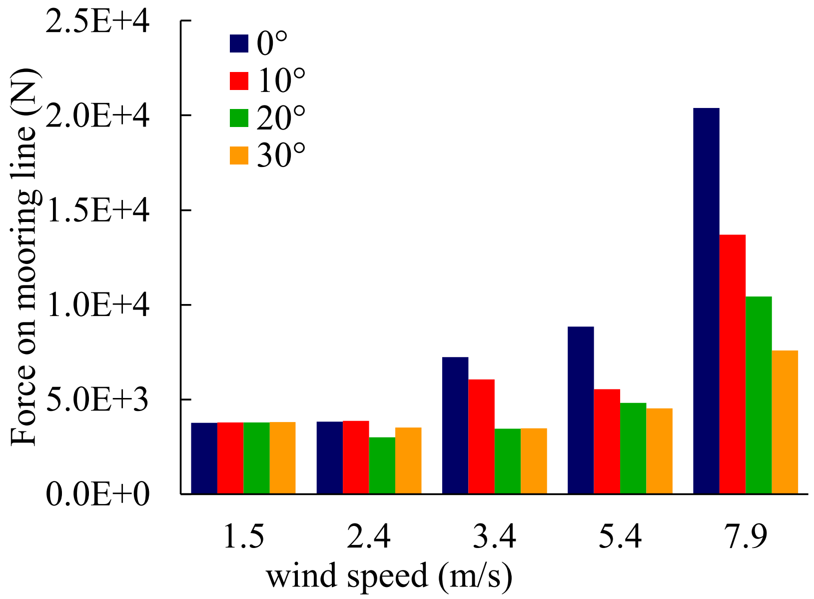

Figure 5.18 Maximum force along mooring lines between floating wind turbine and offshore support vessel under LC condition with different wind speed and wind-wave misalignment

Figure 5.17 and Figure 5.18 shown the maximum relative distance and the maximum tension in the connecting line respectively. It is noted that the maximum relative distance and the maximum line tension are of similar trend when the wind speed is low (1.5m/s and 2.4m/s).

Both wind speed and wind-wave misalignment appear to have little impact on the maximum relative distance and the maximum line tension. As the wind speed increases, the maximum relative distance and the maximum line tension tend to increase. It is evident that the maximum relative distance and the maximum line tension decrease markedly with increasing wind-wave misalignment under wind speed from 3.4 m/s to 7.9 m/s showing greater impact of wind-wave alignment at higher wind speed. Different to the fixed wind turbine, this characteristic indicates that the maximum line tension occurs when the wind, wave and current are in the same direction (colinear environment), an important information for the on-board crew of the offshore support vessel during the service operation of the floating wind turbines.

5.4 Summary

The coupled system of a fixed or floating wind turbine and an offshore support vessel under different environmental conditions and various wind-wave misalignment are investigated based on numerical simulation. The present numerical model for the coupled analysis in time domain are rigorously validated against field measurements of the full-scale operation at sea during the service to offshore wind farms located in Baltic Sea and North Sea. The maximum relative distance and the maximum tension in the connecting lines are examined in detail under different conditions.

- When the wind turbine is fixed, the maximum relative distance and force along the connecting lines have significantly influenced by the wind-wave misalignment under the low condition (LC) and medium condition (MC). However, there is little impact of misalignment on these under high condition (HC).

- The increase wind speed and wind-wave misalignment will lead a jump of maximum relative distance and maximum force along the connecting lines when the wind turbine is fixed.

- When the wind turbine is fixed, the impact of the wind-wave misalignment on the relative distance and force are mostly concentrated in the base directions of 0° and 180°. When the base direction is at the range of 60° to 120°, the relative distance and force along connecting lines are similar under different wind-wave misalignments

- When the wind turbine is floating, the impact of the wind on maximum relative distance and force along the connecting lines are shown under low condition. There is little impact of wind-wave misalignment when the environmental condition is medium and high condition.

- The increasing amplitude of the maximum relative distance and force along the connecting lines are reduced with rising wind-wave misalignment. In other word, the maximum and force along the connecting lines are highest comparing with other wind-wave misalignment conditions when the wind speed is same.

6 Conclusions and recommendation of future work

6.1 Conclusions

The main strength of the present work is the comprehensive numerical study focusing on various aspects of linear and non-linear hydrodynamic characteristics of different kinds of multi-platforms system and multiple columns offshore structures. These aspects are crucial for the accurate prediction of surface elevation, wave loads on and motion response of the multi-platform system, thus key impact on the reliable design and safe operation of such offshore structures. Analysis on three main structure configurations is conducted in the thesis, fixed multiple columns structure, floating multi-platforms system (TLP-TAD) and fixed/floating wind turbine with offshore support vessel. Model test results of the fixed multiple columns cases and the TLP-TAD model are used to validate the newly developed numerical models for the cases respectively. The field data from the full-scale prototype offshore operation for the offshore support vessel during the O&M operation of offshore wind farms is applied to validate the coupled wind turbine-vessel model. Numerical simulation provides substantial details of the motion of the platform, linear/nonlinear forces on the structures and surface elevation around the platforms under different environmental conditions.

The principal contribution and conclusions of the present thesis are summarised below:

1. The interaction between two adjacent floating platforms increases both the first-order and the second-order wave force on the two bodies along their arrangement direction in multi-platforms system. For the structure at the lee position, the interaction between the two bodies has great impact on the wave force. This should be taken into consideration in the prediction of the relative distance and design of the gangway between platforms especially under the beam sea condition.

2. Under the beam sea condition, the wave loads in surge/pitch direction (which are perpendicular to the incident wave) on TLP/TAD in coupled model cannot be neglected since the diffraction and radiation in surge direction caused by adjacent platform. This

should be considered in the gangway design between two platforms.

3. The influence of interaction between the two platforms on TLP's sum-frequency heave force in TLP/TAD system is highly dependent on the wave direction. The peak value of sum-frequency QTF matrix in coupled model under head sea is much higher than that of the TLP in isolation. The sum-frequency QTF matrix under the beam sea in TLP/TAD system is lower than that of TLP in isolation. This characteristics of sum-frequency force in heave is a crucial design feature to avoid the significant nonlinear (high frequency "springing" and "ringing") wave load which often induces TLP undergoing resonant motion in vertical planes and further leads to fatigue load to tendons and risers in TLP-TAD system.

4. The drift force on TAD in surge are increased by the interaction between the two floating platforms. Meanwhile, shielding effect is observed across period ranged analysed in head sea condition. The combination of these two effects (hydrodynamic interaction and shielding effect) may result in the drift force on TAD much higher in some range of wave period and further leads to sudden increase in the top tension of mooring lines for TAD.

5. Increasing ratio of corner radius tends to reduce wave run-up along the rounded-corner square column under 0° incident wave, and a higher wave run-up under 45° incident wave.

6. Near-trapping frequency model previously proposed for multiple circular columns is demonstrated still valid for the four rounded-corner square columns. Further, the peak surface elevation due to near-trapping reduces with increasing corner ratio.

7. The impact of the column's corner ratio on the second-order component of surface elevation is significantly larger than that on the first-order component. The peak value of the second-order surface component caused by superposition decreases with higher ratio of column's corner. However, for the peak surface elevation caused by near-trapping, the second-order surface component decreases with lower ratio of column's corner.

8. During wave interaction with four rounded-corner square columns, it is demonstrated that superposition is responsible to a single peak surface elevation occurring under 0° incident wave, while different peaks of surface elevation depending on scatting parameter under 45° incident wave are demonstrated due to two mechanisms namely near-trapping and superposition, respectively.

9. During O&M operation of offshore wind farm with fixed offshore wind turbine using single point mooring system, the maximum relative distance and tension in the connecting lines are significantly influenced by the wind-wave misalignment under the low environmental condition (LC) and medium condition (MC). However, there is little impact of misalignment under high condition (HC). For floating wind turbine, the impact of wind-wave misalignment is rather small when the environmental condition is medium and high condition.

10. Weather window for safe operation of the fixed offshore wind farm O&M operation using single point mooring system requires careful analysis as increase in wind speed and wind-wave misalignment evidently leading to a jump of maximum relative distance and maximum tension in the connecting lines.

11. For floating offshore wind farm O&M operation, the increasing maximum relative distances and tensions in the connecting lines are reduced with rising wind-wave misalignment. In other words, the maximum relative distance and maximum tension in the connecting lines are the highest when the wind and wave directions are same comparing with other wind-wave misalignment conditions.

6.2 Suggestions for future work

Although the present thesis covered wide range aspects of the hydrodynamic interactions between platforms in multi-platforms system or multiple columns structures on motion, linear/nonlinear force and the surface elevation around structures. There are still limitations on aspects requiring further research and study. The work in this thesis is based on the potential theory that the fluid is assumed inviscid, irrotational and incompressible. The viscous effect is ignored in this method. The assumption of a perturbation solution in terms of a small wave slope of the incident waves is applied in analysis of diffraction and radiation. The viscosity is ignored in the present thesis. The prediction of free surface elevation around columns might be lower with the viscous effect. For the strong nonlinear incident wave, there might be a jet-like runup along the column. The viscosity might be more important in the jet-like runup and the potential flow is not sufficient to predict the jet-like runup amplitude. Without viscous damping, the potential flow solution will lead the hydrodynamic damping on the platform lower than realistic condition. Thus, the platform tends to follow the waves leading to overestimate of the air gap. This may potentially lead to non-conservative design. Since the viscosity is ignored in the present case, the motion amplitude could be larger than realistic case and further lead to prolonged ringing and springing in the numerical prediction with associated tensions in tendons.

It should be noted that the sum-frequency wave force on TLP typically results in nonlinear motion in vertical planes which will lead to the high-frequency tensions in tendons. To ensure the numerical simulation more realistic, material properties of the tendons and their fatigue analysis should be included.

In offshore industry, the platforms in the multi-platforms system are typically connected using hawser and bridge. The response of the connecting bridge with different configurations and its strength should be examined according to the hydrodynamic response in future.

The present work is mainly based on potential theory, the viscous effect should be considered in future, especially on the wave run-up along the columns.

References

ABDUSSAMIE, N., DROBYSHEVSKI, Y., OJEDA, R., THOMAS, G. & AMIN, W. 2017. Experimental investigation of wave-in-deck impact events on a TLP model. *Ocean Engineering,* 142**,** 541-562.

ADRIAN, E. & WONG, S. Overview of the Malikai Project. Offshore Technology Conference, 2018. Offshore Technology Conference.

ARAMANADKA, S. B., YONG, L., KOTA, R., JAMAL, S. A. & YEAP, F. Malikai Tension Leg Platform-Drilling Tender Vessel-Top Tension Riser Operations. Offshore Technology Conference, 2018. Offshore Technology Conference.

BACHYNSKI, E. E., KVITTEM, M. I., LUAN, C. & MOAN, T. 2014. Wind-wave misalignment effects on floating wind turbines: motions and tower load effects. *Journal of Offshore Mechanics and Arctic Engineering,* 136.

BIAO, W., XIAOLONG, Y., LICHENG, Q. & LEI, W. 2018. A comparative study on model test and numerical analysis of wave basin based on tension leg platform in south china sea. *Research and Exploration in Laboratory,* 37**,** 53-57.

BIROL, F. 2018. WEO-2018 Special Report: Offshore Energy Outlook. Inernational Energy Agency

BP 2020. Statistical Review of World Energy.

CARROLL, J., MCDONALD, A. & MCMILLAN, D. 2016. Failure rate, repair time and unscheduled O&M cost analysis of offshore wind turbines. *Wind Energy,* 19**,** 1107-1119.

CHAKRABARTI, S. K. 1978. Wave forces on multiple vertical cylinders. *Journal of the waterway, port, coastal and ocean division,* 104**,** 147-161.

CHEN, L., ZANG, J., HILLIS, A., MORGAN, G. & PLUMMER, A. 2014. Numerical investigation of wave–structure interaction using OpenFOAM. *Ocean Engineering,* 88**,** 91-109.

CHOI, Y.-M., NAM, B. W., HONG, S. Y., JUNG, D. W. & KIM, H. J. 2018. Coupled motion analysis of a tension leg platform with a tender semi-submersible system. *Ocean Engineering,* 156**,** 224-239.

CHOI, Y. & HONG, S. An analysis of hydrodynamic interaction of floating multi-body using higher-order boundary element method. The Twelfth International Offshore and Polar Engineering Conference, 2002. International Society of Offshore and Polar Engineers.

CONG, P., GOU, Y., TENG, B., ZHANG, K. & HUANG, Y. 2015. Model experiments on wave elevation around a four-cylinder structure. *Ocean Engineering,* 96**,** 40-55.

CONTENTO, G., D'ESTE, F., SICCHIERO, M., CODIGLIA, R. & CALZA, M. Run-up and wave forces on an array of vertical circular cylinders: Experimental study on the second order near trapping. The Fourteenth International Offshore and Polar Engineering Conference, 2004. International Society of Offshore and Polar Engineers.

C.-H. LEE. WAMIT THEORY MANUAL. Massachusetts Institute of Technology, 1995

DAI, L., STÅLHANE, M. & UTNE, I. B. 2015. Routing and scheduling of maintenance fleet for offshore wind farms. *Wind Engineering,* 39**,** 15-30.

DONG, Q., LU, H., YANG, J. & GUO, X. 2019. Dynamic gangway responses between TLP and semi-submersible platform during tender-assisted drilling. *Marine Structures,* 67**,** 102645.

DONG, Z. & ZHAN, J.-M. 2009. Numerical Modeling of Wave Evolution and Runup in Shallow Water. *Journal of Hydrodynamics,* 21**,** 731-738.

ENDRERUD, V., AUSTRENG, K. R., KESERIC, N. & LIYANAGE, J. P. New vessel concepts for operations and maintenance of offshore wind farms. The Twenty-fifth International Ocean and Polar Engineering Conference, 2015. OnePetro.

EVANS, D. & PORTER, R. 1997. Near-trapping of waves by circular arrays of vertical cylinders. *Applied Ocean Research,* 19**,** 83-99.

FANG, Z., XIAO, L., GUO, Y., KOU, Y. & LI, J. 2018. Wave run-up on a fixed surface-piercing square column using multi-layer barrier. *Applied Ocean Research,* 71**,** 105-118.

FENG, J. & SHEN, W. Z. 2015. Solving the wind farm layout optimization problem using random search algorithm. *Renewable Energy,* 78**,** 182-192.

GANESAN, S. & SEN, D. 2016. Time domain simulation of side-by-side floating bodies using a 3D numerical wave tank approach. *Applied Ocean Research,* 58**,** 189-217.

GRICE, J., TAYLOR, P. & TAYLOR, R. E. 2013. Near-trapping effects for multi-column structures in deterministic and random waves. *Ocean Engineering,* 58**,** 60-77.

GUANCHE, R., MARTINI, M., JURADO, A. & LOSADA, I. J. 2016. Walk-to-work accessibility assessment for floating offshore wind turbines. *Ocean Engineering,* 116**,** 216-225.

GUPTA, J., BHAT, S. & YANG, T. Numerical Study of Vortex Induced Motion and Vibrations on Risers and Tension Leg Platform for Malikai. Offshore Technology Conference, 2018. Offshore Technology Conference.

HUANG, W., LI, B., CHEN, X. & ARAUJO, R. 2018. Numerical and experimental studies on dynamic gangway response between monohull flotel and FPSO in non-parallel side-by-side configuration. *Ocean Engineering,* 149**,** 341-357.

JEAN-ROBERT, F., NACIRI, M. & XIAO-BO, C. Hydrodynamics of two side-by-side vessels experiments and numerical simulations. The Sixteenth International Offshore and Polar Engineering Conference, 2006. International Society of Offshore and Polar Engineers.

JIN, Y., CHAI, S., DUFFY, J., CHIN, C. & BOSE, N. 2019. Hydrodynamics of a conceptual FLNG system in side-by-side offloading operation. *Ships and Offshore Structures,* 14**,** 104-124.

JOHNSTON, B., FOLEY, A., DORAN, J. & LITTLER, T. 2020. Levelised cost of energy, A challenge for offshore wind. *Renewable Energy,* 160**,** 876-885.

KAGEMOTO, H., MURAI, M. & FUJII, T. 2014. Second-order resonance among an array of two rows of vertical circular cylinders. *Applied Ocean Research,* 47**,** 192-198.

KARAGIANNOPOULOS, R. C. L. 2021. Offshore project commitments count set for record in coming years, deepwater to have top growth.

KIM, C. H. 1972. The hydrodynamic interaction between two cylindrical bodies floating in beam seas.

KIM, M.-H. & YUE, D. K. 1989. The complete second-order diffraction solution for an axisymmetric body Part 1. Monochromatic incident waves. *Journal of Fluid Mechanics,* 200**,** 235-264.

KOO, B. & KIM, M. 2005. Hydrodynamic interactions and relative motions of two floating platforms with mooring lines in side-by-side offloading operation. *Applied Ocean Research,* 27**,** 292-310.

KRIEBEL, D. L. 1992. Nonlinear wave interaction with a vertical circular cylinder. Part II: Wave run-up. *Ocean Engineering,* 19**,** 75-99.

KRISTIANSEN, T., BAARHOLM, R. & STANSBERG, C. T. Validation of second-order analysis in predicting diffracted wave elevation around a vertical circular cylinder. The Fourteenth International Offshore and Polar Engineering Conference, 2004. International Society of Offshore and Polar Engineers.

KVALEID, J., OOSTERLAAK, V. AND KVILLUM, T., 2014, June. Non-Linear Air Gap Analyses of a Semi-Submersible Compared With Linear Analyses and Model Tests. In International Conference on Offshore Mechanics and Arctic Engineering (Vol. 45387, p. V01BT01A012). American Society of Mechanical Engineers.

LAZAKIS, I. & KHAN, S. 2021. An optimization framework for daily route planning and scheduling of maintenance vessel activities in offshore wind farms. *Ocean Engineering,* 225**,** 108752.

LI, B. 2020. Multi-body hydrodynamic resonance and shielding effect of vessels parallel and nonparallel side-by-side. *Ocean Engineering,* 218**,** 108188.

LI, B. 2021. Effect of hydrodynamic coupling of floating offshore wind turbine and offshore support vessel. *Applied Ocean Research,* 114**,** 102707.

LI, B., HUANG, W., ARAUJO, R., BOULLAND, J. & CHEN, X. Gangway motion evaluation of an accommodation vessel operating along a turret moored FPSO. The Twenty-fifth International Ocean and Polar Engineering Conference, 2015. International Society of Offshore and Polar Engineers.

LIANG, Y. 2018. *Vortex-induced motions of multiple cylindrical offshore structures.* Newcastle University.

LIN, Y.-H., CHEN, J.-F. & LU, P.-Y. 2017. A CFD model for simulating wave run-ups and wave loads in case of different wind turbine foundations influenced by nonlinear waves. *Ocean Engineering,* 129**,** 428-440.

LINTON, C. & EVANS, D. 1990. The interaction of waves with arrays of vertical circular cylinders. *Journal of fluid mechanics,* 215**,** 549-569.

LIU, Y., KIM, M. & KIM, C. 1995. The Computation of Second-Order Mean and Double-Frequency Wave Loads on a Compliant TLP by HODEM. *International Journal of Offshore and Polar Engineering,* 5.

LOKEN, A. E. Hydrodynamic interaction between several floating bodies of arbitray form in waves. International Symposium on Hydrodynamics in Ocean Engineering, 1981. The Norwegian Institute of Technology.

LOW, Y. 2010. Influence of the setdown of a tension leg platform on the extreme airgap response. *Applied Ocean Research,* 32**,** 11-19.

LU, W., ZHAO, W., TAYLOR, P., YANG, J., XIAO, L. & LI, X. 2020. Linearity and nonlinearity in wave run-up and air-gap response for a semi-submersible platform under irregular wave excitation. *Applied Ocean Research,* 104**,** 102218.

LIU, Z., LIN, Z., TAO, L. AND LAN, J., 2016. Nonlinear wave–current interaction in water of finite depth. Journal of Waterway, Port, Coastal, and Ocean Engineering, 142(6), p.04016009.

MAHONEY, C. 2013. 2013 Deepwater Solutions & Records for Concept Selection. *Wood Group Mustang*.

MALENICA, Š., TAYLOR, R. E. & HUANG, J. 1999. Second-order water wave diffraction by an array of vertical cylinders. *Journal of Fluid Mechanics,* 390.

MARIBUS 2014. World ocean review: living with the oceans 3 Marine Resources - Opportunities and Risks.

MORANDINI, C., OROZCO, J.-M. & L'HOSTIS, D. Design issues for connecting two floating structures. International Conference on Offshore Mechanics and Arctic Engineering, 2005. 449-464.

MORRIS-THOMAS, M. & THIAGARAJAN, K. 2004. The run-up on a cylinder in progressive surface gravity waves: harmonic components. *Applied Ocean Research,* 26**,** 98-113.

MYHR, A., MAUS, K. J. & NYGAARD, T. A. Experimental and computational comparisons of the OC3-HYWIND and Tension-Leg-Buoy (TLB) floating wind turbine conceptual designs. The Twenty-first International Offshore and Polar Engineering Conference, 2011. OnePetro.

NATIONAL ACADEMIES OF SCIENCES, E. A. M. 2016. Strengthening the Safety Culture of the Offshore Oil and Gas Industry. *Transportation Research Board*.

NEWMAN, J. N. 1974. Second-order, slowly-varying forces on vessels in irregular waves.

NEWMAN, J. N. 1985. Algorithms for the free-surface Green function. *Journal of engineering mathematics,* 19**,** 57-67.

NEWMAN, J. N. 1994. Wave effects on deformable bodies. *Applied ocean research,* 16**,** 47-59.

NEWMAN, J. N. 2001. Wave effects on multiple bodies. *Hydrodynamics in ship and ocean engineering,* 3**,** 3-26.

NIEDZWECKI, J. & HUSTON, J. 1992. Wave interaction with tension leg platforms. *Ocean*

Engineering, 19**,** 21-37.

OGILVIE, T. F. 1983. Second order hydrodynamic effects on ocean platforms. *International Work Shop on Ship and Platform Motions, 1983***,** 205-343.

OK, H., LEE, S. & CHOI, J. 2017. Numerical simulation of motion of single and side-by-side vessels in regular waves using OpenFOAM. *Ships and Offshore Structures,* 12**,** 793-803.

PERIĆ, M. & SWAN, C. 2015. An experimental study of the wave excitation in the gap between two closely spaced bodies, with implications for LNG offloading. *Applied Ocean Research,* 51**,** 320-330.

PRATT, J. A., PRIEST, T. & CASTANEDA, C. J. 1997. *Offshore pioneers: Brown & Root and the history of offshore oil and gas*, Gulf Professional Publishing.

PESSOA, J., STANSBERG, C.T., FONSECA, N. AND LARANJINHA, M., 2018, June. Experimental and numerical study of the free surface elevation over the pontoons of a semisubmersible platform in waves. In International Conference on Offshore Mechanics and Arctic Engineering (Vol. 51203, p. V001T01A030). American Society of Mechanical Engineers.

PAN, Z., VADA, T., FINNE, S., NESTEGÅRD, A., HOFF, J.R., HERMUNDSTAD, E.M. AND STANSBERG, C.T., 2016, June. Benchmark study of numerical approaches for wave-current interaction problem of offshore floaters. In International Conference on Offshore Mechanics and Arctic Engineering (Vol. 49927, p. V001T01A024). American Society of Mechanical Engineers.

PAN, Z., VADA, T.K. AND NESTEGÅRD, A., 2018, June. Efficient Calculation of Low Frequency Motions for Air-Gap Prediction. In International Conference on Offshore Mechanics and Arctic Engineering (Vol. 51265, p. V07AT06A038). American Society of Mechanical Engineers.

RAMAN, H., SHANKAR, N. J. & VENKATANARASAIAH, P. 1977. Nonlinear wave interaction with vertical cylinder of large diameter. *Journal of Ship Research,* 21**,** 120-

124.

RAMAN, H. & VENKATANARASAIAH, P. 1976. Forces due to nonlinear waves on vertical cylinders. *Journal of the Waterways, Harbors and Coastal Engineering Division,* 102**,** 301-316.

REN, X., LIANG, Y. & TAO, L. Nonlinear wave surface elevation characteristics analysis around a multi-body offshore platforms system. International Conference on Offshore Mechanics and Arctic Engineering, 2019. American Society of Mechanical Engineers, V009T13A003.

REN, X. & TAO, L. Probability of slamming due to set-down of tension leg platform. The 27th International Ocean and Polar Engineering Conference, 2017. OnePetro.

REN, X. & TAO, L. Nonlinear wave surface elevation around array of truncated cylinders. The 30th International Ocean and Polar Engineering Conference, 2020. OnePetro.

REN, X. & TAO, L. 2021. Nonlinear hydrodynamic characteristics of multi-body platform system. *European Journal of Mechanics-B/Fluids*.

REN, X., TAO, L., LIANG, Y. & HAN, D. 2021a. Nonlinear wave surface elevation around a multi-column offshore structure. *Ocean Engineering,* Revisions being processed.

REN, Z., VERMA, A. S., LI, Y., TEUWEN, J. J. & JIANG, Z. 2021b. Offshore wind turbine operations and maintenance: A state-of-the-art review. *Renewable and Sustainable Energy Reviews,* 144**,** 110886.

SARKAR, A. & TAYLOR, R. E. 2001. Low-frequency responses of nonlinearly moored vessels in random waves: Coupled surge, pitch and heave motions. *Journal of fluids and structures,* 15**,** 133-150.

SELOT, F., BRINDLEY, G. & WALSH, C. 2019. Offshore wind in europe–key trends and statistics 2018.

SHAN, T.-B., YANG, J.-M., LI, X. & XIAO, L.-F. 2011. Experimental investigation on wave run-up characteristics along columns and air gap response of semi-submersible platform. *Journal of Hydrodynamics,* 23**,** 625-636.

SIMOS, A. N., SPARANO, J. V., ARANHA, J. A. & MATOS, V. L. 2nd order hydrodynamic effects on resonant heave, pitch and roll motions of a large-volume semi-submersible platform. ASME 2008 27th International Conference on Offshore Mechanics and Arctic Engineering, 2008. American Society of Mechanical Engineers, 229-237.

SMITH, E. & DIXON, W. 1987. Tender-supported operations at the Odin field. *Journal of petroleum technology,* 39**,** 324-330.

STÅLHANE, M., HVATTUM, L. M. & SKAAR, V. 2015. Optimization of routing and scheduling of vessels to perform maintenance at offshore wind farms. *Energy Procedia,* 80**,** 92-99.

SWEETMAN, B., WINTERSTEIN, S. R., MELING, T. S. & BIRKNES, J. Airgap Prediction" Use of Second-Order Diffraction and Multi-Column Models. The Eleventh International Offshore and Polar Engineering Conference, 2001. International Society of Offshore and Polar Engineers.

STANSBERG, CARL TRYGVE. "Nonlinear wave amplification around column-based platforms in steep waves." International Conference on Offshore Mechanics and Arctic Engineering. Vol. 45387. American Society of Mechanical Engineers, 2014.

TAGHIPOUR, R. & MOAN, T. Efficient frequency-domain analysis of dynamic response for the multi-body wave energy converter in multi-directional wave. The Eighteenth International Offshore and Polar Engineering Conference, 2008. International Society of Offshore and Polar Engineers.

TAYLOR, R. E. & SINCOCK, P. 1989. Wave upwelling effects in TLP and semisubmersible structures. *Ocean engineering,* 16**,** 281-306.

TECHNOLOGY, P. 2017. Full circle: decommissioning the first ever offshore windfarm.

PAKOZDI, CSABA, SVEIN-ARNE REINHOLDTSEN, AND CARL T. STANSBERG. "A Novel Semi-Empirical Non-Linear Time-Domain Formulation of Wave Elevation

Diffracted by a Vertical Column." In International Conference on Offshore Mechanics and Arctic Engineering, vol. 51203, p. V001T01A077. American Society of Mechanical Engineers, 2018.

UMAR 2019. Exploring the impact of artificial intelligence on offshore oil and gas. *Offshore Technology*.

WANG, C. & WU, G. 2007. Time domain analysis of second-order wave diffraction by an array of vertical cylinders. *Journal of Fluids and Structures,* 23**,** 605-631.

WANG, C. & WU, G. 2010. Interactions between fully nonlinear water waves and cylinder arrays in a wave tank. *Ocean Engineering,* 37**,** 400-417.

WANG, Y. & YOU, Y.-X. 2009. Numerical simulation of interaction of viscous wave fields with a semi-submersible platform [J]. *Journal of Hydrodynamics (Ser. A),* 6**,** 018.

WATAI, R., DINOI, P., RUGGERI, F., SOUTO-IGLESIAS, A. & SIMOS, A. 2015. Rankine time-domain method with application to side-by-side gap flow modeling. *Applied Ocean Research,* 50**,** 69-90.

WEI, H., XIAO, L., TIAN, X. & KOU, Y. 2017. Four-level screening method for multi-variable truncation design of deepwater mooring system. *Marine Structures,* 51**,** 40-64.

WILLIAMS, A. & LI, W. 2000. Water wave interaction with an array of bottom-mounted surface-piercing porous cylinders. *Ocean Engineering,* 27**,** 841-866.

WILLIAMS, A. & RANGAPPA, T. 1994. Approximate hydrodynamic analysis of multi-column ocean structures. *Ocean Engineering,* 21**,** 519-573.

WU, M. 2014. Numerical analysis of docking operation between service vessels and offshore wind turbines. *Ocean engineering,* 91**,** 379-388.

XIA, J. & TAGHIPOUR, R. Feasibility of TLP with Tender Assisted Drilling for Northwest Australian Waters-A Case Study. Offshore Technology Conference, 2012. Offshore Technology Conference.

XIONG, H., YANG, J. & TIAN, X. 2015. An experimental study on the inline wave force on a truncated vertical cylinder. *Ships and Offshore Structures*, 1-16.

XU, X., YANG, J.-M., LI, X. & XU, L.-Y. 2015. Time-domain simulation for coupled motions of three barges moored side-by-side in floatover operation. *China ocean engineering,* 29, 155-168.

ZHAO, W., TAYLOR, P., WOLGAMOT, H., MOLIN, B. & TAYLOR, R. E. 2020. Group dynamics and wave resonances in a narrow gap: modes and reduced group velocity. *Journal of Fluid Mechanics,* 883.

ZHAO, W., YANG, J., HU, Z. & TAO, L. 2014. Prediction of hydrodynamic performance of an FLNG system in side-by-side offloading operation. *Journal of Fluids and Structures,* 46, 89-110.